2014

Bio-inspired surface engineering for hydrophobicity

Hua Guo
Edith Cowan University

Edith Cowan University

Copyright Warning

USE OF THESIS

The Use of Thesis statement is not included in this version of the thesis.

Bio-inspired Surface Engineering for Hydrophobicity

Hua Guo

Submitted in total fulfillment of the requirements

of the degree of

Doctor of Philosophy

School of Engineering

Edith Cowan University

March 2014

Declaration

I certify that this thesis does not, to the best of my knowledge and belief:

(i) incorporate without acknowledgment any material previously submitted for a degree or diploma in any institution of higher education;

(ii) contain any material previously published or written by another person except where due reference is made in the text; or

(iii) contain any defamatory material.

I consent to grant Edith Cowan University library the permission to make duplicate copies of this thesis in accord with the University rules and regulations.

Acknowledgements

Firstly, and most importantly, I am deeply indebted to Dr Zonghan Xie, my Principal Supervisor from the beginning, for the opportunity to work under his instruction, for leading me to explore the vast and exciting world of scientific research, and for his assistance in many aspects. His dedication to research has inspired me to realize the skills and mindset an authentic scientist should have.

I would like to express my great appreciation to Dr Jeremy Shaw, my Co-Supervisor, for his invaluable support with preparing leaf samples and performing Scanning Electron Microscopy imaging at The University of Western Australia. Both Dr Eddie van Etten, my Co-Supervisor, and Professor Kingsley Dixon have contributed precious biological knowledge to this research. Professor Dixon also kindly provided access to leaf samples through the Kings Park and Botanic Garden Authority. Special thanks are given to Dr Xiaoli Zhao for facilitating access to research equipments and for his expertise with Finite Element Modelling and relevant mechanical tests. Thanks are also given to Dr Zhong-Tao Jiang from Murdoch University for his valued instructions and his assistance on XPS measurements.

Similarly, I extend my thanks to Dr Majid Rad and Associate Professor Laichang Zhang for their contributions as my Principal Supervisor

for the periods of Dec 2012∼present and July∼Dec 2012, respectively. Their suggestions on research methods and strategies were always beneficial and encouraging to me. Dr Rad helped greatly with revising the thesis and undertaking relevant administrative procedures to progress this project. I am also grateful to Professor Daryoush Habibi, the Head of the School of Engineering, for his enthusiastic support on my research. I benefited a lot from Dr Greg Maguire's advice on academic writing and his help on revising the thesis.

I really appreciate Heather Williams, Narelle Jones, Dr Silvia Torezani, Sharon Smart, Dr Natasha Ayers, and more at Graduate Research School for their kindness and concerns. I thank very much Muriel Vaughan, Myra Kendall, Sue Drew, and Kim Gardiner for their administrative assistance at the School of Engineering. Many thanks are given to Zhongyi Cai, Siong Khai Ong and Jing Miao for their friendships and the leisure time we spent together, to Mohammad Shoeb Ahmed for research collaboration, to Simona O'Brien for her handy advice.

I gratefully acknowledge the research scholarship provided by Edith Cowan University. And last but not least, a big thank you is given to my family whose endless support and understanding made my career journey so much easier.

Publications

Guo, H.; Jiang, Z. T.; Shaw, J.; Dixon, K.; Yin, C. Y.; Xie, Z. Elucidating the surface geometric design of hydrophobic Australian *Eucalyptus* leaves: Experimental and modeling studies. [Ready for journal submission]

Guo, H.; Zhao, X.; Jiang, Z. T.; Wood, B. J.; Rahman, M. M.; Xie, Z. Wetting and mechanical properties of fluorinated diamond-like carbon coatings prepared by closed-field unbalanced magnetron sputtering. [Manuscript drafted]

Ahmed, M. S.; Munroe, P.; Jiang, Z. T.; Zhao, X.; Wajrak, M.; Guo, H.; Rickard, W.; Xie, Z. Corrosion- and Damage-Resistant Nitride Coatings for Steel. *Journal of the American Ceramic Society*, **2012**, 95 (9), 2997-3004. [Performed AFM scanning, electro-chemistry and graph editing]

Pittman, C. U. Jr.; Mohan, D.; Eseyin, A.; Li, Q.; Ingram, L; Hassan, E. M.; Mitchell, B.; Guo, H.; Steele, P. H. Characterization of Bio-oils Produced from Fast Pyrolysis of Corn Stalks in an Auger Reactor. *Energy Fuels*, **2012**, 26 (6), 3816-3825. [Performed sample preparation and NMR experiemnts]

Yin, C. Y.; Minakshi, M.; Ralph, D. E.; Jiang, Z. T.; Xie, Z. H.;

Guo, H. Hydrothermal synthesis of cubic -Fe_2O_3 microparticles using glycine: Surface characterization, reaction mechanism and electrochemical activity. *Journal of Alloys and Compounds*, **2011**, 509, 9821–9825. [Performed AFM scanning]

Abstract

Highly evolved, efficient and sophisticated biological systems can be used as models for scientific innovations. This research explored specific surface structures on plant leaves with respect to their hydrophobicity in the context of the often arid Australian climate. The relationships between leaf surface structures and their hydrophobicity could inform the making of artificial surfaces with specially designed hydrophobicity.

Moderate hydrophobicity and strong surface adhesion were discovered on many study plant leaves. Scanning Electron Microscopy (SEM) revealed that their surface morphologies could be categorized into four groups while their water-repellent mechanisms were considered at an individual species level. Specifically, physical models were built based on the topography of several *Eucalyptus* species. Wetting robustness and surface free energy analyses were performed with these models to study wetting transitions on surfaces with specific microscopic features.

In the fabrication component of the study, a convenient self-assembly procedure of oxysilane successfully converted a hydrophilic glass slide into a hydrophobic surface, with the measured contact angle changing from 30.8 to more than 100°. Atomic force microscope (AFM)

images showed randomly distributed roughness at a micrometre scale on these self-assembled hydrophobic surfaces. Samples with square arrays of micro-posts were also fabricated following a sophisticated photo-lithography process. Wetting properties similar to some leaves, namely moderate hydrophobicity and strong surface adhesion, were observed with these fabricated samples. Anisotropic wetting, liquid-surface contact footprints and base lengths on these micro-textured surfaces were also investigated.

Finally, fluorine containing diamond-like carbon (F-DLC) coatings were examined because of their chemical inertness, mechanical durability, and low surface energy. F-DLC films were prepared by closed-field, unbalanced, magnetron sputtering (CFUBMS) on silicon substrate to study their wetting and mechanical properties. The influences of CF_4 and C_2H_2 gas addition during fabrication on these properties were explored by measuring contact angles, fluorine contents, surface roughness, Young's modulus and hardness. Simulation from Finite Element Analysis with COMSOL software was also conducted to confirm the mechanical results obtained in nano-indentation experiments.

The leaf surface geometries revealed in this study could trigger further relevant research and applications. Surface free energy analysis on the built models could lead to a deeper theoretical understanding of wetting state transition for these geometries. The preliminary results on the self-assembly of oxysilane at ambient conditions could

contribute to the development of cost-efficient and environmentally friendly methods for fabricating durable hydrophobic coatings. The results of F-DLC coatings could be beneficial for manipulating surface free energy and mechanical properties, to match specific requirements for certain applications.

Contents

Chapter 1

Introduction

1.1 Background

Wetting, the contact between a solid phase and a liquid phase, is a ubiquitous phenomenon as liquid water exists almost everywhere on earth. Different levels of wetting are found in nature. Generally, tree leaves are fully covered by water film after a shower, while under the same conditions water pools in some bush leaves, without covering the whole leaf surface. Conversely, spherical dew droplets, are usually found on grass leaves and spider webs in early autumn mornings in temperate climates. Striking examples include on lotus leaves and bird feathers. Water forms spherical droplets on the horizontal surfaces in both cases and readily rolls off when these surfaces are slightly tilted.

The wetting condition on many tree leaves can be categorized as hydrophilic, on grass leaves and spider webs as hydrophobic, on lotus leaves and bird feather as superhydrophobic. Different wetting types also support various practical applications. For example, hydrophilicity is preferred for water adhesion and col-

lection, while hydrophobicity is preferred for water-proofing functions including on clothes, window glass, autos and electronics. Superhydrophobicity, characterized with high water contact angles and small roll-off angles, has received most research attention, due to its additional functions, such as self-cleaning [1–5], anti-fogging [6], anti-icing [7, 8], buoyancy [9] and drag reduction [10, 11].

The fundamental theory of wetting dates back to 200 years ago, when Young claimed the existence of a contact angle for a specific combination of solid and liquid [12]. In the mid 20th century, the classical Wenzel [13] and Cassie [14] wetting models were introduced and incorporated surface roughness factors. Nearly 50 years later, the explicit microscopic images of lotus leaf [15], with structural details of microscopic papillae and nano-scale wax, indicated the critical importance of multi-scale surface roughness for superhydrophobicity. Ever since, superhydrophobicity has been extensively researched through experiments, calculations and simulations. Despite major progress has been made on this topic, theoretical descriptions of wetting modes are still debated and difficulty is encountered during the conversion of relevant laboratory prototypes to industrial use.

1.2 Motivation for the research

Wetting has been studied extensively in the past two decades. Various models have been built to simulate wetting conditions on surfaces with different geometry [16–18]. Physics, mechanics, dynamics, kinetics and thermodynamics have been introduced to the theoretical studies on different scale levels [19]. However, questions such as how nano-structures specifically affect a surface's wettability and how wetting conditions transition, are still left unanswered [20].

Hundreds of materials and dozens of fabrication techniques have been combined to generate surfaces with extreme wetting properties [21]. Impacts of wetting properties on other natural occurrences, such as corrosion and friction, have been scrutinized and utilized in laboratories [22, 23]. However, the commercialization of these artificial water-repellent surfaces has faced several challenges.

1. Most of these fabricated surfaces are quite fragile [24] and are easily damaged by mechanic impacts or even gentle rubbing. Specifically, most surfaces with low surface energy are made of organic polymers, which are usually less mechanically robust than inorganic materials, especially metals.

2. These fabricated surfaces still absorb oil and grease contaminants, even though they are rendered superhydrophobic for self-cleaning [25]. Oily substances can easily adhere, impregnate and block the fine structures of water-repellent surfaces, due to their low surface energy. Eventually, the accumulation of dirt particles significantly reduces of superhydrophobic or water-repellent properties.

3. These fabricated surfaces cannot repair themselves from some segmental malfunction [25]. In contrast, plant leaves may be delicate and fragile, but they can regenerate their hydrophobic epicuticular wax layer quickly and recover full surface properties. This self-repairing property compensates for the fragility of wax layers and secures long-time stability.

Although it is difficult to duplicate the surface morphology and biological system of a living plant leaf using today's science and engineering, it is still possible to simulate water repellent behaviour on fabricated surfaces by harnessing chemical reactions and physical transitions. By observing water-repellent surfaces in

nature, several artificial surfaces have been fabricated to mimic plant leaf surfaces successfully [26, 27]. The current study aims to find specific wetting scenarios on native Australian plant leaves and explore the relationships between topography and wetting properties, given the occurrence of arid climates in Australia and plant species. The thesis should contribute to some extent to its unique and diverse knowledge of wetting and help overcome some challenges listed above.

1.3 Scope of thesis

The current study follows a bio-inspired strategy: revealing structures of particular plant leaves, building models by simplifying the structures, performing relevant calculations and analysis, and finally undertaking experimentation with artificial surfaces.

Firstly, the thesis focuses on surface imaging of selected native Australian plant leaves using Scanning Electron Microscope (SEM). Corresponding wetting scenarios for each species, such as high contact angles, strong surface adhesion, and directional collection are identified using contact angle instruments. The selected species are divided into different categories for further discussion. Models are subsequently constructed for calculations that employ critical pressure and free surface energy strategies. The roles of micro-structures and nano-structure play in surface wetting are discussed based on theoretical predictions.

Artificial surfaces characterized with microscopic cylindrical posts are fabricated in order to study the influence of micro-structural geometric parameters on surface wetting. Fluorine-doped diamond-like carbon (F-DLC) coatings are also prepared to study their wetting and mechanical properties. These artifi-

cial surfaces, coupled with bio-surfaces found in nature, provide ideal platforms for further exploration of fabricated surfaces that are mechanically durable and contamination free.

1.4 Summary of chapters

Chapter 2 presents a literature review on superhydrophobic research. It begins with general wetting phenomena, classic wetting principles, and development of wetting theories. Next, the specific wetting phenomenon of superhydrophobicity is characterised and various applications are highlighted. Fabrication methods for artificial superhydrophobic surfaces, with different topographies and roughness, are also summarized.

Chapter 3 summarizes different types of selected native Australian leaves based on their specific topographies and corresponding wetting attributes. Models are introduced and analysed to predict wetting scenarios under different hypothetical conditions. Diatoms are also considered at a theoretical level in relation to the wetting of their external pores.

Chapter 4 describes the special wetting phenomena of several Australia native *Eucalyptus* leaves. Their contact angles and topographical details are obtained and discussed. Models based on the microscopic level are built to perform surface energy analysis and critical pressure calculations. The calculated surface energy and critical pressure are compared between *Eucalyptus* and lotus leaves.

Chapter 5 details the fabrication, wetting and mechanical attributes of micro-textured surfaces with square arrays of microscopic cylindrical posts. The influence of micro-post geometric factors on contact angles and surface adhesion is

discussed.

Chapter 6 and 7 discuss the wetting and mechanical properties of fluorine-doped diamond-like carbon (F-DLC) coatings.

Chapter 8 gives a brief summary and conclusions on this study. Future research on this topic is also outlined.

References

[1] Ralf Blossey. Self-cleaning surfaces — virtual realities. *Nature Materials*, 2 (5):301–306, 2003. 2

[2] Bharat Bhushan, Yong Chae Jung, and Kerstin Koch. Self-cleaning efficiency of artificial superhydrophobic surfaces. *Langmuir*, 25(5):3240–3248, 2009.

[3] Akira Nakajima, Kazuhito Hashimoto, Toshiya Watanabe, Kennichi Takai, Goro Yamauchi, and Akira Fujishima. Transparent superhydrophobic thin films with self-cleaning properties. *Langmuir*, 16(17):7044–7047, 2000.

[4] Liting Zhang, Songtao Wu, Andreas Buthe, Xueyan Zhao, Hongfei Jia, Songping Zhang, and Ping Wang. Poly(ethylene glycol) conjugated enzyme with enhanced hydrophobic compatibility for self-cleaning coatings. *ACS Applied Materials & Interfaces*, 4(11):5981–5987, 2012.

[5] Daniela Caschera, Barbara Cortese, Alessio Mezzi, Marco Brucale, Gabriel Maria Ingo, Giuseppe Gigli, and Giuseppina Padeletti. Ultra hydrophobic/superhydrophilic modified cotton textiles through functionalized diamond-like carbon coatings for self-cleaning applications. *Langmuir*, 29 (8):2775–2783, 2013. 2

[6] Yu Chen, Yabin Zhang, Lei Shi, Jing Li, Yan Xin, Tingting Yang, and Zhiguang Guo. Transparent superhydrophobic/superhydrophilic coatings for self-cleaning and anti-fogging. *Applied Physics Letters*, 101(3):033701, 2012. 2

[7] Jie Xiao and Santanu Chaudhuri. Design of anti-icing coatings using supercooled droplets as nano-to-microscale probes. *Langmuir*, 28(9):4434–4446, 2012. 2

[8] Min Ruan, Wen Li, Baoshan Wang, Binwei Deng, Fumin Ma, and Zhanlong Yu. Preparation and anti-icing behavior of superhydrophobic surfaces on aluminum alloy substrates. *Langmuir*, 29(27):8482–8491, 2013. 2

[9] Hendrik Bargel, Kerstin Koch, Zdenek Cerman, and Christoph Neinhuis. Structure-function relationships of the plant cuticle and cuticular waxes — a smart material? *Functional Plant Biology*, 33:893–910, 2006. 2

[10] Richard Truesdell, Andrea Mammoli, Peter Vorobieff, Frank van Swol, and C. Jeffrey Brinker. Drag reduction on a patterned superhydrophobic surface. *Physical Review Letters*, 97:044504, 2006. 2

[11] Bharat Bhushan. Biomimetics inspired surfaces for drag reduction and oleophobicity/philicity. *Beilstein Journal of Nanotechnology*, 2:66–84, 2011. 2

[12] Thomas Young. An essay on the cohesion of fluids. *Philosophical Transactions of the Royal Society of London*, 95:65–87, 1805. 2

[13] Robert N. Wenzel. Resistance of solid surfaces to wetting by water. *Industrial Engineering Chemistry*, 28(8):988–994, 1936. 2

[14] A. B. D. Cassie and S. Baxter. Wettability of porous surfaces. *Transactions of the Faraday Society*, 40:546–551, 1944. 2

[15] W. Barthlott and C. Neinhuis. Purity of the sacred lotus, or escape from contamination in biological surfaces. *Planta*, 202:1–8, 1997. 2

[16] Neelesh A. Patankar. On the modeling of hydrophobic contact angles on rough surfaces. *Langmuir*, 19(4):1249–1253, 2003. 2

[17] Abraham Marmur. Wetting on hydrophobic rough surfaces: To be heterogeneous or not to be? *Langmuir*, 19(20):8343–8348, 2003.

[18] Masashi Miwa, Akira Nakajima, Akira Fujishima, Kazuhito Hashimoto, and Toshiya Watanabe. Effects of the surface roughness on sliding angles of water droplets on superhydrophobic surfaces. *Langmuir*, 16(13):5754–5760, 2000. 2

[19] Bharat Bhushan and Yong Chae Jung. Natural and biomimetic artificial surfaces for superhydrophobicity, self-cleaning, low adhesion, and drag reduction. *Progress in Materials Science*, 56(1):1–108, 2011. 2

[20] Michael Nosonovsky and Bharat Bhushan. Do hierarchical mechanisms of superhydrophobicity lead to self-organized criticality? *Scripta Materialia*, 59:941–944, 2008. 2

[21] Seong H. Kim. Fabrication of superhydrophobic surfaces. *Journal of Adhesion Science and Technology*, 22:235–250, 2008. 3

[22] MG Wirthensohn and M Sedgley. Epicuticular wax structure and regenera-

tion on developing juvenile *Eucalyptus* leaves. *Australian Journal of Botany*, 44(6):691–704, 1996. 3

[23] Iris Bitterlich and Mahesh K. Upadhyaya. Leaf surface ultrastructure and susceptibility to ammonium nitrate injury. *Canadian Journal of Botany*, 68 (9):1911–1915, 1990. 3

[24] J. M. Benyus. *Biomimicry: Innovation Inspired by Nature*. William Morrow & Company Inc, New York, NY, USA, 1997. 3

[25] Christian Dorrer and Jurgen Ruhe. Some thoughts on superhydrophobic wetting. *Soft Matter*, 5:51–61, 2009. 3

[26] Peter Forbes. Self-cleaning materials: Lotus leaf-inspired nanotechnology. *Scientific American*, 299 (2):88–95, 2008. 4

[27] Bharat Bhushan, Yong Chae Jung, Adrian Niemietz, and Kerstin Koch. Lotus-like biomimetic hierarchical structures developed by the self-assembly of tubular plant waxes. *Langmuir*, 25(3):1659–1666, 2009. 4

Chapter 2

Literature Review

The natural phenomenon of wetting occurs wherever liquid water makes contact with a solid surface. Practical procedures are carried out to either facilitate or prohibit wetting by water in many aspects of the society, from ancient history to present time. Fundamental principle of wetting can be traced back to the early 19th century [1]. Nearly in the mid 20th century, two classical models were introduced to quantitate wetting through surface roughness parameters [2, 3]. It was not until the 1990's that the concept of multi-scale surface roughness was brought into highlight [4]. Ever since, literature in this field has been greatly nourished by experimentations and calculations based on this critical concept. Fundamental questions and engineering issues, however, still remain unsolved and open for further investigation.

2.1 Surface tension

Wetting is caused and determined by the liquid-solid molecular interaction on the interface. The green region in Fig. 2.1 depicts the outmost layer of a liquid phase (such as water) that is contacting another phase above (such as air). Water molecules below the interface readily form an optimal number of hydrogen bonds with neighbouring molecules to achieve a physical equilibrium with a net force of zero. However, molecules on the interface are under a different physical environment, due to lack of neighbouring molecules of the same type beyond the interface. These asymmetric attractive forces result in surface molecules being pulling into the liquid bulk and therefore there tend to be fewer molecules on the interface.

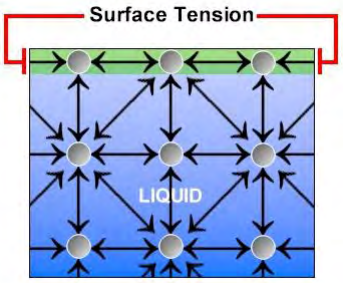

Figure 2.1: Water molecules (marked with green) on the liquid-air interface [5].

A force is thus created with a direction parallel to the interface. Surface tension is defined as this force along a line of unit length, with an SI (International System of Units) unit of N/m. Water is among the liquids with highest surface tensions, with a value of 72.8 mN/m at 20 °C [6]. Surface tension minimizes the surface area and causes the membrane-like water "skin" to float tiny subjects, such as a needle or a paper clip, on the interface. Hydrocarbon solvents or oils

usually have smaller surface tensions, which render their wetting a surface much easier than water.

2.2 Solid surfaces

For water molecules in contact with a solid surface, there exist two opposing forces: adhesive force that causes water to spread out on the solid surface and cohesive force that minimizes the contact with the solid surface. Water's behaviour greatly depends on whether water molecules are more strongly attracted to each other than they are to the solid phase. A general case with the presence of the third phase (gas) is analysed in the same way such that all forces balance on the interfaces. Based on the extent to which water makes contact, surfaces can be characterized in a range from non-wetting to wetting. In Fig. 2.2a, water makes the least contact as possible with the surface and forms spherical droplets. In Fig. 2.2c, water spreads as much as possible on the surface and makes major contact. These two conditions are termed as hydrophobic (water-hating) and hydrophilic (water-loving), respectively.

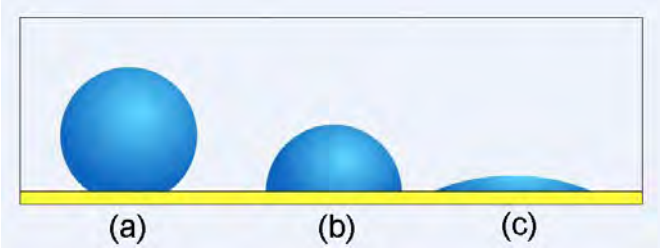

Figure 2.2: Different wetting conditions: (a) minor wetting (hydrophobic), (b) medium wetting, and (c) major wetting (hydrophilic) [7].

The interaction between water molecules and a solid surface plays a critical

role in determining the surface's wettability. Conventionally, solids that water interacts with can be divided into high-energy and low-energy solids. The chemical bonds that hold high-energy solids together are very strong such as metallic, covalent and ionic, because it takes a large amount of energy to break them. This group includes metals, crystals, glasses and ceramics. Since the attractive forces between water and high-energy solids are much stronger than the hydrogen bonds formed between inner and outer water molecules, a large contact area is favoured and major wetting is achieved.

Conversely, the chemical bonds that hold low-energy solids together are usually very weak such as van der waals force and hydrogen bonds, and it requires very minor energy to break them. This group mainly includes hydrocarbons and other organic molecules. Water can achieve minor wetting or non-wetting with low-energy solid surfaces.

In nature, the epidermal layers of many plant leaves are made of long-chain hydrocarbons [8]. Therefore, water can rarely achieve major wetting on most plant leaves, rendering them hydrophobic. Lotus (*Nelumbo nucifera*) has long become the symbol of purity in eastern Asian religions. They remain clean even though when growing in muddy water. Water droplets usually remain spherical on horizontal lotus leaves (Fig. 2.3a). A slight tilt of the horizontal leaves will cause droplets to roll off (Fig. 2.3b), taking away dust and dirt [9].

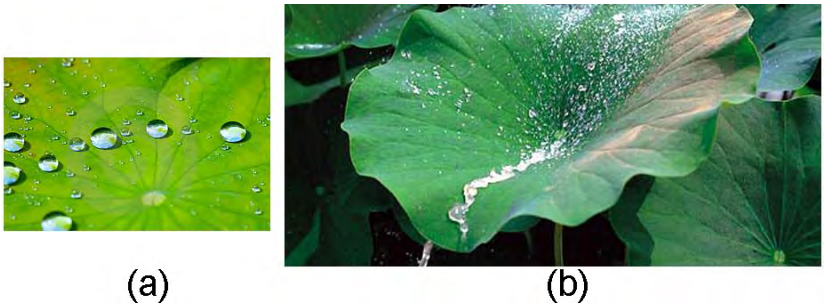

Figure 2.3: Superhydrophobicity on lotus leaves: (a) Water droplets sit on a horizontal lotus leaf [10], and (b) Water droplets roll off a tilted lotus leaf [11].

2.3 Theoretical background

2.3.1 Contact angle

Wetting is the intermolecular interaction between a liquid and a solid when they are brought together and then an interface develops between. The theoretical description on wetting dates back about 200 years ago. The British genius and polymath, Thomas Young, presented an epochal essay to the Royal Society in 1804 and published it in 1805. In this article, "An essay on the cohesion of fluids" [1], Young states, "for each combination of a solid and a fluid, there is an appropriate angle of contact between the surface of the fluid exposed to the air, and to the solid."

Today, contact angle (θ) is termed to describe the water wettability of surfaces (Fig. 2.4). A high contact angle ($90° < \theta \leq 180°$) means that wetting is not favoured and water tends to maintain the least contact possible with the surface as shown in Fig. 2.2a. A low contact angle ($0 \leq \theta < 90°$) usually denotes that wetting is favoured and water tends to disperse and maintain the largest contact possible (Fig. 2.2c).

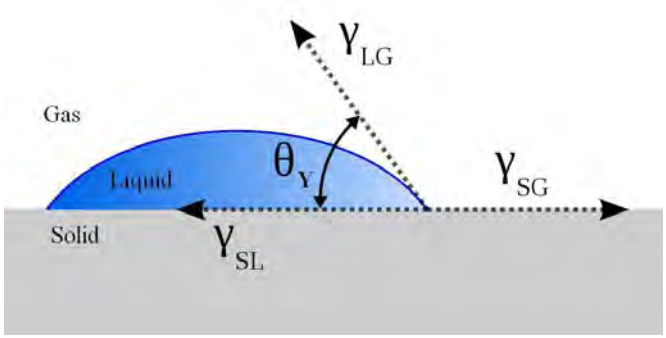

Figure 2.4: Schematic illumination of a liquid droplet sitting on a solid surface and the forces applied on the triple line [12].

Based on Young's description [1], the physical condition of a droplet is determined by surface tensions acted on the contact line (also referred as triple line), where the three phases converge. The net force per unit length acting along the triple line between three phases is equal to zero. Young's equation is presented as follows [13]:

$$\gamma_{SG} = \gamma_{SL} + \gamma_{LG} \cos \theta_Y \tag{2.1}$$

where

θ_Y = Young's contact angle,

γ_{SG} = Interfacial tension between the solid and gas,

γ_{SL} = Interfacial tension between the solid and liquid,

γ_{LG} = Interfacial tension between the liquid and gas.

Large θ_Y values correlate to high hydrophobicity. When $\gamma_{SG} > \gamma_{SL} + \gamma_{LG}$, it means complete wetting. On the contrary, when $\gamma_{SL} > \gamma_{SG} + \gamma_{LG}$, it means zero wetting. In order to predict wetting, a spreading parameter S is introduced: $S = \gamma_{SG} - (\gamma_{SL} + \gamma_{LG}) = \gamma_{LG}(\cos \theta_Y - 1)$.

2.3.2 The Wenzel model and Cassie-Baxter model

Young's equation applies to ideally smooth and flat surfaces. However, when it comes to reality, such ideal surfaces never exist. Factors other than interfacial tensions, such as roughness and impurity, also affect the wetting properties to an unexpected extent. Two models have been built based on the hypothetical wetting regimes (see Fig. 2.5).

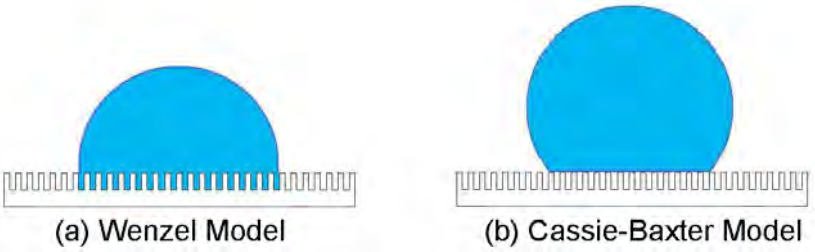

Figure 2.5: Sketches of the Wenzel model and Cassie-Baxter model [14].

In the Wenzel state, the liquid fills all the voids below the liquid and thus develops a large contact area. Wenzel introduced a roughness ratio, r, for a homogeneous wetting regime, and the Wenzel's equation is described as follows [2]:

$$\cos\theta_W = r\cos\theta_Y \tag{2.2}$$

where θ_W is the observed contact angle and θ_Y is the Young's contact angle as defined for ideal solid surfaces of the same material. The roughness ratio, r, is defined as the ratio of the actual area of the solid surface to its projected area (or the effective area to the geometric area). For a rough surface, r is usually greater than 1. This formula makes an adjustment for the increase in interfacial area caused by the presence of a texture or roughness when the liquid contacts a

surface.

It can be easily deduced that the cosine value of the apparent contact angle increases as the roughness r increases, and the Young's contact angle is fixed for a specific wetting set of liquid and solid surface. For a hydrophilic surface ($0° < \theta_Y < 90°$, $0 < \cos\theta_Y < 1$), an increase in roughness leads to an increase of the value of $\cos\theta_W$ and a decrease of θ_W. On the contrary, for a hydrophobic surface ($90° < \theta_Y < 180°$, $-1 < \cos\theta_Y < 0$), an increase in roughness causes a decrease of the value of $\cos\theta_W$ and an increase of θ_W. That is, an increase in roughness will enhance either hydrophilic or hydrophobic properties of a surface accordingly [15]. However, even though there is a possibility that a roughness with certain values ($r > 1/|\cos\theta_Y|$) will bring any surface to complete wetting ($\theta_W = 0°$) or complete dryness ($\theta_W = 180°$), this possibility contradicts outcomes of practical experiments.

In the Cassie state, the droplet, as illustrated in Fig. 2.5, rests upon the asperities with gas filling all the voids below. The interfacial area is therefore less than it would be for a droplet of the same volume and apparent contact angle in the Wenzel state. To compensate the reduction in actual interfacial area, f, a fraction of solid surface area wetted by the liquid is introduced. The Cassie-Baxter equation (Cassie's law) is presented as below [16]:

$$\cos\theta_{CB} = r_f f \cos\theta_Y + f - 1 \tag{2.3}$$

where θ_{CB} is the Cassie-Baxter contact angle, r_f is the roughness ratio of the surface area wetted by the liquid and f is the fraction of solid surface area contacting the liquid on the horizontal plane. When $f = 1$ and $r_f = r$, the Cassie-Baxter

equation is simplified to the Wenzel equation. When the interface contains various fractions of surface roughness, each fraction factor of the total contact area is denoted by f_i. The sum of all f_i is equal to unity or 1. The Cassie-Baxter equation can also be generalized for multiple fractions of surface roughness as [17]

$$\gamma_{LV} \cos\theta_{CB} = \sum_{n=1}^{N} f_i(\gamma_{i,SV} - \gamma_{i,SL}) \tag{2.4}$$

Here γ_{LV} is the interfacial tension between the liquid and vapour, $\gamma_{i,SV}$ represents the solid-vapour surface tension on each component and $\gamma_{i,SL}$ means the solid-liquid interfacial tension of each component. For a two component system, the Cassie-Baxter equation is specified as below [17]:

$$\gamma_{LV} \cos\theta_{CB} = f_1(\gamma_{1,SV} - \gamma_{1,SL}) + (1 - f_1)\gamma_{LV} \tag{2.5}$$

2.3.3 The wetting state transition

The wetting scenario transition between two classical models — Cassie-Baxter and Wenzel — is worth studying due to its myriad practical applications in engineering. Based on some practical experiments [18], the transition from Cassie-Baxter to Wenzel can be a one-way process and the opposite phenomenon has never been witnessed.

The transition is assumed to take place when the contact angle can fulfil both the Wenzel equation and the Cassie-Baxter equation. By combining these two equations, the contact angle during the transition is solved: $\cos\theta_Y = (f - 1)/(r - r_f f)$, where $f = 1 - f_{LA}$. Nosonovsky and Bhushan [18] studied how contact angle changes with roughness of superhydrophobic surfaces by plotting

these two equations. In the Wenzel wetting regime (Fig. 2.6i), the value of $\cos\theta$ decreases with the increasing roughness at a slope less than -1 (because roughness $r > 1$). In the Cassie-Baxter wetting regime (Fig. 2.6-ii), the value of $\cos\theta$ also decreases with the increasing roughness, but at a slope between -1 and 0 (because roughness $R_f \sim 1$ and $0 \leqslant (1 - f_{LA}) < 1$).

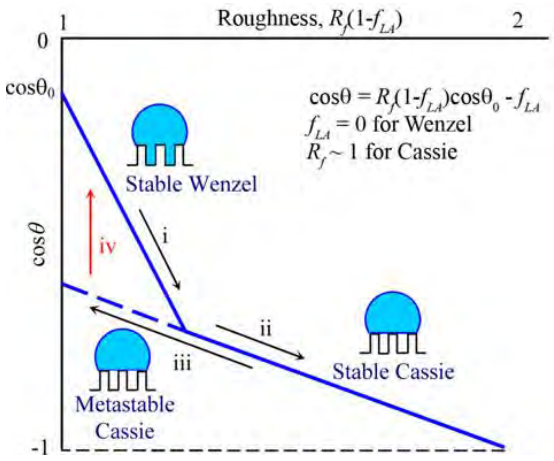

Figure 2.6: The cosine value of contact angle plotted as a function of roughness for superhydrophobic surfaces [18].

Increased roughness may facilitate the wetting transition from the Wenzel scenario to the Cassie-Baxter scenario. However, the opposite transition (from metastable Cassie state to the Wenzel state, Fig. 2.6-iv) has never been confirmed experimentally. Nosonovsky and Bhushan [18] explained the unlikeliness by the high energy barriers during the transition that are caused by destabilization. Fig. 2.6 also indicates the apparent contact angle tends to follow the Wenzel wetting regime on hydrophobic surfaces with mild roughness and obey the Cassie-Baxter wetting regime on highly rough hydrophobic surfaces.

The wetting state transition between Cassie-Baxter and Wenzel has been widely studied under specific conditions. Two types of wetting transition have

been discussed: 2D character of wetting transition with liquid filling all pores underneath the droplet, and 1D character of wetting transition with liquid filling only pores in the vicinity of the triple line [19]. Wetting transition was also observed in experiments when the critical value of force acted on the unit length of the triple line is reached.

It has been deduced that both the Wenzel and Cassie-Baxter states can coexist on hydrophobic surfaces ($\theta_Y \sim 100°$) with moderate roughness ($r_s \sim 2$) [16, 20, 21]. The method by which a droplet is created also determines the wetting regime. For example, dispensing a water droplet on a moderately rough surface can result in the Cassie-Baxter state with air pockets locked in the surface asperities. However, when the water droplet is produced by steam condensation, the Wenzel wetting regime is more likely to develop for the droplet [22]. It is reasoned that gaseous water molecules can penetrate the micro-roughness of the surface and fill up the cavity with gradual condensation.

The wetting state transition can also be triggered by external factors. When pressure is applied to a water droplet on the Cassie-Baxter state, a transition to the Wenzel state can also happen [22, 23]. Even though the transition has been studied from different approaches and methods, there is still controversy about which particular mechanism rules the process.

2.3.4 Contact angle hysteresis

The contact angles mentioned above, θ_Y, θ_W and θ_{CB}, deal with macroscale environments and they are normally called "apparent contact angles". The actual contact angles, at which the liquid-air interface meets the solid surface at the

micro- and nano-scale roughness, can be very different according to Nosonovsky and Bhushan [24]. Furthermore, recent theoretical studies put the Wenzel equation and the Cassie-Baxter equation into a thermodynamic framework. When a liquid wets an ideal surface, classic theory predicts only one single contact angle at a thermodynamically stable state. However, a wide range of different metastable states for a wetting system exists in the real world caused by a series of free energy barriers. Thus, the contact angle of one single wetting system presents as a range of values.

Consider the case of a sessile drop that is never thermodynamically stable in an open system, if additional liquid is added (Fig. 2.7a), the contact line advances. The drop displays an advancing contact angle (θ_{adv}) each time the motion ceases. Accordingly, if some volume is taken away from the drop, the contact angle exhibits a receding value (θ_{rec}) before the contact line retreats. Alternatively, when a droplet is moving on a tilted solid surface (Fig. 2.7b), the advancing contact angle (θ_{adv}) is defined as the contact angle measured at the front of the moving droplet and the receding contact angle (θ_{rec}) refers to the back of the droplet. The advancing contact angle (θ_{adv}) is usually greater than the receding contact angle (θ_{rec}), because of the surface roughness.

This difference between θ_{adv} and θ_{rec} is referred to the contact angle hysteresis ($\Delta\theta_H$),

$$\Delta\theta_H = \theta_{adv} - \theta_{rec} \tag{2.6}$$

And the value of a contact angle falls between the advancing contact angle (θ_{adv}) and the receding angle (θ_{rec}) at different metastable states.

Andrade [26] discussed at least six known sources of contact angle hystere-

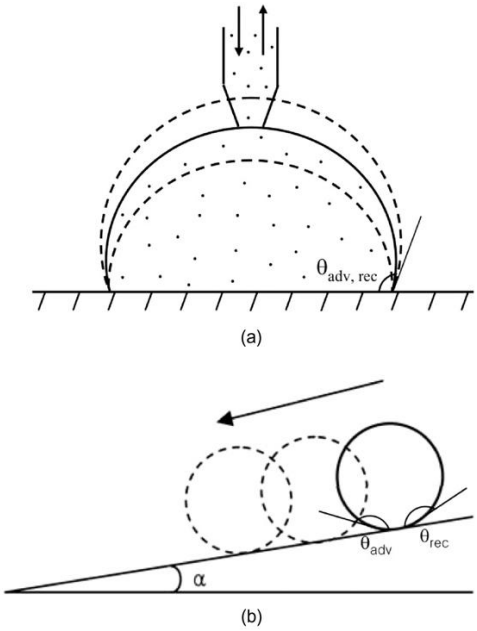

Figure 2.7: Two conditions that advancing and receding angles can be measured [25]: (a) a liquid droplet in contact with rough surface when the volume is added or removed, (b) a liquid droplet moving on a tilted surface with a tilt angle α.

sis categorized into two groups: thermodynamic and kinetic hysteresis. Surface roughness and surface heterogeneity are two sources for thermodynamic hysteresis and are the most common practical sources. The Wenzel equation and the Cassie-Baxter equation actually describe these two factors individually. A conclusion can be drawn from a heterogeneous surface: the advancing angle and the receding angle reflect the characteristics of the low-energy portion and the high-energy portion of the surface, respectively. Similarly, Bhushan and Jung [25] considered that contact angle hysteresis is relevant to energy dissipation on the droplet's flow path. Kinetic hysteresis is related to time or cycle dependent changes in the contact angle.

Small contact angle hysteresis leads to very small water roll-off angles. This

is clearly associated with surfaces bearing self-cleaning abilities such as the lotus leaves. To correctly characterize a surface, it is very important to measure or calculate contact angle hysteresis.

Nosonovsky and Bhushan [27] proposed that contact angle hysteresis equals the sum of the so-called adhesion hysteresis and a term related to the effect of surface roughness, H_r. They applied eq 2.3 to the advancing and receding angles and derived the following equation:

$$\cos\theta_{adv} - \cos\theta_{rec} = R_f(1 - f_{LA})(\cos\theta_{adv0} - \cos\theta_{rec0}) + H_r \tag{2.7}$$

θ_{adv0} and θ_{rec0} refer to the advancing and receding angles for a smooth surface. The first part on the right side of the equation correlates to the contact angle hysteresis for a smooth surface. H_r is equal to the perimeter of the asperity per unit area. In an extreme example of very small solid-liquid fraction of the interfacial area, when the contact angle is large and contact angle hysteresis is small, the above equation can be modified to [27]:

$$\theta_{adv} - \theta_{rec} = (1 - f_{LA})R_f\frac{\cos\theta_{a0} - \cos\theta_{r0}}{-\sin\theta_Y} = (\sqrt{1 - f_{LA}})R_f\frac{\cos\theta_{r0} - \cos\theta_{a0}}{\sqrt{2(R_f\cos\theta_0 + 1)}} \tag{2.8}$$

f_{LA} is equal to zero for a homogeneous interface (the Wenzel wetting regime). For a composite interface, it is non-zero and a small value of f_{LA} will lead to a small contact angle hysteresis, which is favoured for self-cleaning properties.

2.4 Mechanisms of superhydrophobic wetting

A surface is entitled as superhydrophobic (exchangeable with ultrahydrophobic, self-cleaning, super water repellent) when it is characterized by a high water contact angle ($> 150°$) and a small contact angle hysteresis. Recent investigations on natural superhydrophobic plant leaves, such as the lotus leaf, have shown that these leaves have hierarchical surface structures (Fig. 2.8). These epidemic waxy surfaces consist of micro-bumps of epidermal cells and nano-bumps of epicuticular wax.

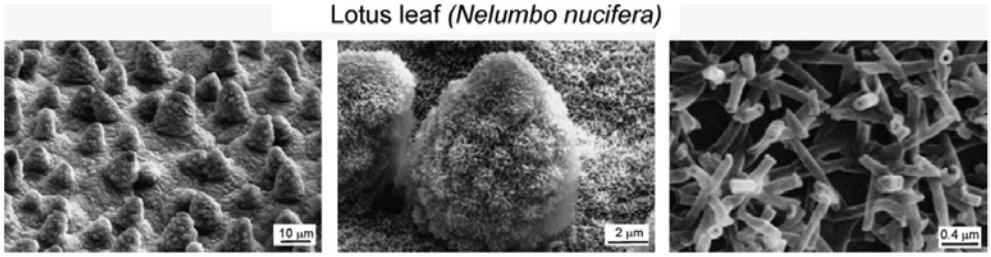

Figure 2.8: SEM micrographs show that Lotus leaf surface is composed of micro-scale papillose epidermal cells and nano-scale epicuticular wax tubules [28].

It becomes a consensus that hierarchical structure is of critical importance for superhydrophobicity. However, mechanisms for hierarchical structures remain unexplained thoroughly, resulting from the complexity of diverse surface topographies and possible wetting scenarios.

Nosonovsky and Bhushan [29] suggested the deciphering of wetting as a multi-scale process. A set of gradual scale lengths presented on a hierarchical surface, based on their suggestion, are associated with different physical mechanisms which act simultaneously and cooperatively at corresponding characteristic scales. They prompted experiments to be carried out to test the involvement of

self-organized criticality, which is relevant to a critical point when the difference between two phases disappears.

Fürstner et al. [30] stated that fabricated surfaces with one scale of roughness can work very well for large "artificial rain" droplets, but they cannot work for small "artificial fog" droplets. Thus, the hierarchical length system should possess the ability to repel droplets at a range of sizes. Gao and McCarthy [31] has showed that two reasons — kinetics of droplet movement and thermodynamics of wetting — make two length scales important for superhydrophobicity. The dual length scales lower the transition energy barriers between metastable states and change the kinetics of contact line recession. They emphasized that the activation energy for the process of receding is greater than that for the process of advancing for a droplet on a solid surface. At the same time, very different physics, such as Laplace pressure and drag reduction slip, is involved about the thermodynamics.

2.5 Superhydrophobicity in nature

Superhydrophobic examples can be widely found in nature. After investigated hundreds of plant species, Neinhuis and Barthlott [32] concluded that plants with superhydrophobic leaves can be found in any habitat and herbs in disturbed area and wetlands dominate this category. Common plants in this category include lotus, Indian cress, lady's mantle, tulipa, iris, drosera and eucalyptus etc [32, 33].

Generally, most birds have superhydrophobic feather to keep them dry and warm. Insects such as butterflies and cicadae grow superhydrophobic wings for the similar reasons [34, 35]. Micro-scale setae on non-wetting legs of a water strider enable them to walk on water surface [36]. In the Namibia Desert, *Steno-*

cara and *Lepidochora* beetles harvest water from mist and fog to provide living water by different means [37].

2.5.1 Structure of cuticle

The thin extracellular membrane on plant leaves is called cuticle. Cuticle protects plant leaves from environmental influence. Both major constituents of the cuticle — the insoluble long-chain polymer called cutin and soluble floral grease called wax — are hydrophobic [38]. Fig. 2.9 shows a generalized cuticle structure with an outer layer "cuticle proper" (usually < 200 nm) and a thick inner "cuticle layer" (up to 17 μm). The thin cuticle proper acts as the primary protective layer and the cuticle layer has a net-like appearance resulting from the growth of the epidermal cells.

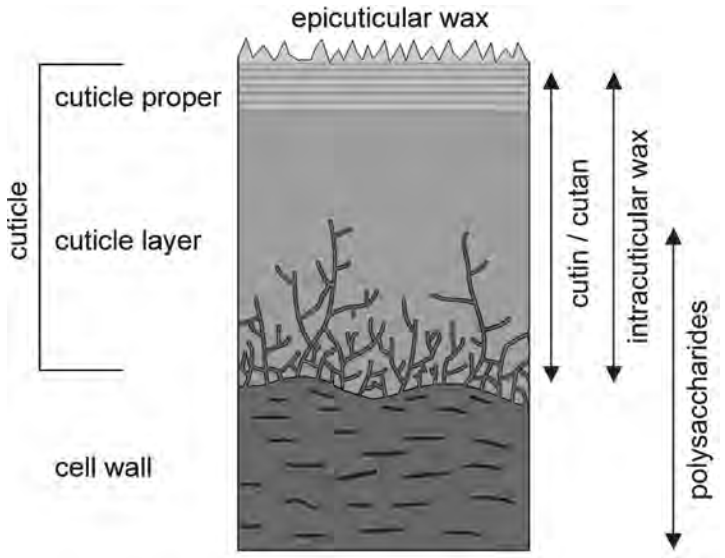

Figure 2.9: Hypothetical sketch of plant leaf cuticle and its constituents [39].

Thin as a few hundred nanometres, cuticle presents at least but not last

the following functions: (1) repel water to keep away pathogenic [40, 41], (2) wash away dust to avoid contamination [41], (3) reduce water erosion and other mechanic erosion [42], (4) regulate radiation budget and adjust temperature indirectly [43, 44], and (5) protect from grazing insects [45–47].

2.5.2 Lotus effect vs. petal effect

Since early 1970s, soon after the scanning electron microscope (SEM) became commercially available, scientists [4, 32, 48] began to investigate tens of thousands of plant surfaces in taxonomic and functional aspects using this new imaging technique. Among them, German biologist Barthlott and Neinhuis concentrated on the water-repellent, anti-adhesive and self-cleaning properties of leaf surfaces [4, 32]. They displayed that leaf surfaces of water-repellent plants are characterized by rough papillose epidermal cells (Fig. 2.8). They concluded that epicuticular wax and its roughness play a vital role in controlling relevant functions.

Later on, a surprising discovery was found about the way water reacts to dust when moving on different surfaces (Fig. 2.10). On normal surfaces, a water droplet slides across and leaves dirt particles sticking to the surface. On lotus-like superhydrophobic surfaces, a water droplet rolls across, picks up dirt and takes it away on the flow.

The term “lotus effect” was thus coined by Barthlott and Neinhuis for characterizing high contact angles and small roll-off angles and excellent anti-adhesive abilities. An important reason for plant leaves to have self-cleaning function is that it keeps water away. Pathogenic germs and organisms readily germinate

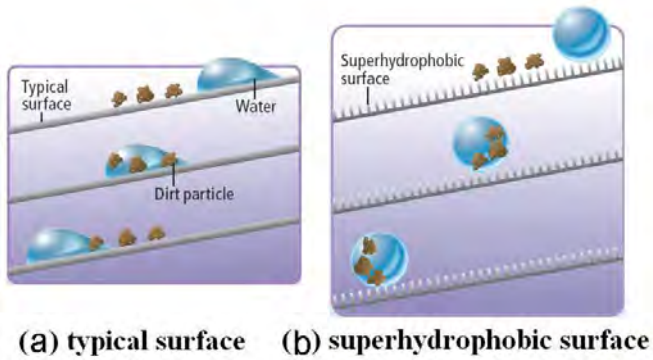

Figure 2.10: A water droplet is moving on: (a) a typical surface, (b) a superhydrophobic surface (Picture is cropped from the original [9]).

and multiple on plant leaves with the presence of water. By removing dust from leaves, plants can also prevent contamination and damage.

Lotus effect is characterized by high static contact angles, low roll-off angles and self-cleaning properties. Water droplets also keep a spherical shape and high contact angles on some rose petals. In contrast, water droplets won't detach even when the rose petal is reversed (see Fig. 2.11). The very high roll-off angles indicate a high adhesive force between the petal and water. Feng and co-workers [49] defined this phenomenon as the "petal effect" as compared to the famous "lotus effect". They found that the rose petal surface is composed of periodic array of micropapillae with an average diameter of 16 μm and height of 7 μm. On each micropapillae there are cuticular folds with a width of around 730 nm. These rose petals exhibit superhydrophobicity with a contact angle of 152.4°.

Both micro- and nano-structures of rose petals are larger than these of lotus leaves as shown as Fig. 2.12. Macroscopically, rose petal surface follows the Wenzel wetting regime on the micro-structure level and the Cassie-Baxter regime on the nano-structure level (or described by Feng et al. [49] as "Cassie impregnating

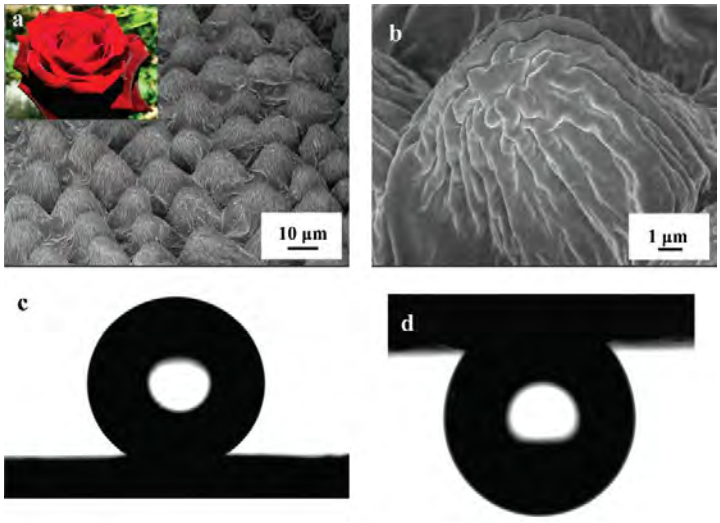

Figure 2.11: Wetting on rose petals: (a,b) SEM images of a rose petal surface in different scales, (c,d) a water droplet stays on a red rose petal [49].

wetting state"). Lotus petal surface follows the Cassie-Baxter regime both on the micro- and nano-structures. Thus water enters the grooves of rose petals but not the nano-scale cuticular folds. The large contact area of water with rose petals leads to great adhesive forces which enable water to cling to the petals even when they are turned upside down.

Interestingly, Bhushan and Her [50] found two kinds of rose petals presenting lotus effect and petal effect respectively. By using AFM, they found that the rose petal with low adhesion (lotus effect)has a higher bump density and a lower peak-to-base height of microstructures compared with that with high adhesion (petal effect).

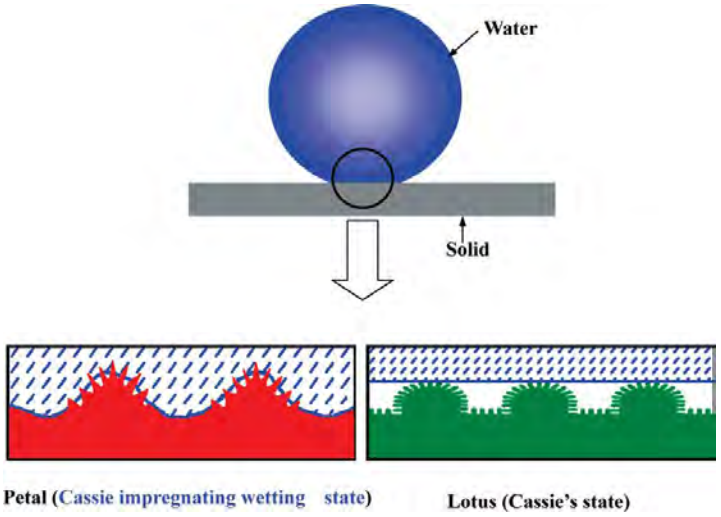

Figure 2.12: Sketch of water-liquid interfacical contact on petal and lotus leaf [49].

2.5.3 *Eucalyptus* in Australia

Eucalyptus is a dominant species in Australia. The question why Eucalyptus has adapted so well to Australia's various stern climates has usually triggered more and more research about this group. Hallam and Chambers [51] undertook an investigation of 315 species of the genus Eucalyptus about the patterns of leaf wax structure to assist the taxonomical categorization. They revealed that for Eucalyptus leaves there are mainly three wax types: plates, tubes, and a mixture of both. Major chemical components of many Eucalyptus epicuticular waxes include long-chain alkyl β-diketones and alkyl primary alcohols [52]. Generally, tubular wax is consisted of alkyl β-diketones and plate wax is made of alkyl primary alcohols [51, 52].

Edwards's work [46] demonstrated that the wax layer on some kinds of Eucalyptus keeps the juvenile leaves away from tortoise beetles' feeding. With the presence of the wax layer, an adult beetle cannot land on the juvenile leaves

easily, since the beetle's claws penetrate the cuticlar structure and no contact area is formed between the adhesive setae and the leaf. Brennan and Weinbaum [53, 54] obtained the similar results after studied the adherence of psyllids to both glaucous young and glossy mature leaves of Eucalyptus globulus.

2.6 Applications of superhydrophobic surfaces

Principles of superhydrophobicity and superhydrophilicity can be applied wherever an interface develops between a liquid and a solid. To decrease the liquid-solid interface area, superhydrophobicity is favoured to aim high contact angle and the Cassie composite non-wetting regime. To increase liquid-solid interface area, superhydrophilicity is favoured to aim low contact angle and the Wenzel wetting regime.

- **Self-cleaning, non-wetting, non-icing and non-sticking** Plants with self-cleaning properties, such as Lotus and India Cress, have been studied extensively in order to fully understand their mechanisms and apply similar principles into daily lives. In 1999, a Lotus-Effect® facade paint was launched to focus on removing dust by droplets rolling off the building external surface without wetting it. Containers coated with a special nano-particle powder (Aeroxide LE®) for multi-purpose applications can be evacuated without any residues.

- **Anti-corrosion and anti-fouling** Liu and co-workers [55] treated copper substrates with *n*-tetradecanoic acid to form a stable flower-like superhydrophobic film, which induced a high contact angle of 158° and improved

the corrosion resistance of copper significantly. Scardino et al. [56] found that coating roughness, air incursion efficiency and air retaining capacity contribute to the anti-fouling function.

- **Reduction of drag** Truesdell et al. [57] tested shear flow on a grooved texture with a superhydrophobic coating. The reduction of effective fluid-surface contact area promoted less drag force and favourable slip condition changes.

  McHale et al. [58] illustrated the drag reducing effects of flow on superhydrophobic interfaces (Fig. 2.13). When a Newtonian liquid flows along a circular channel enclosed by a solid wall, there is a parabolic distribution of the velocity on the cross-section with a maximum value in the centre (Fig. 2.13a). When the upper half of the solid interface is replaced by air, the velocity reaches the maximum on the liquid-air interface due to the continuity of the shear stress from the centre to the interface (Fig. 2.13b). In the case of a superhydrophobic solid tube, a thin film of air can be expected to exist between the liquid flow and solid wall. The velocity of liquid flow should follow a balanced distribution due to the significantly reduced drag friction (Fig. 2.13c).

- **Microfluidic devices** On the micro- and nano-meter level, liquid exhibits surprisingly particular wetting properties and flow behaviours, due to a large surface-to-volume ratio. A capillary length, k_c, is defined as follows when considering a liquid drop placed in gas [33]:

$$k_c = \sqrt{\frac{\gamma_{LG}}{\rho g}} \tag{2.9}$$

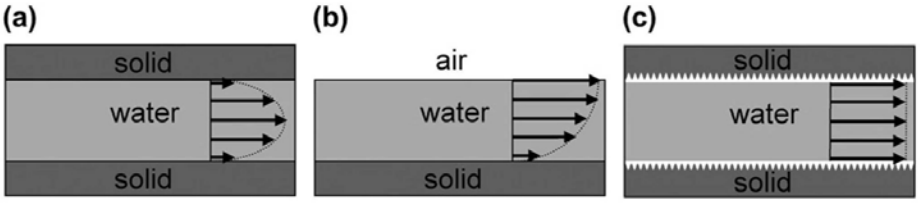

Figure 2.13: Schematic illustration of velocity distribution on the cross-section of a laminar flow in [58]: (a) a normal solid tube with high drag friction on the interface, (b) a normal tube with upper half replaced by air, and (c) a superhydrophobic tube with liquid-air interface built up to reduce drag friction.

Where γ_{LG} is the surface tension at the liquid-gas interface, ρ is the liquid density and g is the gravitational acceleration constant. For a liquid droplet with a size less than capillary length, its gravity is relatively insignificant and can be ignored when predicting the liquid droplet shape at the equilibrium state. Water's capillary length at ambient temperatures is $\sim$ 2.7 mm.

Vorobyev and Guo [59] produced parallel microgrooves with depths of round 30 μm on glass surface using amplified Ti:sapphire laser system. A superwicking phenomenon was observed when distilled water droplets of 16 μL were dispersed on the laser-patterned surface: water wetted the surface along the orientation of microgrooves even when the glass surface was set up vertically (in which water flowed upwards on glass).

By coating the channel walls with responsive polymers, Ionov et al. [60] developed smart microfluidic channels that can switch the wettability of channel walls between hydrophobic and hydrophilic. They used this device to separate a mixture of water and toluene.

- **Water collection**

The Namibia desert Stenocara beetle is a perfect example in nature of water collection. Cohen et al. [61] designed a combination of superhydrophilic patterns on superhydrophobic surfaces to mimic the beetles back. Spider silk web is another distinct example that harvests water in the morning fog and transport it directionally [62]. Water collection efficiency could be manipulated by adjusting the superhydrophobic/hydrophilic pattern on the surfaces and their ratio on the pattern areas.

2.7 Biomimetic surface development

As presented above, it is distinct that micro- and nano-structures on plant surfaces, including cellular protrusions, cuticular foldings and wax platelets, reduce the contact area dramatically between water and the plant leaf surface by the combination of hydrophobic chemistry and multi-scale roughness. Finally, the formation of an enlarged water/air interface leads to a composite wetting regime with air pockets trapped among the epicuticular wax asperities.

Based on the principles learned from nature, various techniques have been exploited for superhydrophobic surface fabrication and coatings by combining hydrophobic chemistry and geometric effects. Research in this field has been growing since the middle 1990s, when more and more applications of nano-structure surfaces have been revealed. In general, techniques employed for delicate construction, such as lithography, etching, dipping and self-assembly, can been transformed to fabricate superhydrophobic surfaces. Bhushan and Jung [25] have summarized these fabrication techniques and listed them in Fig. 2.14. The advantages and disadvantages of these fabrication techniques are listed by Bhushan

and Jung [25] shown in Table 2.1.

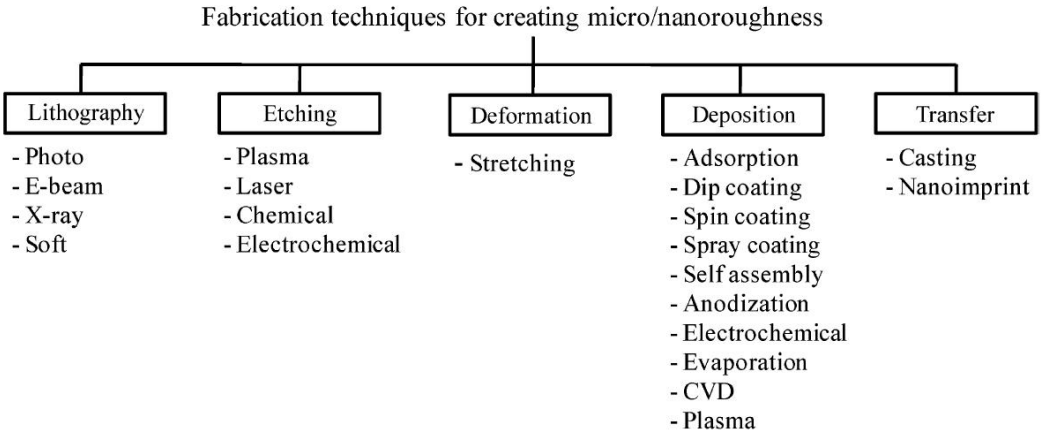

Figure 2.14: Various fabrication techniques for creating micro/nanostructures [25] .

Table 2.1: Pros and cons of different fabrication techniques [25].

Techniques	Pros	Cons
Lithography	Accuracy, large area	Slow process, high cost
Etching	Fast	chemical contamination, less control
Deposition	Flexibility, cheap	Can be high temperature, less control
Self-assembly	Flexibility, cheap	Require suitable precursor

A prerequisite for putting such surfaces to work in optics and glass is transparency, which necessitates the surface roughness scale smaller than the wavelength of visible light (400-700 nm).

Two key components for building a superhydrophobic surface are roughness and hydrophobicity. According to the process to render these surfaces superhydrophobic, Kim [33] categorized the fabrication approaches into three groups: 1) roughing hydrophobic materials, 2) making rough structures followed by hy-

drophobic treatments, 3) depositing hydrophobic materials with rough textures.

2.7.1 Roughening hydrophobic materials

Flat poly(tetrafluoroethylene) (PTFE) surfaces usually have a water contact angle of 115-120°. After treatment with plasma etching, the widely used method for fluorinated polymers, water contact angles on these surfaces can be increased to 170° [63]. PTFE surfaces can also be simply stretched to double their original length to create additional micro roughness.

Poly(dimethylsiloxane) (PDMS) is another hydrophobic polymer that can be easily treated with laser abrasion to created micro- and nano-structures which ensure large contact angles and small roll-off angles. After processed as an oligomeric liquid form, PDMS can be cured into a solid to duplicate surface textures. Lotus leaf like PDMS surface has been fabricated by this process [64]. Similarly, hydrophobic hydrocarbon polymers, such as paraffin [65] and wax crystals [8, 28, 66] can also be processed by plasma etching to impart superhydrophobic properties on surface.

2.7.2 Hydrophobic treatments of roughened surfaces

Theoretically, delicate roughing can render any surfaces superhydrophobic. More widely, material surfaces are roughened first and followed by hydrophobic treatments. Roughness can be created on polycrystalline metal surfaces by chemical etching [67, 68], on polymer surfaces and glass by plasma process [69], on silicon surfaces by high power pulsed laser [69]. Qian and Shen [67] carried out simple chemical etching by immersing polycrystalline metals in a Becks dislocation

etchant at room temperature and subsequently hydrophobized the etched surface with a fluoroalkylsilane solution in methanol. The use of a Becks dislocation etchant ensured the preferential dissolving of the dislocation sites on the surface which led to surface roughness.

Techniques used widely in semiconductor process, photo-lithography and electron beam lithography, have been applied to periodic micro-patterning with accurate control of dimensions and shapes [30].

Nanosphere lithography has also been developed for nano-patterning by depositing mono-dispersed polystyrene or silica nanoparticles in a lattice array [70]. Various nanowires and nanotubes have been synthesized or dispersed vertically on smooth surfaces by chemical vapour deposition. A second chemical vapour deposition makes these surfaces remarkably superhydrophobic [71].

Another popular method is lay-by-layer thin film deposition. Charged polyelectrolytes or nanoparticles are deposited on the surface according to electrostatic interactions and hydrogen bonding. The film thickness and roughness can be precisely manipulated by varying particle size and deposition conditions. These films are thereafter fluorinated on the outmost layer to achieve superhydrophobicity [72, 73]. Metals and conductive polymers can be deposited lay-by-layer in an electrochemical process.

Sol-gel process is a widely used method to create porous rough surface by including a secondary component in the process and removing it with hot water or sublimation. Hydrophobic treatments include fluorinated silane coating [74].

2.7.3 Depositing hydrophobic materials with rough topography

Creating both roughness and low surface energy surface in one single step is desirable and efficient. In a sol-gel phase-separation process [75], hydrophobicity has been achieved on the organo-functionlized inorganic precursors when the conditions are carefully adjusted. Electrospinning, a popular technique used to make ultra-thin polymer fibre, can work with hydrophobic polymers and produce superhydrophobic fibre mats on the collector [76]. Plasma polymerization has been applied on fluorinated carbon films with certain roughness to induce multi-scale structures that leads to superhydrophobicity [77].

References

[1] Thomas Young. An essay on the cohesion of fluids. *Philosophical Transactions of the Royal Society of London*, 95:65–87, 1805. 11, 15, 16

[2] Robert N. Wenzel. Resistance of solid surfaces to wetting by water. *Industrial Engineering Chemistry*, 28(8):988–994, 1936. 11, 17

[3] A. B. D. Cassie and S. Baxter. Wettability of porous surfaces. *Transactions of the Faraday Society*, 40:546–551, 1944. 11

[4] W. Barthlott and C. Neinhuis. Purity of the sacred lotus, or escape from contamination in biological surfaces. *Planta*, 202:1–8, 1997. 11, 28

[5] rame-hart instrument co. rame-hart information on surface and interfacial

tension. http://www.ramehart.com/. Retrieved on Oct 20, 2013. Slightly modified. 12

[6] Bharat Bhushan. Biomimetics inspired surfaces for drag reduction and oleophobicity/philicity. *Beilstein Journal of Nanotechnology*, 2:66–84, 2011. 12

[7] MesserWoland. Wetting. http://en.wikipedia.org/wiki/Wetting. Retrieved on Oct 25, 2013. Slightly modified. 13

[8] Bharat Bhushan, Yong Chae Jung, Adrian Niemietz, and Kerstin Koch. Lotus-like biomimetic hierarchical structures developed by the self-assembly of tubular plant waxes. *Langmuir*, 25(3):1659–1666, 2009. 14, 37

[9] Peter Forbes. Self-cleaning materials: Lotus leaf-inspired nanotechnology. *Scientific American*, 299 (2):88–95, 2008. 14, 29

[10] Michael Steden. Drops art. http://blog.romandavydov.com/. Retrieved on Sep 30, 2013. 15

[11] GA Sto Corp., Atlanta. http://www.asknature.org/media/image/11200. Retrieved on Sep 10, 2013. 15

[12] Hydrophobe. http://www.answers.com/topic/hydrophobe-1. Retrieved on Oct 17, 2013. Slightly modified. 16

[13] L. Boruvka and A. W. Neumann. Generalization of the classical theory of capillarity. *Journal of Chemical Physics*, 66:5464–5476, 1977. 16

[14] Z. Zander. Wetting. http://en.wikipedia.org/wiki/Wetting. Retrieved on Sep 25, 2013. Slightly modified. 17

[15] Christian Borgs, Joel De Coninck, Roman Kotecky, and Murielle Zinque. Does the roughness of the substrate enhance wetting? *Physical Review Letters*, 74:2292–2294, 1995. 18

[16] Abraham Marmur. Wetting on hydrophobic rough surfaces: To be heterogeneous or not to be? *Langmuir*, 19(20):8343–8348, 2003. 18, 21

[17] Gene Whyman, Edward Bormashenko, and Tamir Stein. The rigorous derivation of young, cassie-baxter and wenzel equations and the analysis of the contact angle hysteresis phenomenon. *Chemical Physics Letters*, 450:355–359, 2008. 19

[18] Michael Nosonovsky and Bharat Bhushan. Patterned nonadhesive surfaces: Superhydrophobicity and wetting regime transitions. *Langmuir*, 24:1525–1533, 2008. 19, 20

[19] Edward Bormashenko, Roman Pogreb, and Gene Whyman. Comment on water wetting transition parameters of perfluorinated substrates with periodically distributed flat-top microscale obstacles. *Langmuir*, 25(23):13694–13695, 2009. 21

[20] C. W. Extrand. Model for contact angles and hysteresis on rough and ultraphobic surfaces. *Langmuir*, 18:7991–7999, 2002. 21

[21] Shutao Wang and Lei Jiang. Definition of superhydrophobic states. *Advanced Materials*, 19:3423–3424, 2007. 21

[22] Aurelie Lafuma and David Quvre. Superhydrophobic states. *Nature Materials*, 2:457–460, 2003. 21

[23] Neelesh A. Patankar. On the modeling of hydrophobic contact angles on rough surfaces. *Langmuir*, 19(4):1249–1253, 2003. 21

[24] Michael Nosonovsky and Bharat Bhushan. Biologically-inspired surfaces: broadening the scope of roughness. *Advanced Functional Materials*, 18:843–855, 2008. 22

[25] Bharat Bhushan and Yong Chae Jung. Natural and biomimetic artificial surfaces for superhydrophobicity, self-cleaning, low adhesion, and drag reduction. *Progress in Materials Science*, 56(1):1–108, 2011. 23, 35, 36

[26] J. D. Andrade. *Surface and Interfacial Aspects of Biomedical Polymers (Vol. 1)*. Plenium Press, NY, 1985. 22

[27] Michael Nosonovsky and Bharat Bhushan. Hierarchical roughness makes superhydrophobic surfaces stable. *Microelectron Engineering*, 84:382–386, 2007. 24

[28] Kerstin Koch, Bharat Bhushan, Yong Chae Jung, and Wilhelm Barthlott. Fabrication of artificial lotus leaves and significance of hierarchical structure for superhydrophobicity and low adhesion. *Soft Matter*, 5:1386–1393, 2009. 25, 37

[29] Michael Nosonovsky and Bharat Bhushan. Do hierarchical mechanisms of superhydrophobicity lead to self-organized criticality? *Scripta Materialia*, 59:941–944, 2008. 25

[30] Reiner Furstner, Wilhelm Barthlott, Christoph Neinhuis, and Peter Walzel.

Wetting and self-cleaning properties of artificial superhydrophobic surfaces. *Langmuir*, 21:956–961, 2005. 26, 38

[31] Lichao Gao and Thomas J. McCarthy. The lotus effect explained: two reasons why two length scales of topography are important. *Langmuir*, 22: 2966–2967, 2006. 26

[32] C. Neinhuis and W. Barthlott. Characterization and distribution of water-repellent, self-cleaning plant surfaces. *Annals of Botany*, 79(6):667–677, 1997. 26, 28

[33] Seong H. Kim. Fabrication of superhydrophobic surfaces. *Journal of Adhesion Science and Technology*, 22:235–250, 2008. 26, 33, 36

[34] Thomas Wagner, Christoph Neinhuis, and Wilhelm Barthlott. Wettability and contaminability of insect wings as a function of their surface sculptures. *Acta Zoologica*, 77:213–225, 1996. 26

[35] Woo Lee, Mi-Kyoung Jin, Won-Cheol Yoo, and Jin-Kyu Lee. Nanostructuring of a polymeric substrate with well-defined nanometer-scale topography and tailored surface wettability. *Langmuir*, 20:7665–7669, 2004. 26

[36] Xuefeng Gao and Lei Jiang. Water-repellent legs of water striders. *Nature*, 432:36, 2004. 26

[37] Andrew R. Parker and Chris R. Lawrence. Water capture by a desert beetle. *Nature*, 414:33–34, 2001. 27

[38] P. E. Kolattukudy. Biopolyester membranes of plants: cutin and suberin. *Science*, 208:990–1000, 1980. 27

[39] Hendrik Bargel, Kerstin Koch, Zdenek Cerman, and Christoph Neinhuis. Structure-function relationships of the plant cuticle and cuticular waxes — a smart material? *Functional Plant Biology*, 33:893–910, 2006. 27

[40] C. E. Jeffree, R. P. C. Johnson, and P. G. Jarvis. Epicuticular wax in the stomatal antechambers of sitka spruce, and its effect on the diffusion of water vapor and carbon dioxide. *Planta*, 98:1–10, 1971. 28

[41] D. J. Royle. *Structural features of resistance to plant diseases. In 'Biochemical Aspects of Plant-Parasite Relationships'.* Academic Press: London, 1976. 28

[42] H. N. Barber. Adaptive gene substitutions in tasmanian eucalypts: I. genes controlling the development of glaucousness. *Evolution*, 9:1–14, 1955. 28

[43] P. E. Kolattukudy. *Cutin, suberin and waxes. In 'The Biochemistry of Plants. Volume 4, Lipids, Structure and Function'.* Academic Press: New York, 1980. 28

[44] S. A. Robinson, C. E. Lovelock, and C. B. Osmond. Wax as a mechanism for protection against photoinhibition-a study of cotyledon orbiculata. *Botanica Acta*, 106:307–312, 1993. 28

[45] Elena Gorb, Dagmar Voigt, Sanford D. Eigenbrode, and Stanislav Gorb. Attachment force of the beetle cryptolaemus montrouzieri (coleoptera, coccinellidae) on leaflet surfaces of mutants of the pea pisum sativum (fabaceae) with regular and reduced wax coverage. *Arthropod-Plant Interactions*, 2:247–259, 2008. 28

[46] Penelope B. Edwards. Do waxes on juvenile eucalyptus leaves provide protection from grazing insects? *Australian Journal of Ecology*, 7:347–352, 1982. 31

[47] P. L. Phelan and J. R. Miller. Post-landing behavior of alate myzus persicae as altered by (e)-beta-farnesene and three carboxylic acids. *Entomologia Experimentalis et Applicata*, 32:46–53, 1982. 28

[48] E. A. Baker and E. Parsons. Scanning electron microscopy of plant cuticles. *Journal of Microscopy*, 94:39–49, 1971. 28

[49] Lin Feng, Yanan Zhang, Jinming Xi, Ying Zhu, Nu Wang, Fan Xia, and Lei Jiang. Petal effect: A superhydrophobic state with high adhesive force. *Langmuir*, 24:4114–4119, 2008. 29, 30, 31

[50] Bharat Bhushan and Eun Kyu Her. Fabrication of superhydrophobic surfaces with high and low adhesion inspired from rose petal. *Langmuir*, 26(11):8207–8217, 2010. 30

[51] N. D. Hallam and T. C. Chambers. The leaf waxes of the genus eucalyptus l'heritier. *Australian Journal of Botany*, 18:335–386, 1970. 31

[52] D. H. S. Horn, Z. H. Kranz, and J. A. Lamberton. The composition of eucalyptus and some other leaf waxes. *Australian Journal of Chemistry*, 17: 464–476, 1964. 31

[53] Eric B. Brennan and Steven A. Weinbaum. Effect of epicuticular wax on adhesion of psyllids to glaucous juvenile and glossy adult leaves of eucalyptus

globulus labillardire. *Australian Journal of Entomology*, 40:270–277, 2001. 32

[54] Eric B. Brennan and Steven A. Weinbaum. Stylet penetration and survival of three psyllid species on adult leaves and 'waxy' and 'de-waxed' juvenile leaves of eucalyptus globulus. *Entomologia Experimentalis et Applicata*, 100: 355–363, 2001. 32

[55] Tao Liu, Yansheng Yin, Shougang Chen, Xueting Chang, and Sha Cheng. Super-hydrophobic surfaces improve corrosion resistance of copper in seawater. *Electrochimica Acta*, 52(11):3709–3713, 2007. 32

[56] A. J. Scardino, H. Zhang, D. J. Cookson, R. N. Lamb, and R. de Nys. The role of nano-roughness in antifouling. *Biofouling*, 25(8):757–767, 2009. 33

[57] Richard Truesdell, Andrea Mammoli, Peter Vorobieff, Frank van Swol, and C. Jeffrey Brinker. Drag reduction on a patterned superhydrophobic surface. *Physical Review Letters*, 97:044504, 2006. 33

[58] Glen McHale, Michael I. Newton, and Neil J. Shirtcliffe. Immersed superhydrophobic surfaces: Gas exchange, slip and drag reduction properties. *Soft Matter*, 6:714–719, 2010. 33, 34

[59] A. Y. Vorobyev and Chunlei Guo. Water sprints uphill on glass. *Journal of Applied Physics*, 108:123512–123512–4, 2010. 34

[60] Leonid Ionov, Nikolay Houbenov, Alexander Sidorenko, Manfred Stamm, and Sergiy Minko. Smart microfluidic channels. *Advanced Functional Materials*, 16:1153–1160, 2006. 34

[61] Lei Zhai, Michael C. Berg, Fevzi C. Cebeci, Yushan Kim, John M. Milwid, Michael F. Rubner, and Robert E. Cohen. Patterned superhydrophobic surfaces: Toward a synthetic mimic of the namib desert beetle. *Nano Letters*, 6(6):1213–1217, 2006. 35

[62] Yongmei Zheng, Hao Bai, Zhongbing Huang, Xuelin Tian, Fu-Qiang Nie, Yong Zhao, Jin Zhai, and Lei Jiang. Directional water collection on wetted spider silk. *Nature*, 463:640–643, 2010. 35

[63] M. Morra, E. Occhiello, and F. Garbassi. Contact angle hysteresis in oxygen plasma treated poly(tetrafluoroethylene). *Langmuir*, 5:872–876, 1989. 37

[64] Manhui Sun, Chunxiong Luo, Luping Xu, Hang Ji, Qi Ouyang, Dapeng Yu, and Yong Chen. Artificial lotus leaf by nanocasting. *Langmuir*, 21:8978–8981, 2005. 37

[65] F. E. Bartell and J. W. Shepard. The effect of surface roughness on apparent contact angles and on contact angle hysteresis. i. the system paraffin-water-air. *The Journal of Physical Chemistry*, 57:211–215, 1953. 37

[66] Bharat Bhushan, Kerstin Koch, and Yong Chae Jung. Biomimetic hierarchical structure for self-cleaning. *Applied Physics Letters*, 93:093101–093101–3, 2008. 37

[67] Baitai Qian and Ziqiu Shen. Fabrication of superhydrophobic surfaces by dislocation-selective chemical etching on aluminum, copper, and zinc substrates. *Langmuir*, 21(20):9007–9009, 2005. 37

[68] Zhiguang Guo, Feng Zhou, Jingcheng Hao, and Weimin Liu. Stable

biomimetic super-hydrophobic engineering materials. *Journal of the American Chemical Society*, 127:15670–15671, 2005. 37

[69] Xiaoyan Song, Jin Zhai, Yilin Wang, and Lei Jiang. Fabrication of superhydrophobic surfaces by self-assembly and their water-adhesion properties. *The Journal of Physical Chemistry B*, 109(9):4048–4052, 2005. 37

[70] Gang Zhang, Dayang Wang, Zhong-Ze Gu, and Helmuth Mohwald. Fabrication of superhydrophobic surfaces from binary colloidal assembly. *Langmuir*, 21:9143–9148, 2005. 38

[71] K. K. S. Lau, J. Bico, K. B. K. Teo, M. Chhowalla, G. A. J. Amaratung, W. I. Milne, G. H. McKinley, and K. K. Gleason. Superhydrophobic carbon nanotube forests. *Nano Letters*, 3:1701–1705, 2003. 38

[72] Joong Tark Han, Yanli Zheng, Jeong Ho Cho, Xurong Xu, and Kilwon Cho. Stable superhydrophobic organic-inorganic hybrid films by electrostatic self-assembly. *The Journal of Physical Chemistry B*, 109:20773–20778, 2005. 38

[73] Lei Zhai, Fevzi C. Cebeci, Robert E. Cohen, and Michael F. Rubner. Stable superhydrophobic coatings from polyelectrolyte multilayers. *Nano Letters*, 4:1349–1353, 2004. 38

[74] Masashi Miwa, Akira Nakajima, Akira Fujishima, Kazuhito Hashimoto, and Toshiya Watanabe. Effects of the surface roughness on sliding angles of water droplets on superhydrophobic surfaces. *Langmuir*, 16:5754–5760, 2000. 38

[75] N. J. Shirtcliffe, G. McHale, M. I. Newton, and C. C. Perry. Intrinsically

superhydrophobic organosilica sol-gel foams. *Langmuir*, 19:5626–5631, 2003. 39

[76] Anurima Singh, Lee Steely, and Harry R. Allcock. Poly[bis(2,2,2-trifluoroethoxy)phosphazene] superhydrophobic nanofibers. *Langmuir*, 21: 11604–11607, 2005. 39

[77] Atsushi Hozumi and Osamu Takai. Preparation of silicon oxide films having a water-repellent layer by multiple-step microwave plasma-enhanced chemical vapor deposition. *Thin Solid Films*, 334:54–59, 1998. 39

Chapter 3

Water Repellency of Selected Australian Native Leaves and Diatoms

3.1 Introduction

Water repellency is found widely on plants in habitats ranging from tropical to arid and in live forms from herbaceous to ligneous [1]. The different water repellent behaviours on the leaves of various plants, such as lotus (*Nelumbo nucifera*), Indian Cress (*Tropaeolum majus*) and Lady's Mantle (*Alchemilla vulgaris*), can be related to survival strategies for specific environments and ecosystems.

Generally, hydrophobicity is essential for plant leaves to avoid pathogenic organisms, dust contamination and stomata blockage. Strong hydrophobicity is usually found on water plants, for which there is excessive water. Moderate hydrophobicity is observed on plants in arid or semi-arid environments. Different

degrees of hydrophobicity, for example, the lotus effect [1] and the petal effect [2], relate to applications in self-cleaning [3] and micro-volume liquid transfer [4]. Given that millions of floral species developed certain types of wettability over billions years of evolution [5], it might be worthwhile to investigate leaf surface structures, which can bio-inspire the design and fabrication of artificial hydrophobic surfaces for different applications.

As single celled organisms floating in the ocean, diatoms cause tedious problems for marine vessels due to biofilm formation on the hulk. Adhesion strength of diatoms is generally associated with surface wettability. Diatom cells usually adhere firmer to hydrophobic surfaces than to hydrophilic surfaces. Understanding the wettability of diatoms could assist the development of marine antifouling coatings.

In this chapter, a few native Australian species were selected to assess their surface structures and leaf hydrophobicity. Different morphologies were divided to categories and their possible mechanisms of hydrophobicity were discussed. Furthermore, special wetting properties, such as directional hydrophobicity, were investigated. A model was constructed based on the geometry of diatoms and a surface free energy analysis was carried out on the model to study the hydrophobicity of diatoms.

3.2 Experimental procedure

3.2.1 Sample collection and preparation

Fresh leaves of 26 native Australian plant species were collected from actively growing specimens in the nursery at the State botanic garden, Kings Park in Perth, Western Australia. Table 3.1 lists the species studied and their epidermal relief.

Squares of 100 mm^2 were carefully excised from the abaxial side of these leaves for optical observation and contact angle measurements. Smaller squares of 4 mm^2 cut from these leaves were freeze-dried prior to SEM examination using an Emitech K775X Turbo Freeze Dryer (Quorum Technologies Ltd, Kent, UK). The following time-temperature path was adopted: holding at -120 °C for the first 5 min, then gradually rising to -65 °C over a period of 14 hrs and finally increasing to room temperature over 10 hrs.

3.2.2 Instrumentation

Contact angle measurements were performed at ambient temperatures using an FTA1000 Drop Shape Analysis instrument (B Frame System, First Ten Angstroms, Virginia, USA) equipped with an automated dispensing syringe and a computer-controlled tilt stage. To ensure an even surface for water dispersal, leaf samples were fixed on the stage by double-sided adhesive tape before the application of 5 μL water droplets. The average water contact angle (n = 5) was obtained by analysing the sessile drop images using Drop Shape Analysis software affiliated with the goniometer. In order to measure roll-off angles, the stage tilt angle was

Table 3.1: Selected native Australian plant species for hydrophobic investigation.

Sample No.	Species	Epidermis description
S#1	*Scaevola globosa*	Hairy (medium)
S#2	*Anthotroche pannosa*	Hairy (medium)
S#3	*Lachnostachys verbascifolia*	Hairy
S#4	*Dicrastylis fulva*	Hairy (medium)
S#5	-[a]	(sample lost)
S#6	*Keraudrenia velutina ssp. velutina*	Convex
S#7	*Pimelea sylvestris*	Papillose
S#8	*Eucalyptus woodwardii*	Papillose (glaucous)
S#9	*Eucalyptus pruinosa*	Papillose (glaucous)
S#10	*Melaleuca globifera*	Smooth
S#11	*Corymbia confertiflora*	Convex
S#12	-[a]	Smooth (sample lost)
S#13	*Cyanostegia angustifolia*	Papillose
S#14	*Cycas pruinosa*	Convex (glaucous)
S#15	*Conostylis robusta*	Convex
S#16	*Thomasia macrocarpa*	Hairy (minor)
S#17	*Banksia petiolaris*	Hairy (back)
S#18	*Eucalyptus pachyphyllaa*	Smooth
S#19	*Eucalyptus species*	Papillose
S#20	*Eucalyptus dolorosa*	Convex
S#21	*Eucalyptus eudesmioides*	Convex (glaucous)
S#22	*Eucalyptus eudesmioides*	(duplicate sample)
S#23	*Eucalyptus oxymitra*	Convex
S#24	*Eremophila hillii*	Hairy (minor)
S#25	*Eucalyptus lane - poolei*	Convex
S#26	*Eucalyptus gomphocephala*	Convex

[a]Sample was lost during preparation and only partial data was obtained.

gradually increased at a speed of 1 deg/sec from 0° until the point where the water droplet began to move along the stage.

Optical images were obtained using a Moticam 2300 digital camera (Motic Instruments Inc., B.C., Canada).

For Scanning Electron Microscopy (SEM) analysis, specimens were mounted

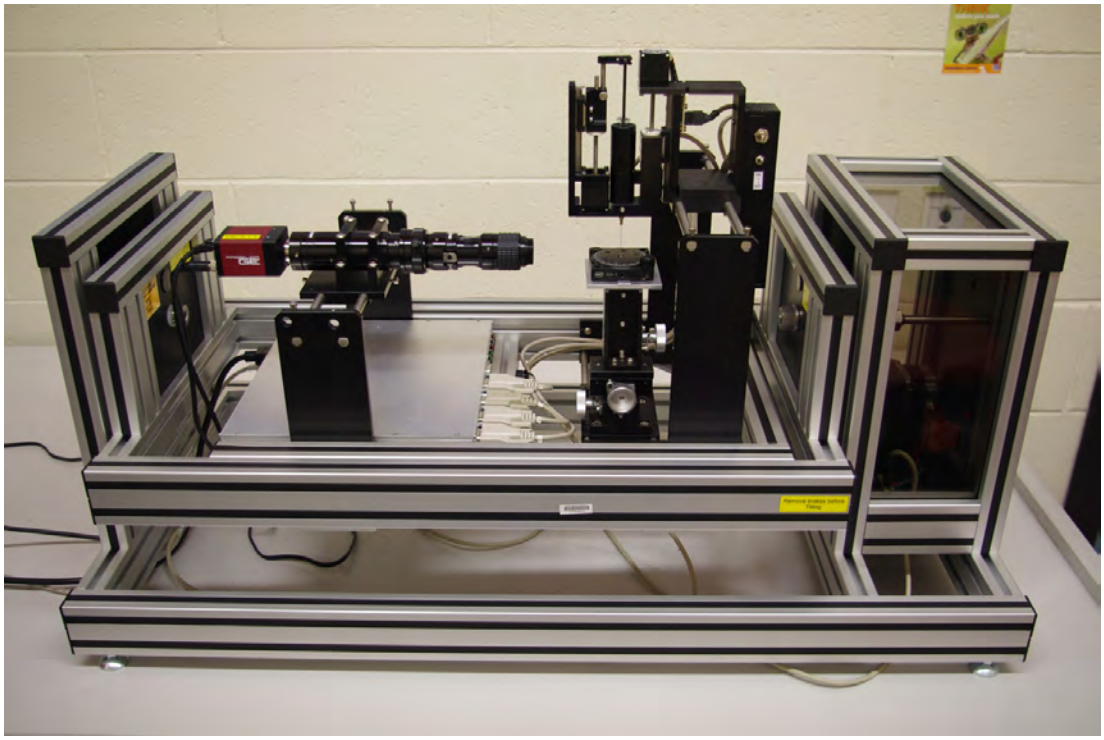

Figure 3.1: An FTA1000 Drop Shape Analysis instrument (system control and data analysis on a desktop not shown).

on aluminium stubs with carbon tabs prior to being sputter-coated with 10 nm carbon and 3 nm platinum. SEM imaging was conducted at 10 kV accelerating voltage and a working distance of 10 mm using a field-emission SEM (Zeiss VP1555, Oberkochen, Germany). Other operating parameters were: aperture size = 30.00 μm, signal = SE2, gun vacuum = 1.30×10^{-10} Torr. Ten measurements of surface features were performed on each SEM image, from which the average and standard deviation values were derived.

3.3 Results and discussion

Various wetting conditions were observed on the study species. Water tends to spread out on some plant leaf surfaces, such as S#10, S#12, S#14, S#17, and S#18, and forms contact angles in the range 30°–85°. As shown in Fig. 3.2a, these hydrophilic leaves tend to have a glossy and smooth surface. For the other species, however, water droplets form spherical shapes with contact angles in the range 110°–140° (Fig. 3.2b) and usually 5 μL droplets stick firmly to the leaf surface when it is tilted gradually from 0° to 180°.

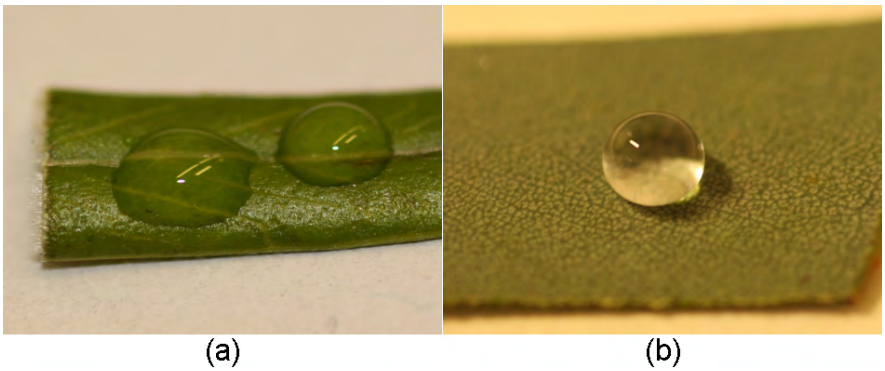

Figure 3.2: Typical hydrophilic and hydrophobic native Australian plant leaves: (a) S#12 and (b) S#25.

Based on the leaf surface topographies, the selected species were categorized into four groups (see Fig. 3.3): (a) hairy, (b) palm-tree-like, (c) papillae and (d) micro-ridge. Hairy leaves have a thick layer of hairs, of different morphologies, covering both the adaxial and abaxial leaf surfaces. Species S#1, S#2, S#3, S#4, S#5, and S#17 belong to this group. A palm-tree-like surface morphology, which is characterized by many micro-structures on the leaf surface with the shape of a palm tree, is found on species S#6, S#16 and S#24. Micropapillae cells are found on the surface of most of the *Eucalyptus* species studied. This

group include species S#7, S#8, S#9, S#11, S#18, S#19, S#20, S#21, S#22, S#23, S#25 and S#26. The last group, with micro-ridge topography is found on species S#15. While the *Eucalyptus* group that will be presented in a separate chapter, the surface morphology and wettability of other groups are individually discussed in this chapter.

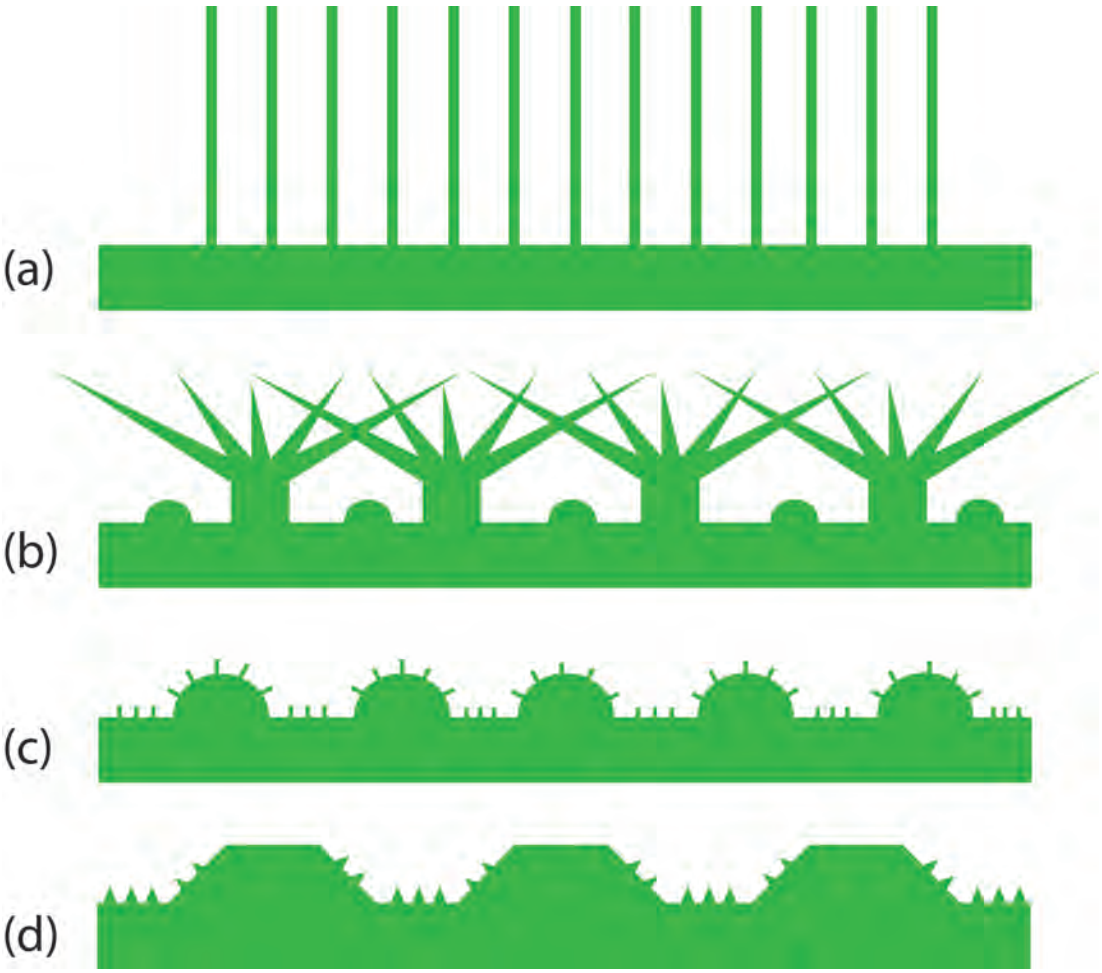

Figure 3.3: A schematic illustration of four categories of native leaves in this study (side view): (a) hairy, (b) palm-tree-like, (c) papillae, and (d) micro-ridge.

3.3.1 Hairy leaves

Hairy leaves have thick, fuzzy hairs covering the whole cuticle and therefore a physical protection layer is formed between the cuticle and the external environment (See Fig. 3.4).

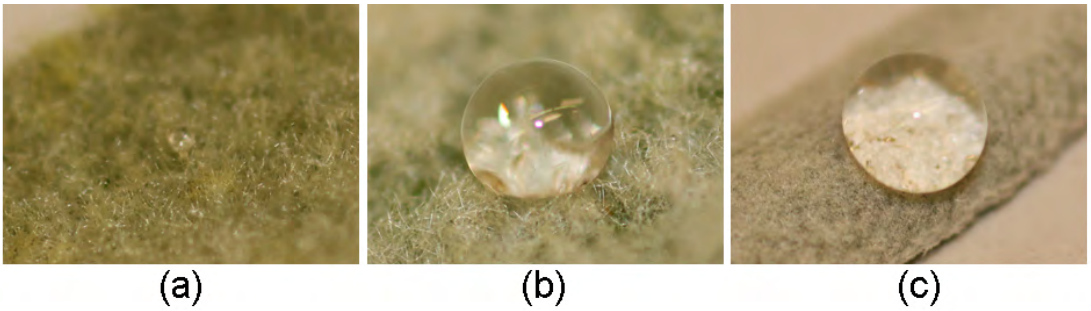

Figure 3.4: Water droplets on three hairy native Australian leaves: (a) S#1, (b) S#3, and (c) S#5.

In Table 3.2, water contact angle (WCA) values of less than 90° were observed on S#2. WCA values of greater than 115° were obtained on the three other species. Given the arid and dry environments in many parts of Australia, these leaves present surprisingly strong hydrophobicity. Additionally, water droplets of 5 μL stuck firmly to the leaf surfaces when the leaves were inverted. No droplet was observed to roll off in the leaf surface tilting experiments.

Table 3.2: WCA values of study hairy species (n=5).

Sample No.	Species	WCA (°)
S#1	*Scaevola globosa*	130.2 ± 1.8
S#2	*Anthotroche pannosa*	84.3 ± 2.3
S#3	*Lachnostachys verbascifolia*	115.7 ± 1.6
S#4	*Dicrastylis fulva*	121.0 ± 2.5
S#17	*Banksia petiolaris*	140.9 ± 1.9

The SEM images of three study species are shown in Fig. 3.5. Different topographies, including upright brushes, upstanding tree-like hairs and entangled fibre-like hairs, are evident on these leaf surfaces. Compared to the thickness of leaves that is determined as the distance between the cuticle layers on the front and back of the leaves, the hairs have lengths of at least three-fold greater magnitude. Micro-bumps of nearly 1 μm across were observed on some individual hairs of all three species in Fig. 3.5. The density projecting from the cuticle layers varies from one to another. The thick layer of hairs on the cuticle is believed to function as a mediator of moisture, radiation and air circulation.

These hairy leaves have entirely different morphologies to the well-established, multi-scale roughness of lotus [3] and may repel water with individual strategies. Researchers have identified contact angles below 60° along Lady's Mantle hairs, which indicates their hydrophilic properties [6]. A bundle of hairs lifted a water droplet deposited on the cuticula thus keeping that surface dry [6].

In the current study, when water comes into contact with upright hairs on the leaves, hairs are pulled together due to water surface energy. Therefore, they tend to narrow their distance and join together on the upper end. A bundle of neighbouring hairs thus stick into the water-air interface (Fig. 3.6a). Species S#1 is very likely to adopt this mechanism, as its hairs are relatively flexible.

The elasticity of hairs becomes critical for hydrophobicity, since most hairs have to bend in the process and the water-air interface moves towards the cuticula (substrate). The bending of the hairs leads to a repulsion interaction between the water-air interface and the cuticula. The elastic energy formed during the

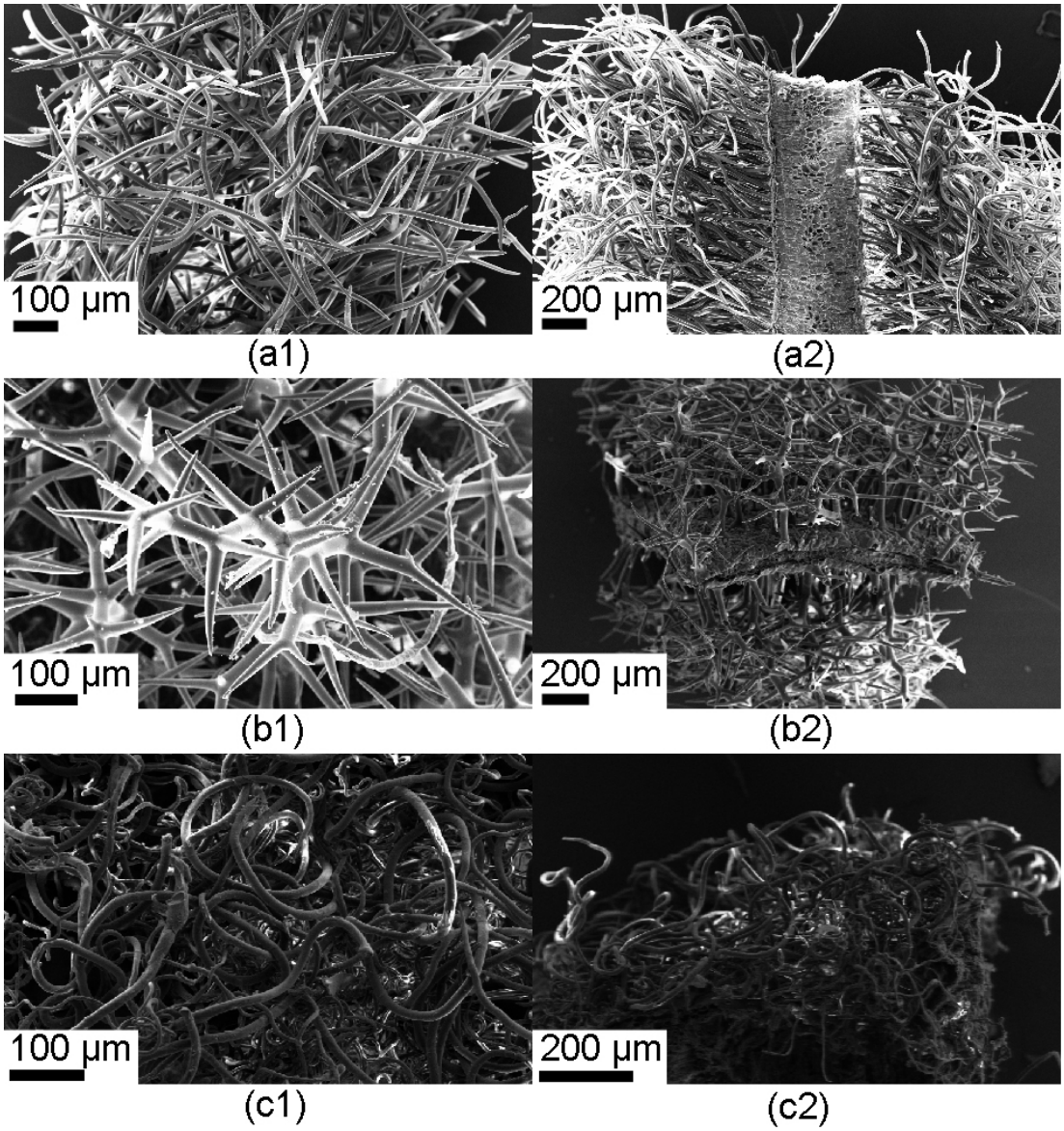

Figure 3.5: Top (1) and cross-section (2) views of three hairy native Australian leaves: (a) S#1, (b) S#2, and (c) S#17.

bending procedure can be expressed as [6]

$$\Gamma \propto \sqrt{K} h^{-1/2} \tag{3.1}$$

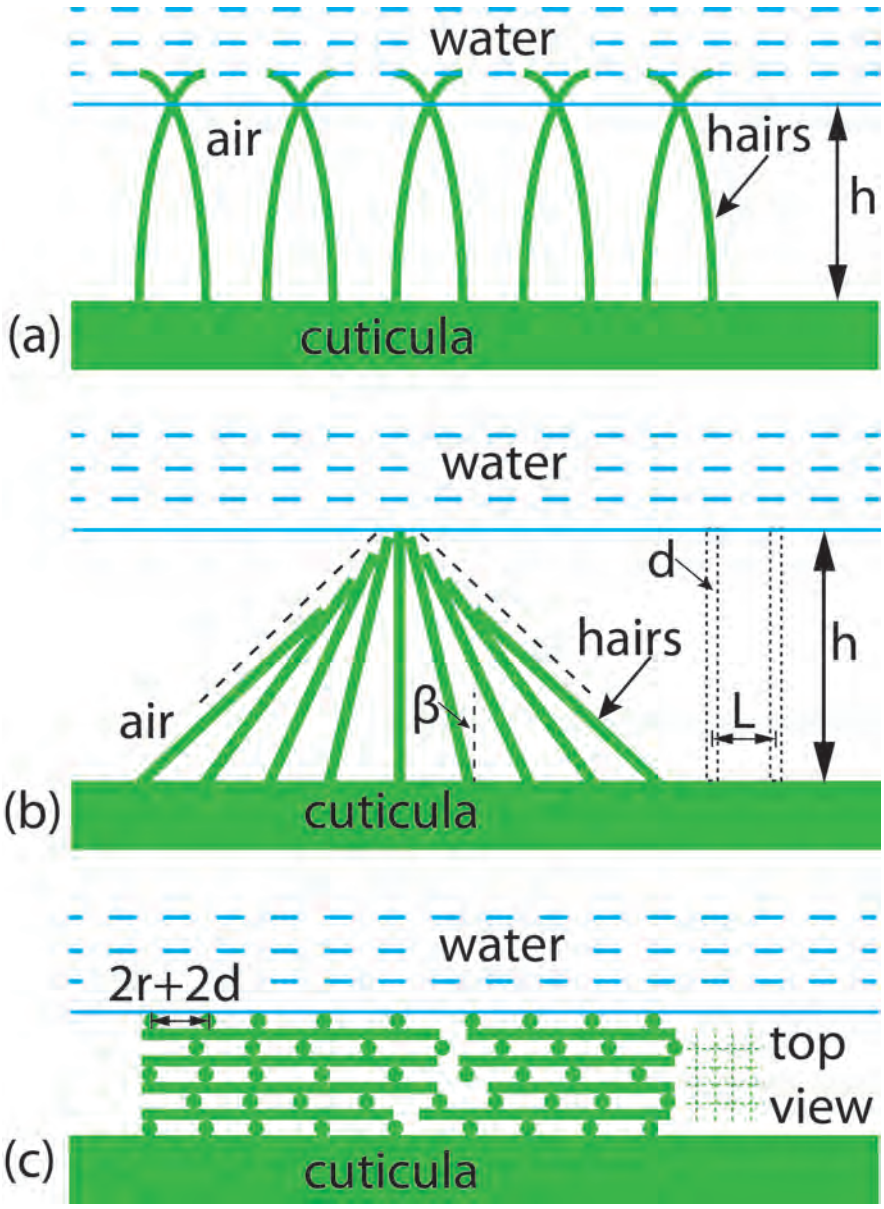

Figure 3.6: Possible hydrophobic mechanisms on hairy leaves: (a) elastic bundling [6], (b) pyramid bundling [7], and (c) layers of hair grids.

where Γ is the elastic energy contribution, K represents the elastic modulus and h is distance between the water-air interface and the cuticle.

In contrast to S#1, species S#2, S#3 and S#4 (Fig. 3.5b) have leaf hairs

arranged in a tree-like shape. Their relatively large hair diameter and spreading "twigs" limit flexibility and crossing over at the hair ends. A micro-pyramid formed after bundling, that is, several hairs move towards a central hair during the contact with water [7]. The sharpness of the micro-pyramid, described as β (the tilt angle of the nearest hair off the vertical direction) in Fig. 3.6b, can be expressed by the hair pitch value L, the hair diameter d, and the rod height h as follows [7]

$$h \sin \beta + \frac{1}{2} d \cos \beta = L - \frac{1}{2} d \tag{3.2}$$

The β solution of this equation indicates that the sharpness of the micro-pyramid increases monotonically with L but decreases with increasing values for d and h. As shown in Fig. 3.5b, the hair pitch value L approximates the leaf thickness ($\sim 200\mu$m) and is greater than the hair diameter d. Therefore sharp micro-pyramids with large β values are likely to form at wetting.

The thick hairs on the leaf surface of species S#17, which does not contain upright hairs, is suspected to repel water with a different method. The hairs growing parallel to the cuticle surface form many layers of grids, which can be analogized to that of fabrics. The rough surface asperities, formed among these grids help prevent water from entering this hair matrix and thus from wetting the cuticula. The fibre-like morphology of specimen S#17 has a surprisingly high WCA of $140.9 \pm 1.9°$, probably because of the close packing of both the hairs in the same layer and the multiple layers above the cuticula.

The apparent contact angle of water on arrays of cylinders, θ_D, can be described as [8]

$$cos\theta_D = f_1 \cos \theta_A - f_2 \tag{3.3}$$

with

$$f_1 = [\pi r/(r+d)](1 - \theta_A/180^\circ) \tag{3.4}$$

and

$$f_2 = 1 - r\sin\theta_A/(r+d) \tag{3.5}$$

where θ_A is the advancing contact angle, f_1 and f_2 are the fractions of solid-liquid and liquid-air contact area in the plane parallel to the substrate, respectively, r is the radius of the hair cylinder and d is half of the edge-to-edge distance between two neighbouring cylinders. The apparent contact angle θ_D increases with the value of $(r+d)/r$.

3.3.2 Palm-tree-like hairs

Palm-tree-like morphology (Fig. 3.7) was found on the leaves of three species (Table 3.3). Compared to tree-like hairs in the hairy category, the hairs of this group are smaller, less dense and each has a palm tree shape. The cuticula for these three species can be seen through the surface hairs.

WCA values greater than 130° were obtained on this type of leaf. Microscopic images show different densities of the surface micro-structures. Specimen S#6 has the largest density, with overlapping of branches covering above the cuticle, which leads to the highest WCA among these three leaves (Fig. 3.7a). Specimen S#16 has the lowest density, with each micro-structure being identified easily (Fig. 3.7b) and S#24 is intermediate (Fig. 3.7c).

SEM images of species S#6 and S#16 are shown in Fig. 3.8. The cross-section view shows these hairs have a short but thick trunk, the height and diameter of which are both less than 50 μm. Hairs greater than 300 μm are stretch from the

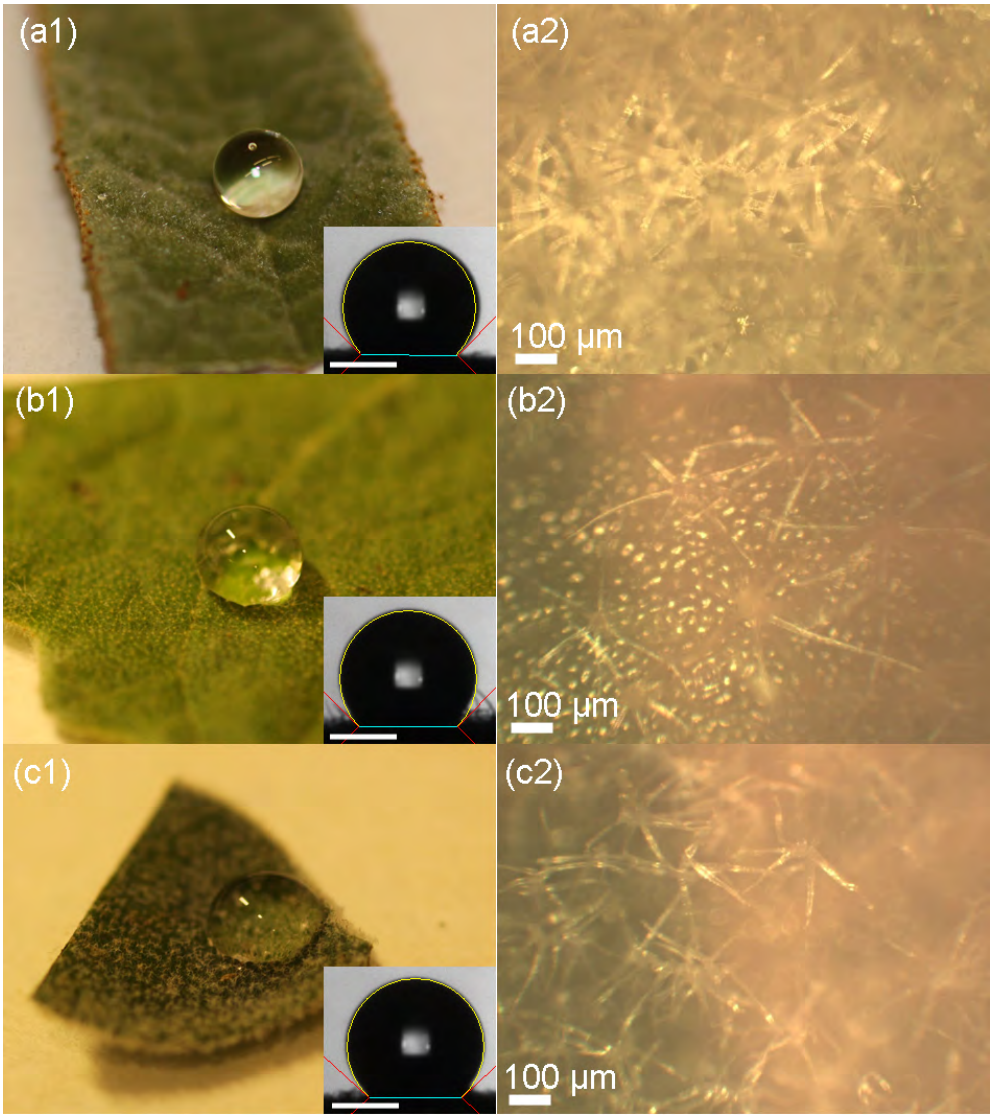

Figure 3.7: Water droplets (1) and optical top views (2) of three hairy native Australian leaves: (a) S#6, (b) S#16, and (c) S#24. Scale bars in droplet images in series (1) = 1 mm.

trunk to all directions. When water comes into contact with the leaf, it initially touches the tips of long hairs. Bundling of upper hairs is speculated to occur, and an elastic repellent layer is formed, similar to that depicted in Fig. 3.6a. If water does move along the hairs and it is likely to rest on the top of the trunks.

Table 3.3: WCA values of study species with palm-tree-like surface morphology.

Sample No.	Species	WCA (°)
S#6	*Keraudrenia velutina ssp. velutina*	138.6 ± 4.3
S#16	*Thomasia macrocarpa*	133.9 ± 2.7
S#24	*Eremophila hillii*	137.5 ± 3.2

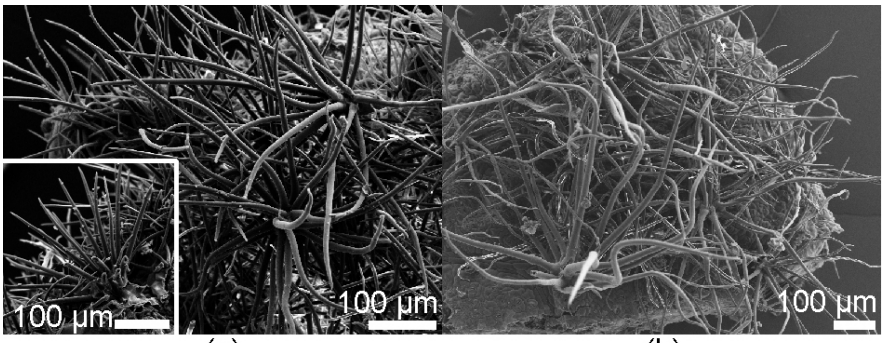

Figure 3.8: SEM images from top perspective: (a) S#6 (with cross-section view in inset) and (b) S#16.

Compared to *Salvinia*, a floating water fern that has hairs of a special egg-beater shape with hydrophilic tips [9], water pinning on the palm-tree-like hairs possibly occurs at the place where upper hairs are joined after bending. The palm-tree like hairs are likely to be hydrophobic, given the relatively large spacing between the upper hairs. Two potential mechanisms may keep the air-water interface away from the cuticula: (a) bent upper hairs create elastic forces to act against further water penetration into the region between the hairs; and (b) water penetration results in a further contact area between water and hydrophobic hairs, in which extra activation energy is required.

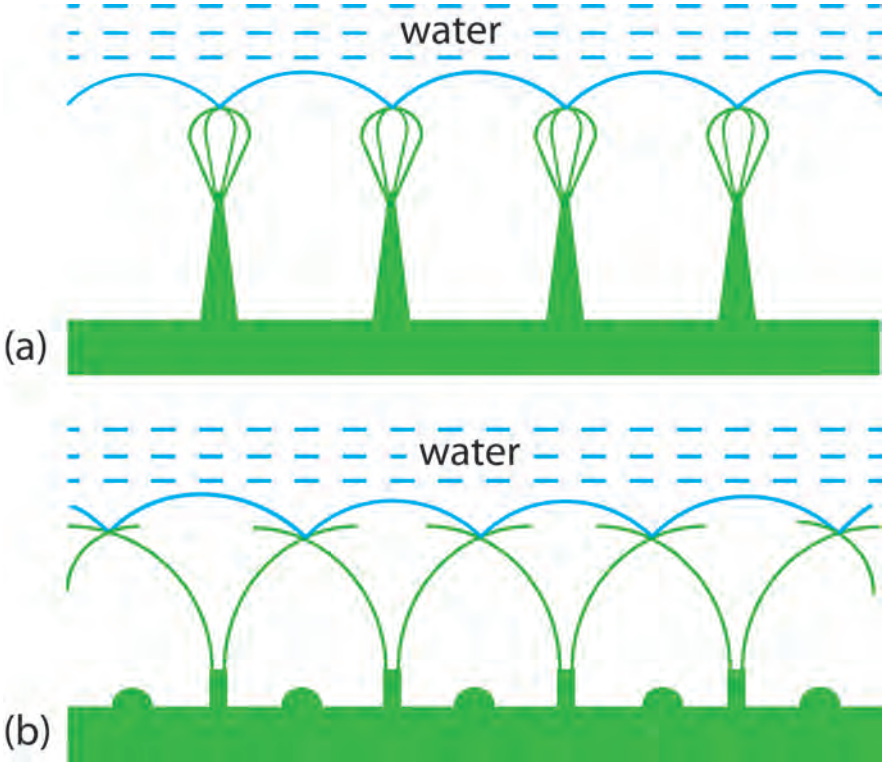

Figure 3.9: Proposed hydrophobic mechanisms on leaves: (a) pinning on hydrophilic tips of *Salvinia* hydrophobic hairs of an eggbeater shape [9] and (b) palm-tree-like hairs on S#6, S#6 and S#24.

3.3.3 Micro-ridge topography

The hydrophobic properties of the leaves of a native plant, *Conostylis robusta* (S#15), were also investigated. This grass-like perennial has a rhizomatous root system in sandy regions, while its flat leaves grow upright and are mechanically robust with distinct parallel micro-ridges stretching along the entire narrow leaf (Fig. 3.10).

Water forms a spherical droplet, on this species' leaf surface, which has a WCA value greater than 90°. The orientation of the micro-ridges has made wetting different on directions parallel or perpendicular to the micro-ridges (Fig. 3.11).

Figure 3.10: Live form of *Conostylis robusta* (S#15).

Firstly, different contact angles were obtained for these two directions: 125.7° for the perpendicular direction and 113.3° for the parallel direction. This distinct difference in WCA values indicates the leaf surface is more hydrophobic along the micro-ridges than in the perpendicular direction. Secondly, water droplets rolled off along the micro-ridges direction when the leaf was tilted to $23.5 \pm 5°$. The roll-off did not occur along the direction perpendicular to the micro-ridges even when the leaf was tilted to 90°. In nature, the leaves grow upright with a tilt angle of nearly 90° from the horizon, so rain or dew droplets of a few microlitres will immediately roll along the micro-ridges towards the root and in this way water is collected in sandy area for the root.

The SEM images of this leaf are shown in Fig. 3.12. The strips that clearly present on the leaf surface have an isosceles trapezoid shape when viewing from the cross-section perspective, with lengths of approximately 150 μm and 300 μm

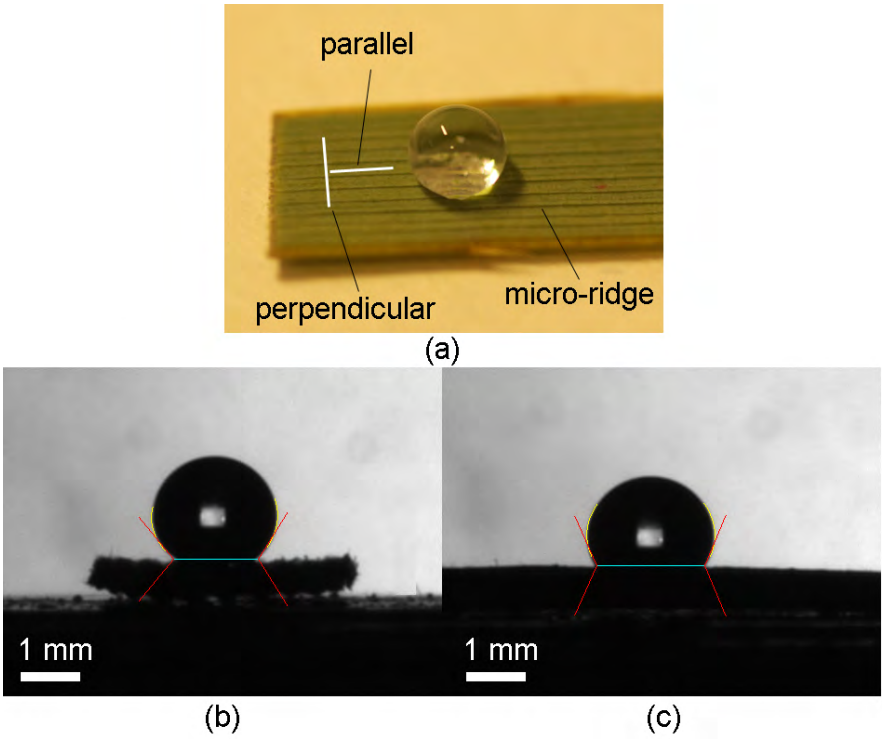

Figure 3.11: A water droplet on a *Conostylis robusta* leaf: (a) directions parallel and perpendicular to the micro-ridges, (b) with a contact angle of 125.7° measured from the direction perpendicular to the micro-ridges, (c) with a contact angle of 113.3° measured from the direction parallel to the micro-ridges.

for the top and bottom sides. The top sides of the strips are smooth with nano-scale grooves craved along the strips. Connecting the bottom sides of neighbouring bulging strips are the micro-ridges in the macroscopic scale. The topography of the micro-ridges is made of two components: randomly distributed micro-bumps and intermittent strips, which are both covered by thick plate wax.

3.3.4 Modelling of diatoms

Marine vessels and underwater structures are constantly subjected to severe attack through a process termed biofouling. When a surface is exposed to the

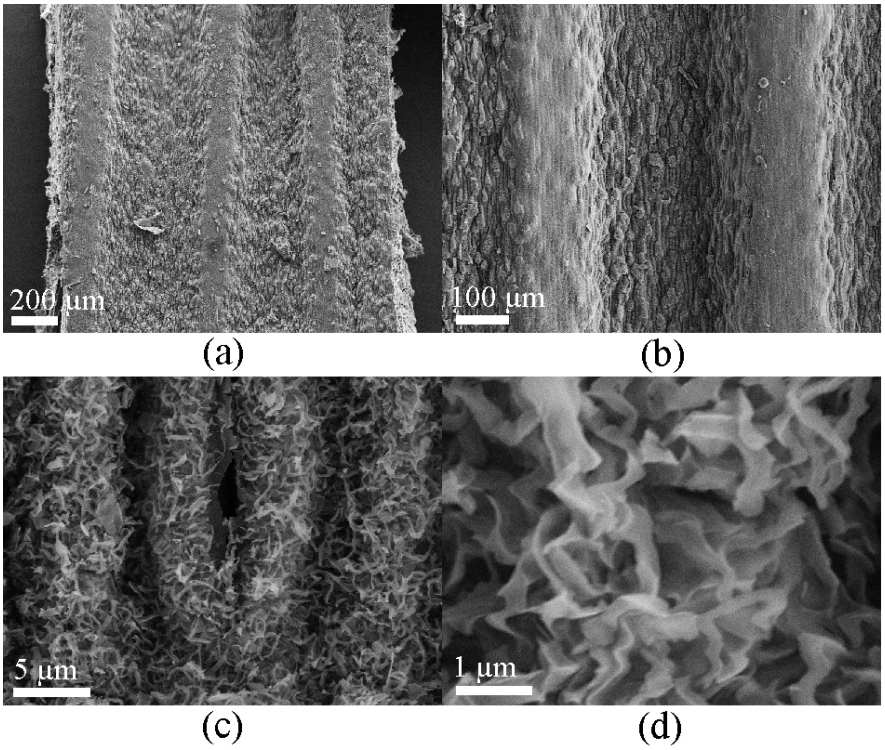

Figure 3.12: SEM images of a *Conoatylia robusta* leaf at different magnifications.

marine environment, microorganisms, such as bacteria and diatoms, begin to colonize the surface within hours and generate a complex biofilm incorporating an extracellular polymeric substance (EPS) matrix [10]. The formation of microfouling slimes, specifically on the ship hulls, can significantly increase the hydrodynamic drag and energy consumption, as well as reducing vessel's maneuverability [11]. Understanding the different stages of biofouling, including the initial adhesion and attachment, becomes critical in minimising its impact.

As dominating constituents in the biofouling slimes, diatoms are a diverse and abundant group of brown pigmented unicellular algae enclosed in a silica wall [12, 13]. They range in size from a few to several hundred microns. The highly complex SiO_2 structure of diatoms exhibits high porosity and a relatively

large surface area [14]. Diatoms can attach to a substratum (benthic diatoms) through adhesives or float freely in the water. The mucilaginous diatom EPS, which is predominantly composed of polysaccharides, mediates both attachment and motility, and enables diatoms to glide across surfaces. In some cases, the EPS can be transformed into attachment pads, tubes or even stalks [15].

Unlike many microorganisms that actively search for a suitable fouling surface, diatoms contact a surface passively through currents and gravity before selecting an attachment position [16]. Diatom slimes are reported to have higher attachment strength on hydrophobic surfaces and can stick to fouling release coatings on boats operating in excess of 30 knots [17]. The adhesion strength of diatoms is related to the surface wettability. Generally, diatoms adhere strongly to hydrophobic coatings, including silicone elastomers and fluorinated block copolymers and, conversely, adhere weakly to hydrophilic surfaces [18].

Diatom biofilms are of great interest, because they are highly resistant to antifouling coatings and are especially difficult to remove from non-toxic foul-release coatings [15]. The geometry of diatoms is modelled here in terms of its wettability underwater. Even though water tends to enter pores in a surface made of silica, the morphology of the external pores of diatom creates the possibility of geometrical air trapping [19], which prevents water from entering the pores and thus maintains surface hydrophobicity.

The external pores are simplified in the model as a spherical cavity (Fig. 3.14). The angle between the tangent of the highest point of the pore and the horizontal plane is ψ_0. The angle between the vertical plane and the liquid level in the pore, ψ, is also the current contact angle. When water enters the pore under external pressure, both ψ and the liquid-vapour interfacial area will increase. The free

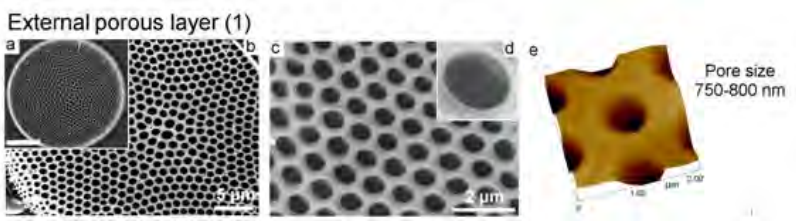

Figure 3.13: SEM and AFM micrographs of the diatom *Thalassiosira eccentrica* (Courtesy of Dr Dusan Losic, University of South Australia).

energy decrease due to wetting of the hydrophilic pore wall is counteracted by the liquid-vapour interfacial energy increase. The maximum energy is obtained when ψ reaches θ_Y, the Young's contact angle. Further water penetration will lead to a Wenzel state (ψ=π).

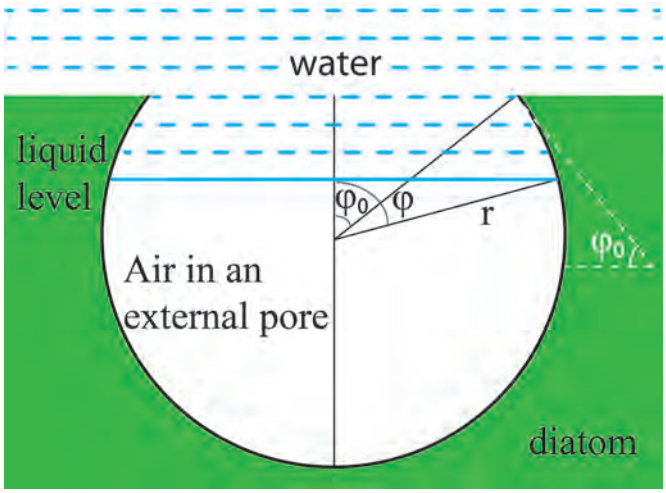

Figure 3.14: A spherical cavity model of an external pore on diatoms.

In the cavity, the surface free energy can be described as the sum of surface

energies at three interfaces [20]

$$\begin{aligned} E_{surf} &= \gamma_{LV} S_{LV} + \gamma_{SV} S_{SV} + \gamma_{LS} S_{LS} \\ &= \gamma_{LV} \pi (r \sin\psi)^2 + \gamma_{SV} 2\pi r^2 (\cos\psi_0 - \cos\psi) + \gamma_{LS} [4\pi r^2 - 2\pi r^2 (1 - \cos\psi)] \\ &= \gamma_{LV} \pi r^2 \sin^2\psi + \gamma_{SV} 2\pi r^2 (\cos\psi_0 - \cos\psi) + \gamma_{LS} 2\pi r^2 (1 + \cos\psi) \end{aligned} \tag{3.6}$$

Young's equation gives [21]

$$\gamma_{SV} = \gamma_{LS} + \gamma_{LV} \cos\theta_Y \tag{3.7}$$

In the above equations,

γ_{ij} = interfacial tension between interface ij (solid, liquid and vapour),

S_{ij} = interfacial area of interface ij (solid, liquid and vapour),

θ_Y = water contact angle on a flat surface (Young's contact angle).

The energy barrier for a single cavity, denoted as the free energy difference between the Cassie state (ψ=ψ_0) and maximum energy (ψ=θ_Y), is calculated as

$$\begin{aligned} \Delta E &= E_{(\psi=\theta_Y)} - E_{(\psi=\psi_0)} \\ &= \gamma_{LV} \pi r^2 (\sin^2\theta_Y - \sin^2\psi_0) + \gamma_{SV} 2\pi r^2 (\cos\psi_0 - \cos\theta_Y) + \gamma_{LS} 2\pi r^2 (\cos\theta_Y - \cos\psi_0) \\ &= \gamma_{LV} \pi r^2 (\sin^2\theta_Y - \sin^2\psi_0) + (\gamma_{SV} - \gamma_{LS}) 2\pi r^2 (\cos\psi_0 - \cos\theta_Y) \\ &= \gamma_{LV} \pi r^2 (\cos^2\psi_0 - \cos^2\theta_Y) + \gamma_{LV} \cos\theta_Y 2\pi r^2 (\cos\psi_0 - \cos\theta_Y) \\ &= \gamma_{LV} \pi r^2 (\cos^2\psi_0 + 2\cos\psi_0 \cos\theta_Y - 3\cos^2\theta_Y) \end{aligned} \tag{3.8}$$

The energy barrier per mm^2 of area is approximately equal to $\Delta E/\pi r^2 = \gamma_{LV}(\cos^2\psi_0 + 2\cos\psi_0\cos\theta_Y - 3\cos^2\theta_Y)$. When substituting $\psi_0 = 30°, \theta_Y = 98°, r = 800$ nm and applying $\gamma_{LV} = 72$ mN/m, this value is 72 nJ per mm^2. When compared with energy barriers of 1–10 nJ for perfluorinated micro-structures [20] and that of 61.5 nJ for bird feathers [22], it is noteworthy that external pores of diatom possess the water repellency as high as bird feathers. That explains why it is very hard for water to enter the external pores of diatom.

Additionally, if the bottom of the external pores of diatom is closed, the penetration of water into the pores will compress the air in the pore and increase the internal pressure dramatically, according to the ideal gas law $PV = nRT$. For example, if water fills half of the pore, the increase of internal pressure will be one atmosphere, which takes 10 meters of water depth to compensate for this pressure as per the Pasca's equation $P = \rho gh$.

3.4 Conclusions

Some native Australian plant leaves were selected to investigate the linkage between wettability and surface morphology. Both hydrophilic and hydrophobic leaves were found among the species studied. Four categories were summarized based on the distinct morphologies of these leaf surfaces. Hairy leaves were postulated to repel water through various mechanisms, such as elastic bundling, pyramid bundling, and layers of hair grids. Palm-tree-like hair leaves have contact angles greater than 130° and possess water repellency possibly because of the overlapping of palm-tree-like hairs, which work as a protection layer similar to an umbrella. The only grass-like plant studied here has distinguishable micro-ridges

(optical) and micro-ridges (SEM) on the surface, which lead to an anisotropic wetting property. These findings represent the initial attempt to uncover the special morphologies of certain native Australian plant leaves. In addition, the external pores of diatoms were modelled geometrically and a free energy calculation was carried out under the specific geometry. It was found the energy barrier required for water penetration in this model is comparable to that of bird feathers that are impressive natural waterproofed structures.

References

[1] C. Neinhuis and W. Barthlott. Characterization and distribution of water-repellent, self-cleaning plant surfaces. *Annals of Botany*, 79(6):667–677, 1997. 51, 52

[2] Lin Feng, Yanan Zhang, Jinming Xi, Ying Zhu, Nu Wang, Fan Xia, and Lei Jiang. Petal effect: A superhydrophobic state with high adhesive force. *Langmuir*, 24(8):4114–4119, 2008. 52

[3] W. Barthlott and C. Neinhuis. Purity of the sacred lotus, or escape from contamination in biological surfaces. *Planta*, 202:1–8, 1997. 52, 59

[4] Niranjan A. Malvadkar, Matthew J. Hancock, Koray Sekeroglu, Walter J. Dressick, and Melik C. Demirel. An engineered anisotropic nanofilm with unidirectional wetting properties. *Nature Materials*, 9(12):1023–1028, 2010. 52

[5] J. M. Benyus. *Biomimicry: Innovation Inspired by Nature*. William Morrow & Company Inc, New York, NY, USA, 1997. 52

[6] Alexander Otten and Stephan Herminghaus. How plants keep dry: A physicist's point of view. *Langmuir*, 20(6):2405–2408, 2004. 59, 60, 61

[7] Jianguo Fan and Yiping Zhao. Nanocarpet effect induced superhydrophobicity. *Langmuir*, 26(11):8245–8250, 2010. 61, 62

[8] A. B. D. Cassie and S. Baxter. Wettability of porous surfaces. *Transactions of the Faraday Society*, 40:546–551, 1944. 62

[9] Wilhelm Barthlott, Thomas Schimmel, Sabine Wiersch, Kerstin Koch, Martin Brede, Matthias Barczewski, Stefan Walheim, Aaron Weis, Anke Kaltenmaier, Alfred Leder, and Holger F. Bohn. The *Salvinia* paradox: Superhydrophobic surfaces with hydrophilic pins for air retention under water. *Advanced Materials*, 22:2325–2328, 2010. 65, 66

[10] Paul J. Molino, Samantha Childs, Maeve R. Eason Hubbard, Janet M. Carey, Mark A. Burgman, and Richard Wetherbee. Development of the primary bacterial microfouling layer on antifouling and fouling release coatings in temperate and tropical environments in Eastern Australia. *Biofouling*, 25 (2):149–162, 2009. 69

[11] L.D. Chambers, K.R. Stokes, F.C. Walsh, and R.J.K. Wood. Modern approaches to marine antifouling coatings. *Surface and Coatings Technology*, 201(6):3642–3652, 2006. 69

[12] Paul J. Molino and Richard Wetherbee. The biology of biofouling diatoms and their role in the development of microbial slimes. *Biofouling*, 24:365–379, 2008. 69

[13] Harihara S. Sundaram, Youngjin Cho, Michael D. Dimitriou, John A. Finlay, Gemma Cone, Sam Williams, Dale Handlin, Joseph Gatto, Maureen E. Callow, James A. Callow, Edward J. Kramer, and Christopher K. Ober. Fluorinated amphiphilic polymers and their blends for fouling-release applications: The benefits of a triblock copolymer surface. *ACS Applied Materials & Interfaces*, 3:3366–3374, 2011. 69

[14] Helmut Goesmann and Claus Feldmann. Nanoparticulate functional materials. *Angewandte Chemie International Edition*, 49:1362–1395, 2010. 70

[15] Colin Anderson, Mehmet Atlar, Maureen Callow, Maxim Candries, and RL Townsin. The development of foul-release coatings for seagoing vessels. In *Proceedings of the Institute of Marine Engineering, Science and Technology. Part B, Journal of marine design and operations*, number 4, pages 11–23, 2003. 70

[16] A. J. Scardino, E. Harvey, and R. De Nys. Testing attachment point theory: diatom attachment on microtextured polyimide biomimics. *Biofouling*, 22 (1):55–60, 2006. 70

[17] R. Holland, T. M. Dugdale, R. Wetherbee, A. B. Brennan, J. A. Finlay, J. A. Callow, and Maureen E. Callow. Adhesion and motility of fouling diatoms on a silicone elastomer. *Biofouling*, 20(6):323–329, 2004. 70

[18] Elisa Martinelli, Serena Agostini, Giancarlo Galli, Emo Chiellini, Antonella Glisenti, Michala E. Pettitt, Maureen E. Callow, James A. Callow, Katja Graf, and Frank W. Bartels. Nanostructured films of amphiphilic fluorinated

block copolymers for fouling release application. *Langmuir*, 24(22):13138–13147, 2008. 70

[19] Edward Bormashenko, Yelena Bormashenko, Gene Whyman, Roman Pogreb, and Oleg Stanevsky. Micrometrically scaled textured metallic hydrophobic interfaces validate the Cassie-Baxter wetting hypothesis. *Journal of Colloid and Interface Science*, 302(1):308–311, 2006. 70

[20] Laura Barbieri, Estelle Wagner, and Patrik Hoffmann. Water wetting transition parameters of perfluorinated substrates with periodically distributed flat-top microscale obstacles. *Langmuir*, 23(4):1723–1734, 2007. 72, 73

[21] Thomas Young. An essay on the cohesion of fluids. *Philosophical Transactions of the Royal Society of London*, 95:65–87, 1805. 72

[22] Edward Bormashenko, Oleg Gendelman, and Gene Whyman. Superhydrophobicity of lotus leaves versus birds wings: Different physical mechanisms leading to similar phenomena. *Langmuir*, 28(42):14992–14997, 2012. 73

Chapter 4

Hydrophobic Australian *Eucalyptus* Leaves

4.1 Introduction

Many biological surfaces, such as plant leaves, bird feathers and animal furs, exhibit strong water repellency in order to adapt to environmental conditions. A typical example is the adaxial surface of the lotus leaf *Nelumbo nucifera*, which remains completely dry while floating on water. The wetting characteristics of the lotus leaf include high contact angles and low contact angle hysteresis [1–4], attributed largely to a hierarchical surface structure. These properties have formed the basis of many surface-critical applications, for example self-cleaning [5–7], corrosion prevention [8], drag reduction [9] and fouling control [10]. Recently, high contact angle hysteresis was observed for certain rose petals exhibiting high contacts angles [11]. These petals contain relatively widely spaced micro-bumps of small peak-to-base heights. Consequently, a composite wetting scenario pre-

vails — that is, the Wenzel process [12] is dominant on the micro-structure level, allowing water to enter the asperities and therefore leading to a high contact area and high adhesion, and the Cassie mode [13], which rules on the nano-structure level, maintaining high water contact angles. Such unique wetting behaviour may lead to applications in mass and heat transport [14] or microfluidic devices [15].

The contact angle, commonly used to quantify the wettability of a solid surface, is a function of two independent variables: the surface energy of the solid controlled by its chemical composition and bonding states, and the surface roughness. Evidence has shown that the presence and three-dimensional (3D) geometry of surface patterns can markedly alter the wetting responses of a surface. For example, micro-structured features, in the form of pores and posts on a leaf surface, can increase water contact angles substantially. Recent studies reveal that nano-structured roughness can further enhance the water repellency and help maintain a robust composite wetting [11, 16–19]. Therefore, understanding the relationships between surface geometric parameters and wetting properties may help develop new types of surfaces with unexpected property combinations.

Eucalyptus, a dominant tree across temperate, arid and tropical ecosystems in Australia, is well adapted for coping with environmental extremes. However, the wetting properties of *Eucalyptus* have not been studied in detail, even though an investigation of surface leaf waxes was undertaken in 1970 of 315 *Eucalyptus* species for taxonomic purposes [20]. In this chapter, eight Australian native *Eucalyptus* species with a prominent waxy-white leaf form were studied in regard to their hydrophobicity and surface morphology. Different from Chapter 3, where selected species were categorized into four groups based on leaf surface micromorphology, these *Eucalyptus* species were compared here due to the same family

they belong to. SEM micro-graphs indicated that various surface morphologies were found on these leaves. Three species with papillae micro-morphology on the leaf surface, among these eight species, were investigated with a special focus on the link between the surface micro-structures and leaf surface hydrophobicity. To do so, physical models were constructed based on the dimensions of surface micro-structure features observed on these leaves. The contact angles, wetting robustness and critical pressures of these leaves were calculated and compared to the well established parameters for the leaf of lotus *Nelumbo nucifera*.

4.2 Experimental procedure

4.2.1 Sample preparation

Fresh leaves of eight *Eucalyptus* species, i.e., *E. woodwardii* (S#8), *E. pruinosa* (S#9), *E. pachyphylla* (S#18), *E. dolorosa* (S#20), *E. eudesmioides* (S#21), *E. oxymitra* (S#23), *E. lane - poolei* (S#25) and *E. gomphocephala* (S#26) were collected from actively growing specimens in the nursery at the State botanic garden, Kings Park in Perth, Western Australia.

Sample preparation procedures for optical observation and contact angle measurements were detailed in Chapter 3.

4.2.2 Instrumentation

Experimental settings for an FTA1000 goniometer, a Moticam 2300 digital camera and Scanning Electron Microscopy (SEM) were elaborated in Chapter 3.

4.3 Results and discussion

4.3.1 Surface morphology

A total of eight Australian native *Eucalyptus* were examined in respect of water contact angle (WCA) values and surface morphologies of their leaves. These juvenile leaves have glaucous surfaces that is presumably covered by wax; water droplets form spheres when deposited on the leaf surfaces (Fig. 4.1). Moderate hydrophobicity with WCA values in the range 120°–150° was observed on all selected species (Table 4.1).

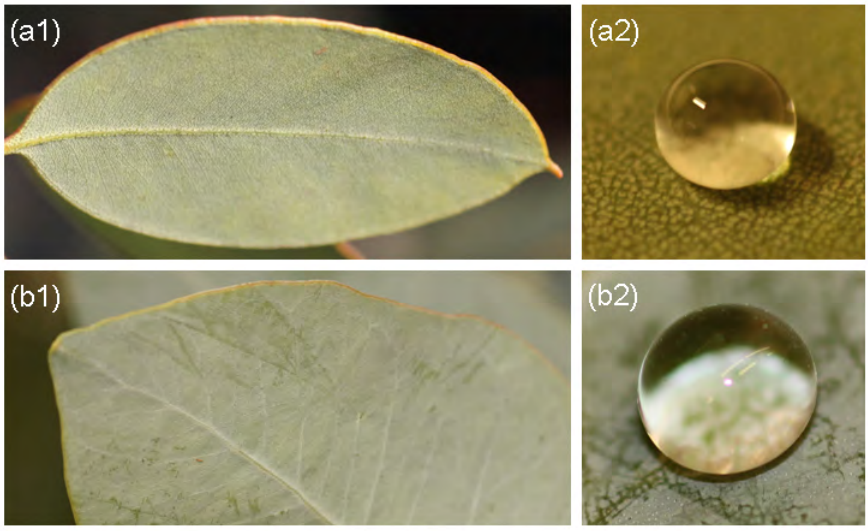

Figure 4.1: Water droplets on glaucous leaves of: (a) *Eucalyptus lane — poolei* (S#25) and (b) *Eucalyptus pruinosa* (S#9).

SEM images reveal various surface micro-structures on the selected *Eucalyptus* species: micro-bumps (Fig. 4.2b), random micro-ridges (Fig. 4.2c) and more orderly micro-ridges whose unevenness in height resembles micro-bumps at larger scale magnification (Fig. 4.2a). Upon these micro-structures is a layer of nano-

Table 4.1: WCA values of selected *Eucalyptus* species.

Sample No.	Sample names	WCA (°)
S#8	*E. woodwardii*	142.6 ± 1.7
S#9	*E. pruinosa*	129.2 ± 2.2
S#18	*E. pachyphylla*	146.3 ± 2.5
S#20	*E. dolorosa*	151.4 ± 1.2
S#21	*E. eudesmioides*	128.6 ± 3.5
S#23	*E. oxymitra*	124.0 ± 2.8
S#25	*E. lane - poolei*	131.1 ± 1.6
S#26	*E. gomphocephala*	125.3 ± 2.4

scale wax in different dimensions and forms. On sample S#9, nanotube wax lays parallel to the leaf surface in the same directions as the micro-ridges. On sample S#21, upright plate wax covers the micro-bumps, the stomata and the cuticle. On sample S#25, relatively small plate wax and irregularly shaped particles are distributed sparsely on top of the micro-ridges. Multiple length scales of roughness, namely micro-structure and nano-structure, are found on these *Eucalyptus* species and indicate its necessity in this strategy for achieving hydrophobicity.

Three *Eucalyptus* species with distinguishable micro-bump structures, S#8, S#18 and S#20, were studied in detail here. Special wetting features, namely high contact angles and strong water adhesion, were evident on the leaves of all three species. This is similar to the findings on the petals of Rosa, *cv.* Bairage [11] and in sharp contrast with the wetting condition of the lotus leaf, which is characterized by high contact angles but negligible water retention.

The water contact angles of the study species (Table 4.1), when compared to that of lotus leaves ($160.4 \pm 0.7°$ [21]), can be considered strongly hydrophobic. Given that lotus is an emergent aquatic plant and the study species of *Eucalyptus*

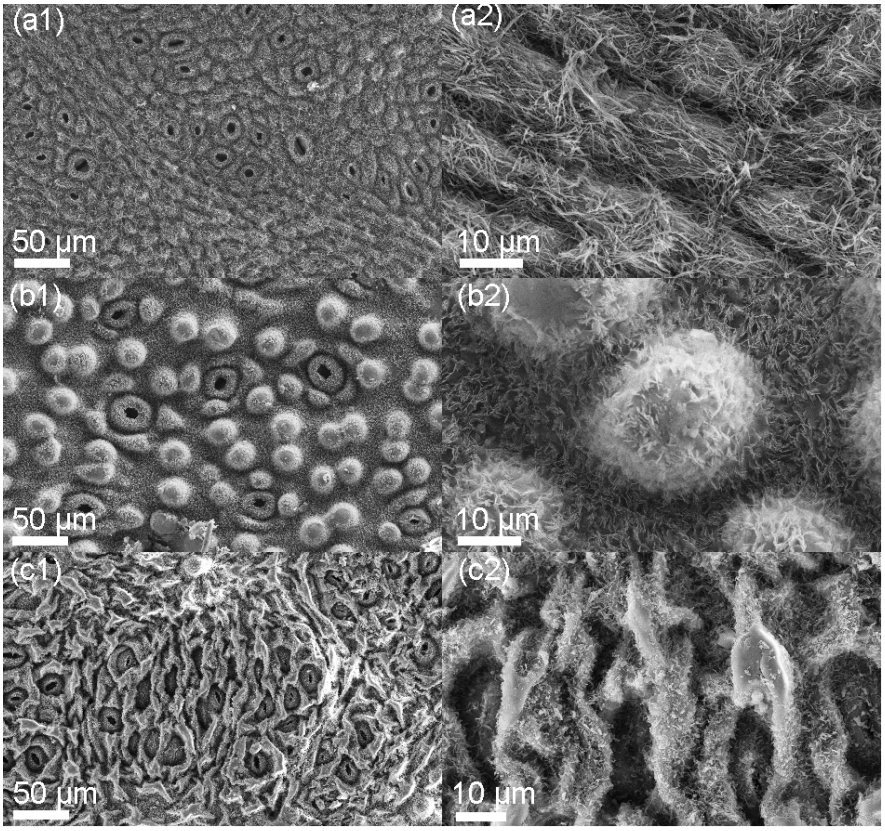

Figure 4.2: SEM images of three typical leaf surfaces: (a) *Eucalyptus pruinosa* (S#9), (b) *Eucalyptus eudesmioides* (S#21) and (c) *Eucalyptus lane — poolei* (S#25).

live in drier environments, it is surprising that these *Eucalyptus* spp. present such high levels of leaf hydrophobicity. Conversely, strong adhesion was observed on all three *Eucalyptus* species, before wax removal, between the water droplet and the leaf surface, with the droplet adhering firmly to the surface when it was gradually tilted from 0° to 180° (Fig. 4.4). This adhesion may be due to a large contact area between the water and the leaf surface. Water retention on fresh leaves is believed to help maintain surface hydration following a rainfall or evening dew event by providing the leaf with an additional source of moisture particularly as

most *Eucalyptus* endure periods of low rainfall.

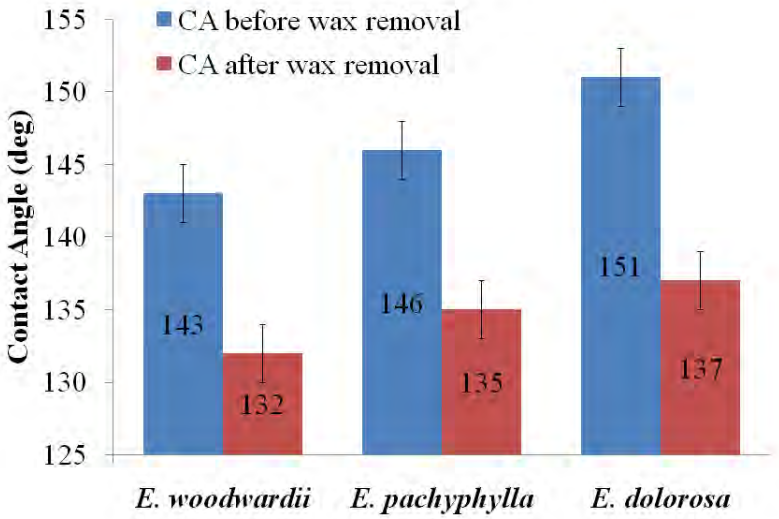

Figure 4.3: Experimental water contact angles of *Eucalyptus* leaves before and after wax removal.

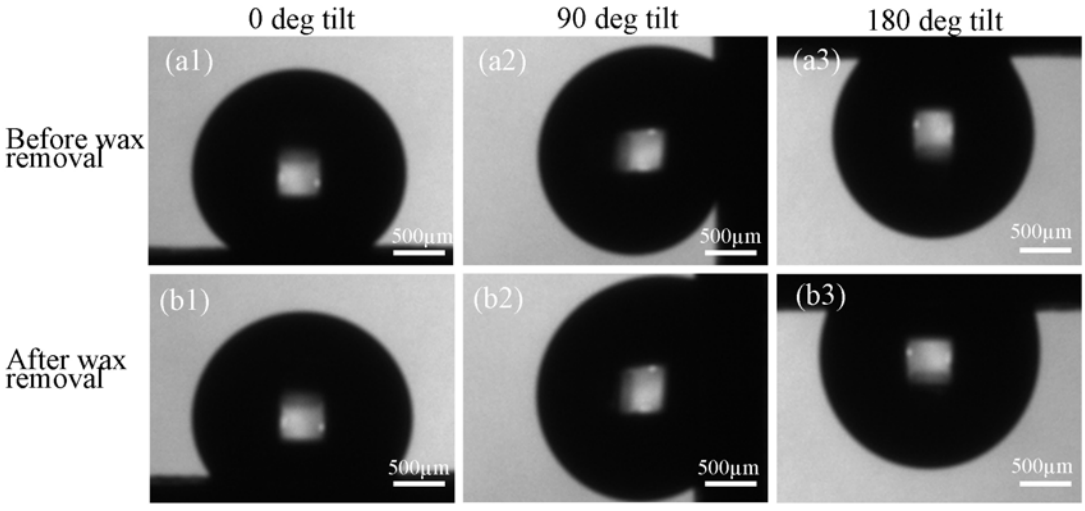

Figure 4.4: Water droplets on *E. pachyphylla* leaves before (a) and after (b) wax removal at different surface tilt angles of 0°, 90°, 180° (scale bars = 500 μm).

The surface morphologies of *Eucalyptus* leaves are shown in Fig. 4.5. Gener-

ally, the entire surfaces of these leaves are covered by fine nanometre scale wax at different forms and microscopic papillae and stomata, forming at least two length scales of roughness. On the micrometer level, hemisphere-like papillae arranged in a quasi-hexagonal pattern appear uniformly on the leaf surface of all three *Eucalyptus* species. Different wax morphologies, however, can be identified at the nanometre level. Needle-like wax particles of approximately 5 μm in length and 200 nm in diameter are aggregated on the leaf surface of *E. woodwardii* (Fig. 4.5a), while string-like wax covers the papillae of *E. pachyphylla* (Fig. 4.5b) and flake-like wax is found on *E. dolorosa* (Fig. 4.5c). These multi-scale structures have some morphological similarity to that of lotus [21]. However, a major difference is that, for lotus leaves, the wax forms fine, nanometre-length short hairs positioned upright to the surface, while on these *Eucalyptus* leaves, wax features have relatively large dimensions laying loosely over the surface.

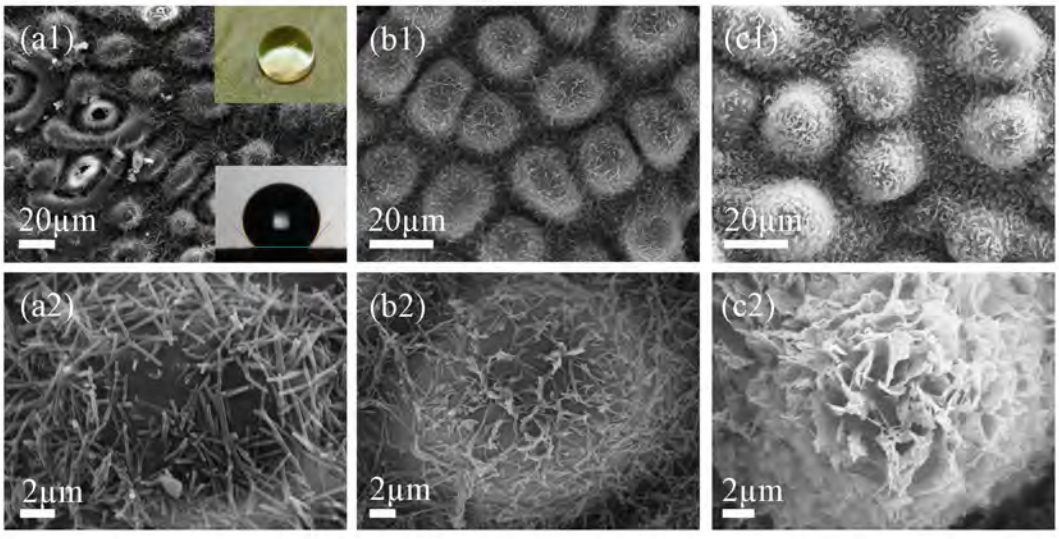

Figure 4.5: SEM images of three *Eucalyptus* leaves at different magnifications: (a) *Eucalyptus woodwardii* with optical images of water droplets shown in the inset, (b) *Eucalyptus pachyphylla*, and (c) *Eucalyptus dolorosa*.

In order to resolve the role that the wax structure plays in the observed wetting properties, water contact angles on these *Eucalyptus* leaves were measured and compared before and after wax removal (Fig. 4.3). For leaves free of wax, an average contact angle drop of $12 \pm 1.7^{\circ}$ was observed, which suggests that the contribution to the contact angles from the wax is relatively minor and that the leaf micro-structures impart an inherent surface hydrophobicity. Note, in Fig. 4.4 all images were taken with the same droplet volume, magnification, and light settings, the contact area between the water and the leaf surface became larger after wax was removed while maintaining a considerable hydrophobicity.

The surface micro-structures of these *Eucalyptus* leaves appear to play a key role in determining water contact angles, as high contact angles are still maintained even after wax is removed. However, wax structures, on the nanometre scale, enhance the wetting robustness. For example, synthetic hierarchical surfaces with varying micro-structure pitch values and wax densities (which are made of the nano-structures) have been fabricated [11]. On these artificial surfaces, the water contact angle did not change substantially on 23 μm pitch micro-structures across differing wax densities. However, there was a drop in the contact angle on a 105 μm pitch micro-structure when less wax was deposited. Based on the above observation and analysis, wetting states of both the *Eucalyptus* and the lotus *Nelumbo nucifera* leaves may be modelled by using their surface micro-structural parameters as inputs. The surface morphology of these three *Eucalyptus* leaves (S#8, 18, 20) can be considered as multiple hemispheres sitting on a flat plane (Fig. 4.6a). Similarly, for lotus [21], the leaf surface can be visualized as a plane containing many cylinders, each with a hemisphere cap (Fig. 4.6b). In both models, the radius of the hemisphere is denoted as r_0, the height of the cylinder

as h_0, and the edge-to-edge distance between two neighbouring micro-structures as $2d_0$. When h_0 equals zero, two models become the same.

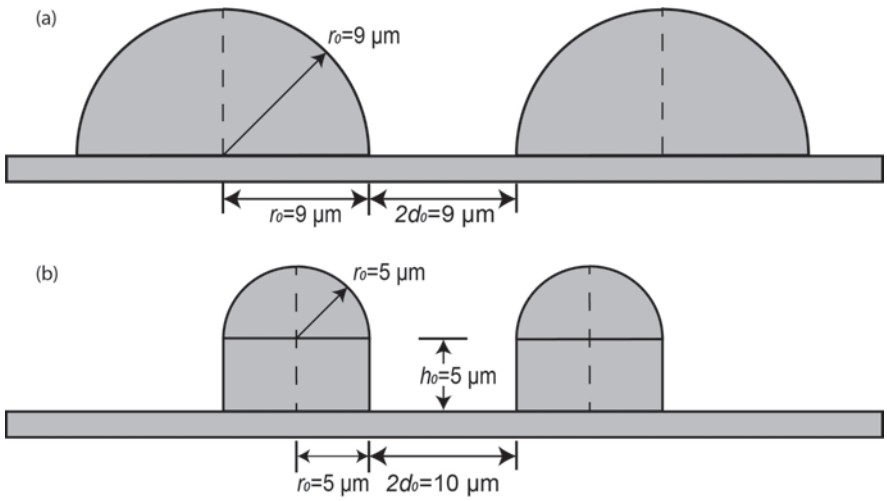

Figure 4.6: Generalized physical models of microscopic surface features of: (a) *Eucalyptus* leaf with parameters adopted from *Eucalyptus pachyphylla* and (b) lotus leaf *Nelumbo nucifera*.

The surface micro-structural parameters of both lotus and three *Eucalyptus* leaves, such as r_0, h_0 and $2d_0$, were measured from SEM images and summarized in Table 4.2. It is understood that the arrangement of the micro-structured features on the leaf surface may affect the surface roughness, which in turn influences the contact angle. Two most common arrangements of the microscopic hemispheres, namely hexagonal (Fig. 4.7a) and square patterns (Fig. 4.7b) are thus considered here when calculating wetting properties. However, negligible difference (for example, <1% in contact angle) was observed from these two patterns in this study. Therefore, only data from the hexagonal pattern is reported here.

Table 4.2: Geometric parameters of micro-structures measured on the leaf surfaces of lotus *Nelumbo nucifera* and three *Eucalyptus* species.

Sample No.	Sample names	Radius, r_0 (μm)	Height, h_0 (μm)	Distance, $2d$ (μm)
-	Lotus	5 ± 0.5	5 ± 0.5	10 ± 1.2
S#8	*E. woodwardii*	8 ± 0.8	0	14 ± 2.8
S#18	*E. pachyphylla*	9 ± 0.6	0	9 ± 2.8
S#20	*E. dolorosa*	10 ± 1.0	0	16 ± 5.4

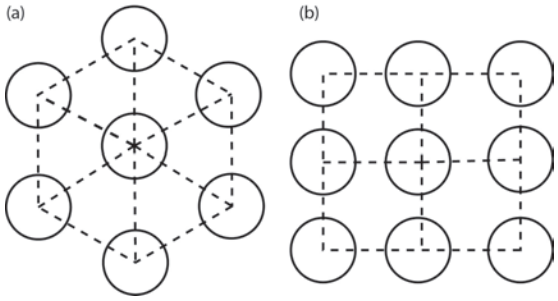

Figure 4.7: Two common patterns of micro-structures: (a) hexagonal and (b) square.

4.3.2 Contact angle calculations

In the Wenzel state wetting, water fills in the asperities of the micro-structure and maintains the maximum contact with the surface. As such, the contact angle is expressed as [12]

$$cos\theta_W = r \cos\theta_Y \tag{4.1}$$

where θ_W and θ_Y are the Wenzel and Young contact angles, respectively. The roughness factor, r, is defined as A_{SL}/A_F, where A_{SL} is the actual solid-liquid contact area and A_F is the projected area of the actual solid-liquid contact on the horizontal surface plane. The roughness factors for the hexagonal pattern can be calculated by the following equation: $r = 1 + \frac{\pi r^2 + 2\pi r h_0}{0.866 \cdot (2r+2d)^2}$.

Table 4.3: Calculated contact angles using the Wenzel equation on fresh leaves of lotus and three *Eucalyptus* species.

Sample No.	Sample names	Experimental WCA (°)	Calculated WCA (°)
-	Lotus	160.4 ± 0.7 [21]	114.0
S#8	*E. woodwardii*	142.6 ± 1.7	107.7
S#18	*E. pachyphylla*	146.3 ± 2.5	110.2
S#20	*E. dolorosa*	151.4 ± 1.2	107.7

Table 4.3 summarizes the experimental and calculated contact angles using Wenzel equation on fresh lotus and three *Eucalyptus* species, respectively. In these calculations, 104° was adopted as the water contact angle on a flat surface covered by wax [22]. It can be seen that calculated contact angles for lotus and *Eucalyptus* leaves are much lower than the experimental ones. Therefore, the wetting behaviour of these leaves cannot be explained using the Wenzel model.

Alternatively, the Cassie model, characterized by the presence of air pockets between water and the leaf surface, can be used to calculate the contact angles as [13]

$$cos\theta_{CB} = r_f f \cos\theta_Y + f - 1 \tag{4.2}$$

where θ_{CB} and θ_Y are the Cassie-Baxter and Young contact angles, respectively, r_f is the wetted roughness ratio of the surface area wetted by the liquid and f is the fraction of solid surface area contacting the liquid. The height of cap that is wetted by the liquid is introduced based on the models and denoted as h_{cap}. The calculations can be stated as

$$r_f = \frac{2\pi r h_{cap}}{\pi[r^2 - (r - h_{cap})^2]} \tag{4.3}$$

and

$$f = \frac{2\pi r h_{cap}}{2\pi r^2 + 2\pi r h + \sqrt{3}(2d)^2/2 - \pi r^2} \tag{4.4}$$

4.3.3 Analysis of wetting robustness

The combination of a spacing parameter [13] and a wetting robustness parameter [23] has also been considered in assessing the ability of a specific surface micro-structure to maintain its composite wetting. Based on the two physical models presented in Fig. 4.6, a spacing parameter was developed here following the Cassie-Baxter equation [13]. Across two structures in Fig. 4.6, the smallest building block will be four-sided and a hexagonal pattern, it will be a rhombus formed by four neighbouring micro-structures (Fig. 4.7a). Within the rhombus, the solid-liquid contact area is equivalent to a complete cap.

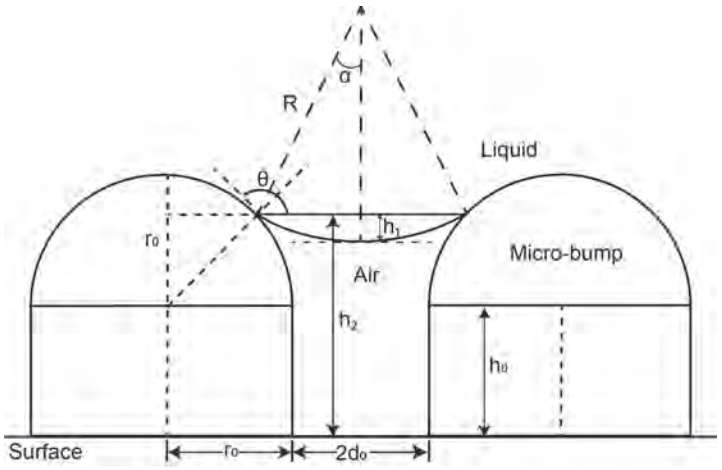

Figure 4.8: A side view schematic plot of geometric parameters defined for calculating the robustness parameter. The triple line plane is formed by creating a plane parallel to the bottom surface with a distance h_2, based on the line connecting the two points where the meniscus meets the top of micro-bumps.

The height of the cap wetted by water, in Fig. 4.8, is $r_0[1 - \sin(\theta_A - 90°)] =$

$r_0(1+\cos\theta_A)$. The area of the cap wetted by water is equal to $2\pi(r_0)^2(1+\cos\theta_A)$. The area of the rhombus parallel to the rough surface can be expressed as $\frac{\sqrt{3}}{2}(2r_0+2d_0)^2$. Therefore, f_1, defined as the solid-liquid contact fraction over the projected area, can be derived as $\frac{2\pi(r_0)^2(1+\cos\theta_A)}{\frac{\sqrt{3}}{2}(2r_0+2d_0)^2}$. The liquid-air contact area in the rhombus is equal to the difference between the projected rhombus area and the area of a circle with the radius of $r_0\cos(\theta_A - 90^\circ) = r_0\sin\theta_A$. Accordingly, f_2, defined as the liquid-air contact fraction over the projected area, can be formulated as $1 - \frac{\pi(r_0)^2\sin^2\theta_A}{\frac{\sqrt{3}}{2}(2r_0+2d_0)^2}$. When substituting these two area fractions, the Cassie-Baxter equation becomes

$$cos\theta_D = \frac{2\pi(r_0)^2(1+\cos\theta_A)}{\frac{\sqrt{3}}{2}(2r_0+2d_0)^2}\cos\theta_A - [1 - \frac{\pi(r_0)^2\sin^2\theta_A}{\frac{\sqrt{3}}{2}(2r_0+2d_0)^2}] = \frac{\pi(r_0)^2(1+\cos\theta_A)^2}{\frac{\sqrt{3}}{2}(2r_0+2d_0)^2} - 1 \tag{4.5}$$

Note the spacing parameter can be defined as $D^* = (\frac{r_0+d_0}{r_0})^2$, the equation reduces to

$$\cos\theta_D = \frac{\pi(1+\cos\theta_A)^2}{2\sqrt{3}D^*} - 1 \tag{4.6}$$

A large value of D^* apparently leads to a high contact angle, which means that large d_0/r_0 values for micro-structures are preferred for hydrophobicity. However, an indefinite value of d_0/r_0, which renders the surface flat, would not result in a 180° contact angle. Therefore, a critical d_0/r_0 value should exist, giving the highest contact angle while maintaining a composite wetting state.

The robustness parameter H^* [23], defined as h_2/h_1 (Fig. 4.8), describes how likely it is for liquid to enter the asperities on a rough surface due to capillary effect. A larger value of H^* renders a wetting regime transition, from composite to wetted, more difficult and thus maintains a composite wetting state. The

distance between the triple line plane and the surface horizon, h_2, is equal to $h_0 + \sin(\theta - 90°) = h_0 - r_0 \cos\theta$. The sagging height, h_1, can be described as the distance between the triple line contact plane and the tangent plane of the liquid meniscus within the asperities.

The liquid meniscus in Fig. 4.8, resulting from capillary pressure in a narrow empty tube (note $2d_0 \approx 15$ μm), can be conjectured as being a portion of a liquid sphere surface with a radius R. Under this condition, the pressure difference across the liquid meniscus can be described by the Young-Laplace equation as $\Delta p = \frac{2\gamma_{lv}}{R}$, where Δp is the pressure difference, γ_{lv} is the liquid-vapour surface tension and R is the radius of the liquid sphere. The radius R approximates to the capillary length λ_c, when the liquid meniscus is at equilibrium with the absence of external pressure and is subjected to both gravitational acceleration and surface tension. In the geometry, $h_1 = R(1-\cos\alpha)$ and $\sin\alpha = (d_0 + r_0 - r_0\sin\theta)/R$. As R is much larger than d_0 and r_0, $\sin\alpha \approx \frac{d}{R} \approx \frac{d}{\lambda_c}$ and $\sin\alpha \approx \alpha$. Then h_1 can be derived as $h_1 \approx \lambda_c(1-\sqrt{1-\sin^2\alpha}) \approx \lambda_c(1-\sqrt{1-(\frac{d}{\lambda_c})^2}) \approx \lambda_c\{1-[1-(\frac{d}{\lambda_c})^2/2]\} = \frac{d^2}{2\lambda_c}$. Therefore, the robustness parameter can be expressed with respect to the two physical models (Fig. 4.6) as

$$H^* = \frac{h_2}{h_1} \approx \frac{h_0 - r\cos\theta}{\frac{d^2}{2\lambda_c}} = \frac{2\lambda_c(h_0 - r\cos\theta)}{d^2} \tag{4.7}$$

A large H^* value is preferred for maintaining a stable composite wetting, as a large barrier must be overcome before liquid can enter the asperities and wet the bottom of the surface. Based on eq 4.7, the combination of a large cylinder height h_0, a large hemisphere radius r_0 and a small micro-structure edge-to-edge distance d_0 will result in a large H^*. The distance d_0 is more influential than the other

variables in the equation when determining the H^* value. As D^* controls the contact angle and H* determines the wetting robustness, a combination of large values of D^* and H^* ensures a robust composite hydrophobicity. The calculated values of the spacing parameter D^* and the robustness parameter H^* for lotus and three *Eucalyptus* leaves are listed in Table 4.4.

Table 4.4: Calculated design parameters for lotus and three *Eucalyptus* species.

Sample No.	Sample names	$D^* = (\frac{r_0+d_0}{r_0})^2$	$H^* = \frac{2\lambda_c(h_0-r_0\cos\theta)}{(d_0)^2}$
-	Lotus	4.0	1339
S#8	*E. woodwardii*	3.5	211
S#18	*E. pachyphylla*	2.2	576
S#20	*E. dolorosa*	3.2	202

Lotus has achieved a larger D^* value and a much larger H^* value than all three *Eucalyptus* species. These values contribute to observed high contact angles and small roll-off angles on lotus leaves, and thus negligible contact between water and the leaf surface. The small H^* values found on *Eucalyptus* species could explain the high adhesion between water and the leaf surface, because water penetrates into the micro-structures and forms a large solid-liquid contact area that leads to sufficient adhesion to counteract the gravitational pull of a water droplet.

These geometric parameters, r_0, d_0 and h_0, can be adjusted to achieve certain D^* and H^* values for specific wetting applications. For superhydrophobic wetting such as lotus leaves, the relative value of d_0 may be tailored to achieve a high contact angle and a small contact area simultaneously. For applications where high adhesion is favoured such as in micro-volume liquid transport, d_0 can be manipulated towards a higher value to achieve relatively large D^* and H^*. Eq 4.7 suggests that a large value of h_0 would result in a large H^* without affecting

the value of D^*. Nano-nails, having a relatively high h_0 value compared to r_0, were reported to give a large D^* of 10–100 and a large H^* of 100–100,000 for an octane droplet [23]. However, h_0 cannot be indefinitely large compared to r_0. A typical example is a micro-scale hair pattern on the surface, which tends to lose its structural integrity under external loading. Therefore, other structural parameters, such as a mechanical integrity parameter, should also be developed and integrated with these design parameters to provide a more comprehensive evaluation of surface wetting.

4.3.4 Analysis of surface free energy

When a water droplet is gently deposited on a surface, based on the surface energy and roughness of the surface, one of the two classical wetting regimes can exist. In the homogeneous Wenzel wetting, water fills in the asperities of the micro-structure and maintains maximum contact with the surface. Alternatively, the heterogeneous Cassie model, characterized by the presence of air pockets between water and the leaf surface, can be used to calculate the contact angles.

For this three-phase system, different surface energies exist for specific wetting scenarios. There are, therefore, energy barriers between various wetting states. A principle of energy minimization is generally applied to determine the final wetting state. That is, the liquid will wet the rough surface to the extent that the overall surface energy of the system is minimized. A prerequisite for taking the final state of minimum energy is that the system can overcome the energy barriers lying between different conditions in a certain environment, given that wetting is a continuous physical process. Thus it is possible for the system to

reach equilibrium before the surface energy is minimized due to insurmountable energy barriers presented without any external disturbance. In order to analyse the possibility of transition between different wetting states, it is necessary to consider the corresponding Gibbs free energy analysis. The Gibbs free energy of a droplet on a surface can be described as [24, 25]

$$G = \gamma_{LV} S_{LV} + \gamma_{SV} S_{SV} + \gamma_{LS} S_{LS} \tag{4.8}$$

where γ_{ij} is the surface energy between the interface ij (solid, liquid and vapour), and S_{ij} is the contact area of the interface ij (solid, liquid and vapour).

Before these interfacial areas can be substituted by mathematical expressions, certain assumptions and reasonable approximations are required based on actuality: (a) The influence of gravity can be neglected, as the radius of a water droplet used here (3 μL, $\sim$1.0 mm) is usually less than the capillary length ($\sim$2.7 mm). Thus the droplet can be deemed to be spherical. (b) The radius of a water droplet is significantly larger than the surface roughness, and the radius of the liquid-vapour interface meniscus, between surface relief, can be approximated to the radius of the water droplet. Consequently, the liquid volume of entering the asperities of the micro-structures can also be neglected, and the liquid-vapour interface meniscus can be taken as planar, parallel to the surface horizontal plane. (c) The base of the spherical droplet can be approximated as the projection of the liquid-solid contact on the surface plane. (d) The contact line tension and potential energy are negligible as their contributions to the total surface energy are insignificant.

When relating to the droplet volume V and contact angle θ, the radius of the

droplet R can be expressed as [24]

$$R = (\frac{3V}{\pi})^{\frac{1}{3}}(2 - 3\cos\theta + \cos^3\theta)^{-\frac{1}{3}} \tag{4.9}$$

In a composite wetting state, the interfacial areas are calculated using r_f and f, the parameters defining the Cassie relationship. S_{LV} consists of two parts: the external spherical cap of the droplet and the liquid-vapour contact under the droplet.

$$S_{LV} = 2\pi R^2(1 - \cos\theta) + \pi R^2 \sin^2\theta(1 - f) \tag{4.10}$$

S_{LS} only contains the liquid-solid contact area under the droplet.

$$S_{LS} = \pi R^2 \sin^2\theta f r_f \tag{4.11}$$

S_{SV} also consists of two parts: the solid-vapour contact under and outside the droplet, respectively. $S_{SV-total}$ is introduced here as the total solid-vapour contact area before the droplet deposition. For a specific surface, $S_{SV-total}$ is constant.

$$S_{SV} = (S_{SV-total} - \pi R^2 \sin^2\theta r) + \pi R^2 \sin^2\theta(r - f r_f) \tag{4.12}$$

The Gibbs energy of a composite wetting system can be described by inserting eqs 4.9, 4.10, 4.11 and 4.12 into eq 4.8

$$\begin{aligned} G_{composite} = \gamma_{SV} S_{SV-total} + \gamma_{LV}(3V)^{\frac{2}{3}}\pi^{\frac{1}{3}}[F(\theta)]^{-\frac{2}{3}} \cdot \\ [2 - 2\cos\theta - \sin^2\theta \cdot F(f)] \end{aligned} \tag{4.13}$$

with

$$F(\theta) = 2 - 3\cos\theta + \cos^3\theta \tag{4.14}$$

and

$$F(f) = r_f f \cos\theta_Y + f - 1 \tag{4.15}$$

For a droplet with a volume V and a well-defined solid surface, the surface energy of the system changes with the contact angle θ and its specific wetting condition (in which these two parameters r_f and f can be determined). The surface roughness ratio, r, does not affect the value of $G_{composite}$ due to its absence in eq 4.13. However, eq 4.13 is a universal equation that remains valid for both composite and wetted regimes. Similar to the conversion between Wenzel and Cassie relations, the function $F(f) = r_f f \cos\theta_Y + f - 1$ for a composite regime can be simplified to $F(f) = r\cos\theta_Y$ for a wetted regime. Thus, the Gibbs energy for a wetted case (where there is no air trapped under the droplet and thus no liquid-vapour and solid-vapour contact areas), can also be obtained with the corresponding $F(f)$ expression.

Suppose the wetting transition from a composite case to a wetted case begins with gradual penetration of liquid into the asperities. Let h be the penetration depth, r_0 be the micro-hemisphere base radius and d_0 be half of the edge-to-edge distance of the micro-hemispheres in a hexagonal arrangement. For convenience, h can be reasonably related to r_0 by $h = xr_0$, where $x \in (0, 1)$ given the model for *Eucalyptus spp.*, and d_0 can be approximated to r_0. The wetting parameters for a composite case can be expressed as

$$r_f = \frac{2r_0}{2r_0 - h} = \frac{2}{2 - x} \tag{4.16}$$

and

$$f = \frac{\pi[(r_0)^2 - (r_0 - h)^2]}{\frac{\sqrt{3}}{2}(2r_0 + 2d_0)^2} = \frac{\pi(2x - x^2)}{8\sqrt{3}} \tag{4.17}$$

and for a wetted regime

$$r = 1 + \frac{\pi(r_0)^2}{2\sqrt{3}(r_0 + d_0)^2} = 1 + \frac{\pi}{8\sqrt{3}} \tag{4.18}$$

The function $F(f)$ can be rewritten when substituting eqs 4.16 and 4.17

$$F(f) = F(x) = \frac{4\pi x \cos\theta_Y - (2 - x)(\pi + 2\sqrt{3})}{(2 - x)(\pi + 2\sqrt{3} + 2\pi x)} \tag{4.19}$$

It is assumed here that the transition between a composite state and a wetted state involves gradual liquid penetration into the rough micro-structures. For each depth of penetration, there is a specific contact angle for the droplet in order to achieve the minimum surface energy. At the thermodynamic equilibrium, the contact angle θ equals the Cassie contact angle θ_C and eq 4.13 can be used to calculate the Gibbs surface energy

$$G_{Cassie} = \gamma_{SV} S_{SV-total} + \gamma_{LV}(3V)^{\frac{2}{3}}\pi^{\frac{1}{3}}[F(\theta_C)])^{\frac{1}{3}} \tag{4.20}$$

with

$$F(\theta_C) = 2 - 3\cos\theta_C + \cos^3\theta_C \tag{4.21}$$

In eq 4.20, both the first part on the right side, $\gamma_{SV} S_{SV-total}$ and $\gamma_{LV}(3V)^{\frac{2}{3}}\pi^{\frac{1}{3}}$ are positive and constant, the actual value of G_{Cassie} can be compared through $F(\theta_C)$, given the exponent on $F(\theta_C)$ is 1/3. The relationship between the $F(\theta_C)$ values and the penetration depth x is shown in Fig. 4.9.

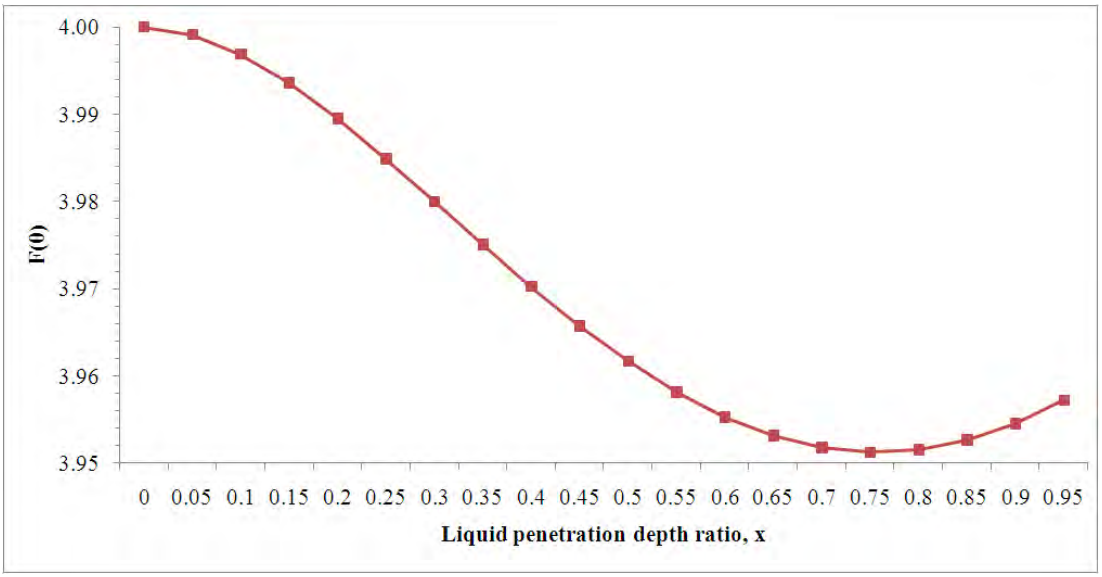

Figure 4.9: $F(\theta_C)$ at different penetration depths when $r_0 = d_0$.

The value of $F(\theta_C)$ decreases steadily as the penetration depth x increases from 0 to 0.75. At about 0.75, the minimum of $F(\theta_C)$ is obtained (3.951), which indicates the minimum surface energy for this specific geometry and composite wetting. After 0.75, $F(\theta_C)$ begins to increase slowly. This observation is similar to the case found on flat-top microscopic cylindrical pillars [25]. When x reaches unity, liquid touches the bottom and the wetting scenario shifts from composite to wetted, for which the $F(\theta_W)$ value can be calculated as 2.867 by employing eqs 4.1, 4.13 and 4.18. Subsequently, when a droplet is deposited gently on a surface characterized with microscopic hemispheres ($r_0 = d_0$), liquid under the droplet simultaneously enters the asperities and reaches a thermodynamic equilibrium at $x = 0.75$ to achieve the minimum surface energy for the composite regime (with local pinning and external energy input neglected). Since the wetted case possesses lower surface energy than the composite case, a transition occurs when

the vibration energy of the droplet or an external energy input can surpass the energy barrier, which can be calculated as the surface energy difference between the two states of $x \approx 0.75$ and $x \approx 1$. This method of energy barrier calculation agrees with a postulation that, on flat-top microscopic pillars, the energy barrier is the energy difference between the non-filling (Cassie) and complete-filling states [25].

The effect of edge-to-edge distance on the surface energy is studied by changing the value of d_0 based on a constant r_0, and the calculated $F(\theta_C)$ values are shown in Fig. 4.10. A lower minimum surface energy is obtained at a smaller depth for a smaller d_0. In addition, a larger energy barrier (marked as ΔG_1 in Fig. 4.10a), which acts as an indicator of hydrophobic stability, exists for the wetting transition for a smaller d_0. Therefore, a smaller d_0, such as $d_0 = 0$, is favoured to maintain a composite wetting state.

A portion of the $F(\theta_C)$ curve in Fig. 4.10a is expanded with an extension of the $F(\theta)$ values at wetted regimes. After a minimum surface energy is reached, $F(\theta)$ value (or accordingly the surface energy) increases gradually with further liquid penetration before complete wetting of the asperities. Although not shown in Fig. 4.10b, the $F(\theta)$ values at the x range of (0.95, 1) can be reasonably postulated as being slightly higher than the values acquired at $x = 0.95$. The surface energy difference between the composite state (with a minimum surface energy) and the wetted state, marked as ΔG_2 in Fig. 4.10b, can be considered as a transition potential or tendency. A larger energy difference, accompanied with a smaller barrier, reflects an easier composite-wetted transition for a larger d_0.

The energy barrier ΔG_1 and energy potential ΔG_2 for the wetting transition for different d_0 values are calculated using eq 4.20. The volume of the water

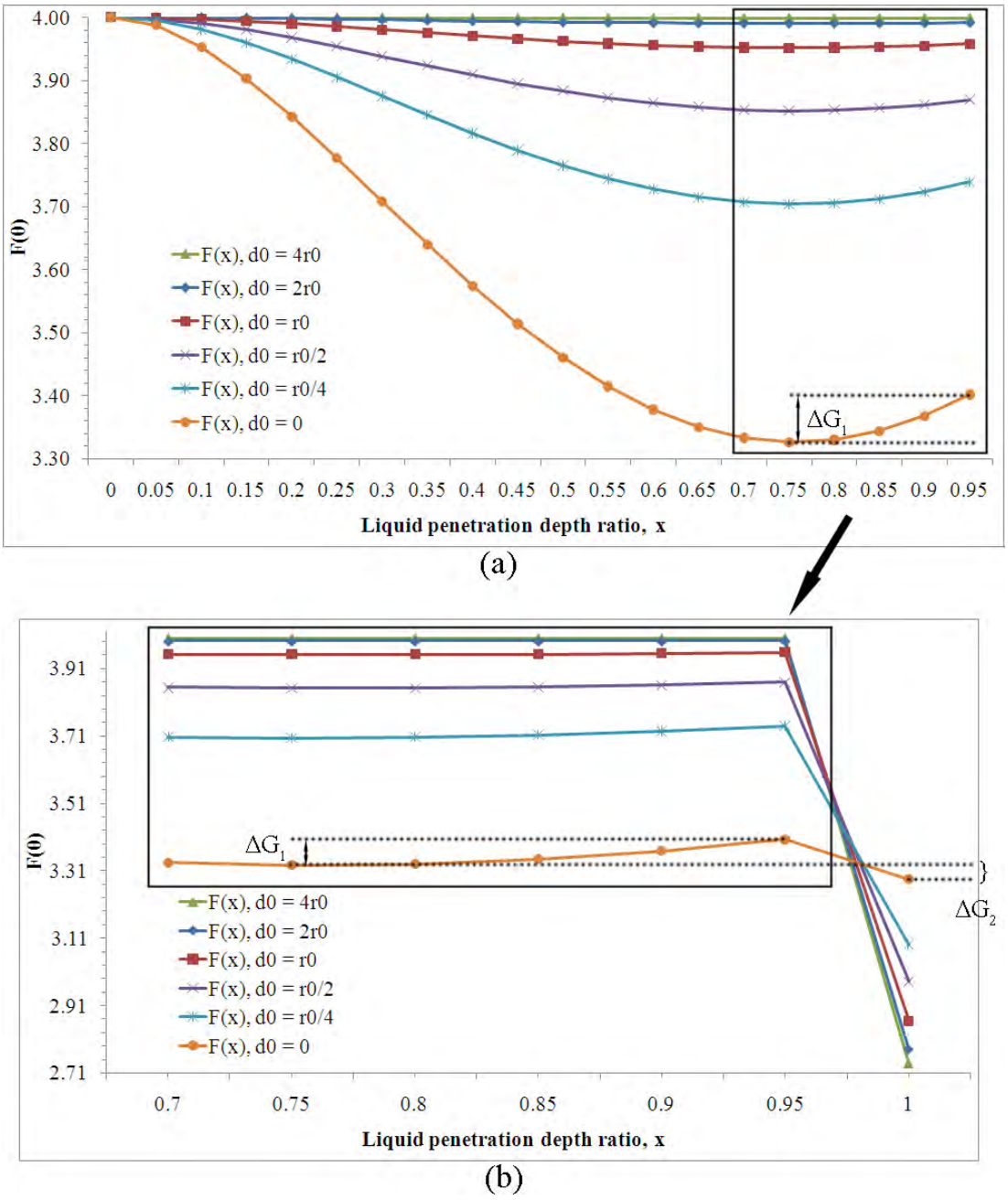

Figure 4.10: Influence of d_0 on $F(\theta_C)$ values: (a) $F(\theta_C)$ at different penetration depths with different d_0 values, (b) $F(\theta)$ at different penetration depths $x \in [0.75, 1]$). The $F(\theta)$ values at the x range of (0.95, 1) are omitted. When $x = 1$, $F(\theta) = F(\theta_W)$.

droplet is taken as 5 μL. The energy barrier is calculated as the difference between the lowest energy and the energy at $x = 0.99$, just before the wetting transition. The energy potential is calculated as the difference between the lowest energy at a composite state and the lowest energy at a wetted state. The results are shown in Table 4.5.

Table 4.5: Calculated energy barriers and energy potentials for different d_0.

d_0 value	ΔG_1 Energy barrier, nJ	ΔG_2 Energy potential, nJ
0	7.33	4.05
$r_0/4$	3.11	58.84
$r_0/2$	1.56	83.24
r_0	0.52	104.19
$2r_0$	0.065	116.83
$4r_0$	0.013	122.19

When d_0 decreases from r_0 to $r_0/4$, the energy barrier increases from 0.52 nJ to 3.11 nJ thus indicating enhanced hydrophobic stability or robustness. When $d_0 = 2r_0$, the energy barrier is close to zero and a droplet deposited gently on such a surface will spontaneously enter the roughness to the thermodynamically favoured wetted state.

In the model for lotus, the existence of h_0 leads to further extension of the penetration depth x at the range of $[1, 1 + h_0/r_0]$ with d_0 being approximated to r_0. The wetting parameters for a composite case, when the liquid level in the asperities is below the microscopic hemisphere base, can be expressed as

$$r_f = \frac{2\pi(r_0)^2 + 2\pi(r_0)^2(x-1)}{\pi(r_0)^2} = 2x \tag{4.22}$$

and

$$f = \frac{\pi(r_0)^2}{\frac{\sqrt{3}}{2}(2r_0 + 2d_0)^2} \tag{4.23}$$

and for a wetted condition, the roughness ratio is calculated as

$$r = 1 + \frac{\pi(r_0)^2 + 2\pi r_0 h_0}{\frac{\sqrt{3}}{2}(2r_0 + 2d_0)^2} \tag{4.24}$$

The $F(\theta_C)$ values with x at the range of [1, h_0) can be derived by combining eqs 4.14 and 4.15 for the free surface energy expressions, and eqs 4.22, 4.23, and 4.24 for the roughness factors. In Fig. 4.11, the curve is the same as the *Eucalyptus* model in the range of [0, 1). After further liquid penetration ($x \geq 1$), $F(\theta_C)$ keeps going up with a gradually decreasing slope. At the same range, the $F(\theta_W)$ value (corresponding to the wetted surface energy and marked in blue), increases with x at a constant slope of $\pi/(4\sqrt{3})$. At large depths of x (continued in Fig. 4.12), the $F(\theta_C)$ value reaches a maximum and then declines gradually even when $x = 10$. The $F(\theta_W)$ value increases with x and reaches a maximum at a much larger depth and then declines slowly. An intersection is found for these two cures at $x = 4.6$. After this point, the composite regime is more thermodynamically favoured than the wetted regime.

It should be noted that eq 4.20 can only be used when the thermodynamic equilibrium is reached and the Cassie relationship is applicable. After $x = 2.05$, the $F(f)$ value in eq 4.15 exceeds unity 1 and no solutions for the contact angle will be found to fulfil the equation of $F(f) = \cos\theta_C$. The same issue occurs for calculating the minimum surface energy for a wetted scenario using the Wenzel relation when x>7.4. After these two specific points, only the original eq 4.13 can be adopted for the overall surface energy calculation and the results stand

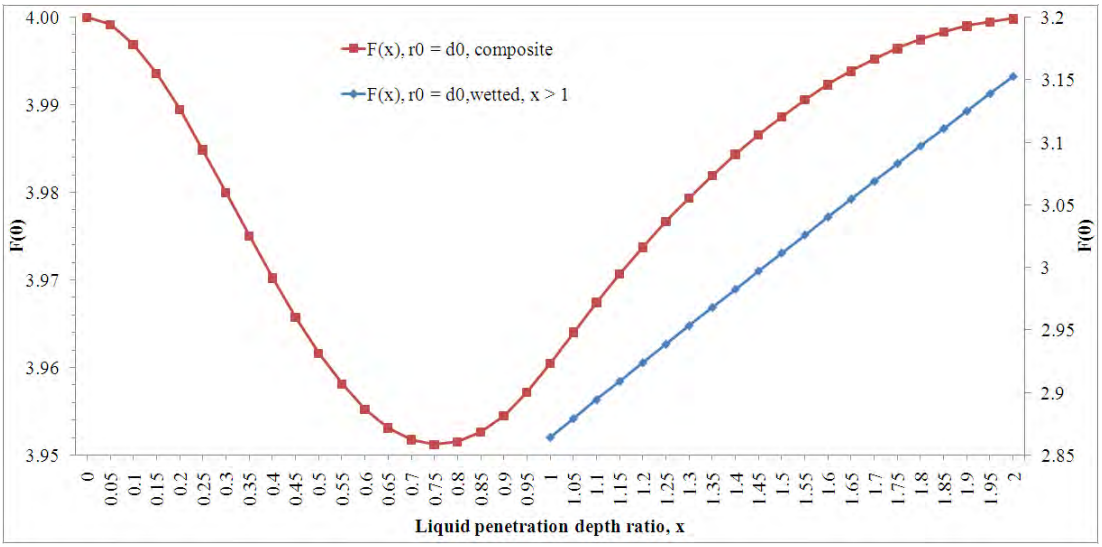

Figure 4.11: $F(\theta)$ values at different penetration depths of x: the composite state is marked by a red line (left vertical axis) and the wetted state is marked by a blue line (right vertical axis).

for situations when a thermodynamic equilibrium cannot be reached.

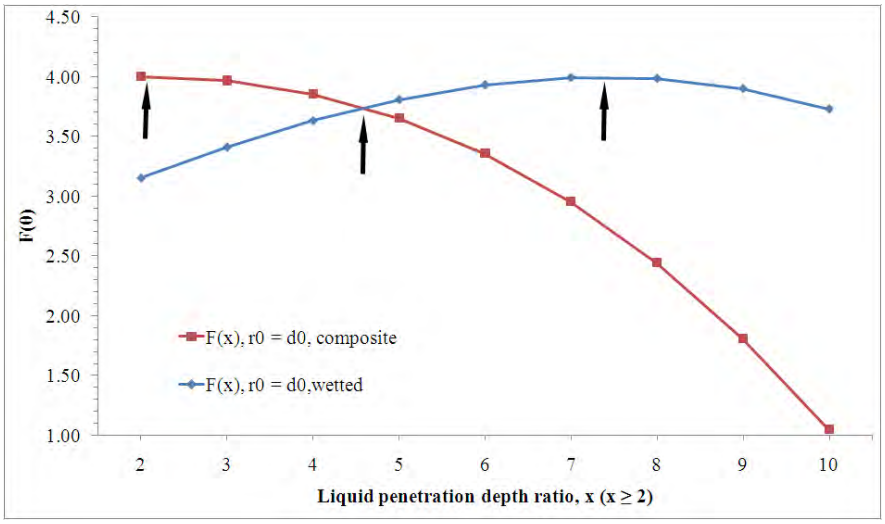

Figure 4.12: $F(\theta)$ values at large depths of x: composite state is marked by a red line and wetted state is marked by a blue line. Three black arrows denotes turning points on surface energy at $x = 2.05$, 4.6 and 7.4, respetively.

Table 4.6 reveals that greater energy barriers and lower energy potentials are obtained for greater h_0 values. The change of h_0 from 0 to r_0 significantly elevates the energy barrier from 0.86 nJ to 4.22 nJ and decreases the energy potential from 104.16 nJ to 74.28 nJ. When h_0>1, all wetting conditions with the penetration depth of x>$2r_0$ face the same maximum energy barrier (4.22 nJ) arising from this specific geometry. Before x reaches $7.4r_0$, after overcoming the energy barrier, a wetted regime with lower surface energy will be adopted by the system. However, neither a composite regime nor a wetted regime will be thermodynamically favoured with a liquid penetration deeper than $7.4r_0$. In this case, the droplet will adopt the composite state with a much smaller x at a thermodynamic equilibrium.

Table 4.6: Calculated energy barriers and energy potentials for different h_0.

h_0 value	ΔG_1 Energy barrier, nJ	ΔG_2 Energy potential, nJ
0	0.86	104.16
$r_0/4$	2.24	96.30
$r_0/2$	3.28	88.65
$3r_0/4$	3.88	81.37
r_0	4.22	74.28

The geometrical parameters presented in Fig. 4.6 can be adopted to compare the energy barriers and energy potentials of wetting on *Eucalyptus* and lotus leaves. For *Eucalyptus*, $r_0 = 2d_0 = 9$ μm and $h_0 = 0$, the energy barrier and energy potential are 1.56 nJ and 83.24 nJ, respectively. For lotus, $2r_0 = 2d_0 = 2h_0 = 10$ μm, these two values are 4.22 nJ and 74.28 nJ. The energy barrier for a wetting transition on a lotus leaf is nearly three times of that on a *Eucalyptus* leaf. The liquid-solid contact area, S_{LS}, is also compared between these two models,

as the contact area is expected to be strongly associated with the water-leaf adhesion. Given that the minimum surface energies at a composite state for the two models are obtained at a similar liquid penetration depth ratio ($x \approx 0.75$, Fig. 4.10 and 4.11), the radii of a 5 μL water droplet on the two models are calculated using eqs 4.9, 4.16 and 4.17. For *Eucalyptus* and lotus models, the radii are found to be 1.074 mm and 1.065 mm, respectively. After substituting eq 4.11 with the radii, the liquid-solid contact areas are acquired to be 0.908 mm^2 and 0.298 mm^2, respectively. Therefore, for a water droplet of 5 μL, the liquid-solid contact area on the *Eucalyptus spp.* is three times that on the lotus leaf. Even though several assumptions and approximations have been made for these calculations, the results can be used to describe qualitatively the stability of hydrophobicity and surface adhesion for two different kinds of leaves in the nature.

4.4 Conclusions

Physical models were constructed based on surface morphologies to gain a deeper understanding of the wetting mechanisms of *Eucalyptus* leaves in comparison to the lotus leaf, *Nelumbo nucifera*. Surface energy analysis on these two models shows the changes of minimum surface energy with stepwise liquid penetration into the asperities of the microscopic roughness. Lower minimum surface energy was found on a smaller edge-to-edge distance of the micro-structures in both models. The wetting transition from a composite state to a wetted state was quantitatively identified using energy barrier and energy potential as criteria. Greater cylindrical length below the microscopic hemisphere in the lotus model

increases the energy barrier for the wetting transition, which is beneficial for hydrophobic stability. The strong water adhesion on *Eucalyptus* leaves was also explained by a relatively larger liquid-solid contact area than for lotus. This study represents the first attempt to understand the unique wetting behaviour of *Eucalyptus* leaves using a hemisphere-top model. The results may guide the design of man-made surfaces with tailored wetting properties.

References

[1] Wei Chen, Alexander Y. Fadeev, Meng Che Hsieh, Didem Oner, Jeffrey Youngblood, and Thomas J. McCarthy. Ultrahydrophobic and ultralyophobic surfaces: Some comments and examples. *Langmuir*, 15(10):3395–3399, 1999. 79

[2] Didem Oner and Thomas J. McCarthy. Ultrahydrophobic surfaces. effects of topography length scales on wettability. *Langmuir*, 16(20):7777–7782, 2000.

[3] T. Onda, S. Shibuichi, N. Satoh, and K. Tsujii. Super-water-repellent fractal surfaces. *Langmuir*, 12(9):2125–2127, 1996.

[4] Michael Nosonovsky and Bharat Bhushan. Energy transitions in superhydrophobicity: low adhesion, easy flow and bouncing. *Journal of Physics: Condensed Matter*, 20:395005, 2008. 79

[5] C. Neinhuis and W. Barthlott. Characterization and distribution of water-repellent, self-cleaning plant surfaces. *Annals of Botany*, 79(6):667–677, 1997. 79

[6] Akira Nakajima, Kazuhito Hashimoto, Toshiya Watanabe, Kennichi Takai, Goro Yamauchi, and Akira Fujishima. Transparent superhydrophobic thin films with self-cleaning properties. *Langmuir*, 16(17):7044–7047, 2000.

[7] Bharat Bhushan, Yong Chae Jung, and Kerstin Koch. Self-cleaning efficiency of artificial superhydrophobic surfaces. *Langmuir*, 25(5):3240–3248, 2009. 79

[8] Tao Liu, Yansheng Yin, Shougang Chen, Xueting Chang, and Sha Cheng. Super-hydrophobic surfaces improve corrosion resistance of copper in seawater. *Electrochimica Acta*, 52(11):3709–3713, 2007. 79

[9] Glen McHale, Michael I. Newton, and Neil J. Shirtcliffe. Immersed superhydrophobic surfaces: Gas exchange, slip and drag reduction properties. *Soft Matter*, 6:714–719, 2010. 79

[10] A. J. Scardino, H. Zhang, D. J. Cookson, R. N. Lamb, and R. de Nys. The role of nano-roughness in antifouling. *Biofouling*, 25(8):757–767, 2009. 79

[11] Bharat Bhushan and Eun Kyu Her. Fabrication of superhydrophobic surfaces with high and low adhesion inspired from rose petal. *Langmuir*, 26(11):8207–8217, 2010. 79, 80, 83, 87

[12] Robert N. Wenzel. Resistance of solid surfaces to wetting by water. *Industrial & Engineering Chemistry*, 28(8):988–994, 1936. 80, 89

[13] A. B. D. Cassie and S. Baxter. Wettability of porous surfaces. *Transactions of the Faraday Society*, 40:546–551, 1944. 80, 90, 91

[14] Niranjan A. Malvadkar, Matthew J. Hancock, Koray Sekeroglu, Walter J. Dressick, and Melik C. Demirel. An engineered anisotropic nanofilm with

unidirectional wetting properties. *Nature Materials*, 9(12):1023–1028, 2010. 80

[15] R. Ledesma-Aguilar, R. Nistal, A. Hernandez-Machado, and I. Pagonabarraga. Controlled drop emission by wetting properties in driven liquid filaments. *Nature Materials*, 10(5):367–371, 2011. 80

[16] Yonghao Xiu, Lingbo Zhu, Dennis W. Hess, and C. P. Wong. Hierarchical silicon etched structures for controlled hydrophobicity/superhydrophobicity. *Nano Letters*, 7(11):3388–3393, 2007. 80

[17] H. H. Liu, H. Y. Zhang, and W. Li. Thermodynamic analysis on wetting behavior of hierarchical structured superhydrophobic surfaces. *Langmuir*, 27 (10):6260–6267, 2011.

[18] Tianqing Liu, Wei Sun, Xiangyu Sun, and Hongru Ai. Thermodynamic analysis of the effect of the hierarchical architecture of a superhydrophobic surface on a condensed drop state. *Langmuir*, 26(18):14835–14841, 2010.

[19] Yewang Su, Baohua Ji, Yonggang Huang, and Keh-chih Hwang. Nature's design of hierarchical superhydrophobic surfaces of a water strider for low adhesion and low-energy dissipation. *Langmuir*, 26(24):18926–18937, 2010. 80

[20] N. D. Hallam and T. C. Chambers. The leaf waxes of the genus *Eucalyptus* L'Héritier. *Australian Journal of Botany*, 18:335–386, 1970. 80

[21] W. Barthlott and C. Neinhuis. Purity of the sacred lotus, or escape from contamination in biological surfaces. *Planta*, 202:1–8, 1997. 83, 86, 87, 90

[22] Michael Nosonovsky and Bharat Bhushan. Roughness optimization for biomimetic superhydrophobic surfaces. *Microsystem Technologies*, 11:535–549, 2005. 90

[23] Anish Tuteja, Wonjae Choi, Minglin Ma, Joseph M. Mabry, Sarah A. Mazzella, Gregory C. Rutledge, Gareth H. McKinley, and Robert E. Cohen. Designing superoleophobic surfaces. *Science*, 318:1618–1622, 2007. 91, 92, 95

[24] Abraham Marmur. Wetting on hydrophobic rough surfaces: To be heterogeneous or not to be? *Langmuir*, 19(20):8343–8348, 2003. 96, 97

[25] Laura Barbieri, Estelle Wagner, and Patrik Hoffmann. Water wetting transition parameters of perfluorinated substrates with periodically distributed flat-top microscale obstacles. *Langmuir*, 23(4):1723–1734, 2007. 96, 100, 101

Chapter 5

Fabrication of hydrophobic surfaces using self-assembly and photo-lithography methods

5.1 Introduction

Many methods have been used to make hydrophobic surfaces, such as deposition [1], etching [2, 3], self-assembly [4] and lithography [5]. Except for few intrinsically hydrophobic materials[6], hydrophobization is both necessary and an efficient process to decrease surface energy and achieve superhydrophobicity on surface fabrication. Long-chain alkanes with structures similar to some leaf wax components, such as *n*-hexatriacontane (molecular formula $CH_3(CH_2)_{34}CH_3$), has been deposited on surfaces by a thermal evaporation method[7]. Silanes are another group of reagents for the hydrophobization purpose. Two types of silanes are usually used: normal silanes and functionalized silanes. The former usually

are fluorinated and can be used to coat a surface after dissolving in an organic solvent. The latter, usually containing reactive groups (-Cl, -OR, -NMe2) that are bonded to Si, however, can form a controllable coating through a self-assembly process in three steps.

Lithography is another common to fabricate surfaces with periodic micro-structures. Surfaces characterized with square or rhombus arrays of microscopic cylindrical posts have been fabricated using photolithography techniques to study the impacts of geometrical parameters on hydrophobicity[7–9]. Only one contact angle was recorded on each of these surfaces in the literature, as it is postulated that wetting on these micro-structured surfaces is symmetrical on all directions parallel to the surface horizon and therefore contact angles measured at different points along the contact line are identical.

However, different shapes, including octagons, squares, hexagons and circles, of a spreading droplet's bottom that is in contact with the surface were obtained on topographically patterned but chemically homogeneous surfaces[10–12]. This contradicts the general perception that only circles will be obtained on such surfaces. Furthermore, discrepancy has been found recently on contact angles measured at different directions on the micro-structures, with 128±2° versus 118±2° measured along the lattice axis and the diagonal directions, respectively, as shown in Fig. 5.1, on a sample with a pitch value of 20 μm[11].

On micro-textured of small gap sizes, it was reported that the liquid front advance velocity to the next row is much smaller than that on the perpendicular direction[10, 13]. In such a case, a zipping mechanism was introduced to explain anisotropic wetting. On large gap sizes, the velocities become comparable on the liquid front advance direction and the perpendicular direction[14]. Microscopic

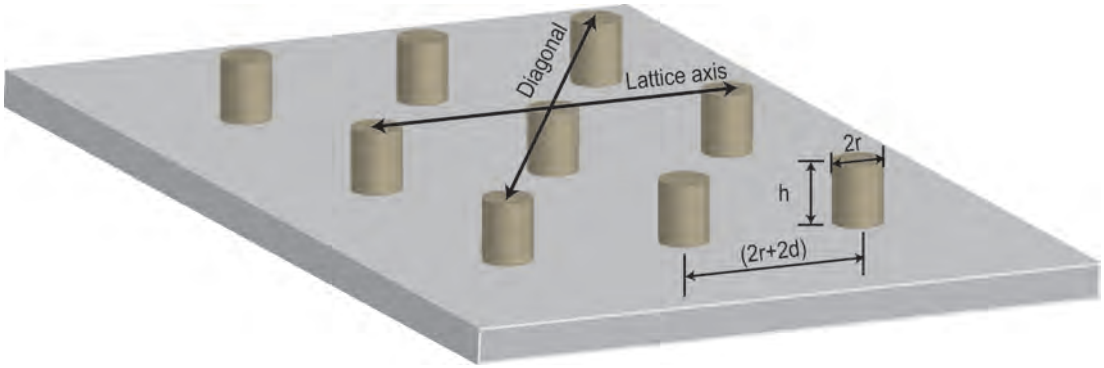

Figure 5.1: Illustration of square arrays of microposts on a surface.

images of an isopropanol contact line on micro-decorated surface revealed details of liquid front advancing among micro-pillar rows[10]. The contact line progression starts with wetting of one single micro-pillar of the next row, followed by wetting on the micro-pillars next to the first one on the same row. Eventually the whole contact line advances to the whole row of micro-pillars and gets ready for wetting on next row.

There are few reports with respect to different local wetting properties along the contact or triple phase line, termed anisotropic wetting here, on surfaces with symmetric periodic micro-structures, although asymmetric surfaces were specifically designed to study anisotropic wetting behaviours of droplets[15–18]. Herein, we first tested the self-assembly coating of oxysilane on glass slides, and explored the mechanism of specific anisotropic wetting properties on these micropost surfaces.

5.2 Experimental details

5.2.1 Self-assembly of hydrophobic films on glass slides

The surface modification of glass slides was carried out by immersing the slides in a hydrolysed silane solution. A 0.05 mol/L ethanol solution of oxysilane was firstly prepared by dissolving 0.20 g hexadecyltrimethoxysilane ($H_3C(CH_2)_{15}$-$Si(OCH_3)_3$, Sigma-Aldrich, Australia) into 10 mL ethanol. 4-fold molar excess of dilute H_2SO_4 solution (0.04 g) was added into the solution to hydrolyse the oxysilane. Glass slides were rinsed with ethanol and distilled water for three times before coating. Clean specimens were then immersed in the hydrolysed silane solution for 10 min, 30 min, 1 h, 2 h, and 4 h at room temperature, rinsed again with ethanol and distilled water for three times and placed in fume hood to dry for 4 h in air.

5.2.2 Fabrication of square arrays of microscopic cylindrical posts using photo-lithography

Samples with square arrays of microposts were fabricated in a normal photolithography process. Si wafers were pre-treated with acetone and isopropanol followed by baking on a hot plate at 150°C. The epoxy-based photoresist Su-8 50 was then spin-coated at speeds of 2500, 1800, 1400, 1000 rpm to achieve different thicknesses (40, 60, 80, 100 μm). After soft baking, the wafers were mounted into EVG mask aligner and exposed with UV at different intensities (260, 340, 420, 500 mJ/cm^2 based on the thickness). Post exposure baking, developing and hard baking of wafers were subsequently performed under programmed temperature

and time.

The corresponding geometrical parameters are defined in Fig. 5.1 for micro-posts in a surface (h for cylindrical height, $2r$ for cylindrical diameter, and $2d$ for cylindrical edge-to-edge distance). By varying these parameters, a total of 10 samples were fabricated.

5.2.3 Instrumentation

Contact angle measurements were performed at ambient temperatures using an FTA1000 Drop Shape Analysis instrument (B Frame System, First Ten Angstroms, Virginia, USA) equipped with an automated dispensing syringe and a computer-controlled title stage. Water droplets of 5 μL in volume were dispersed on fabricated samples. The contact angles were obtained by analyzing the sessile drop images using Drop Shape Analysis software affiliated with the instrument. Five drop tests were performed on each sample and the average angle was adopted for wetting characterization. In order to measure the roll-off angles, stage tilt angle was gradually increased at a speed of 1 deg/sec from 0° until the point where the water droplet started to move along the stage.

An RSX-1 Rotation Stage (Newport Research Corp (NRC), CA, USA) is placed on the FTA1000 sample stage to align the angles with the camera of the FTA1000 system.

Optical images were obtained using the Moticam 2300 digital camera (Motic Instruments Inc., B.C., Canada).

Coating surfaces were imaged using an atomic force microscope (AFM) (Ntegra Prima, NT-MDT Co., Moscow, Russia) in semi-contact mode. The coating

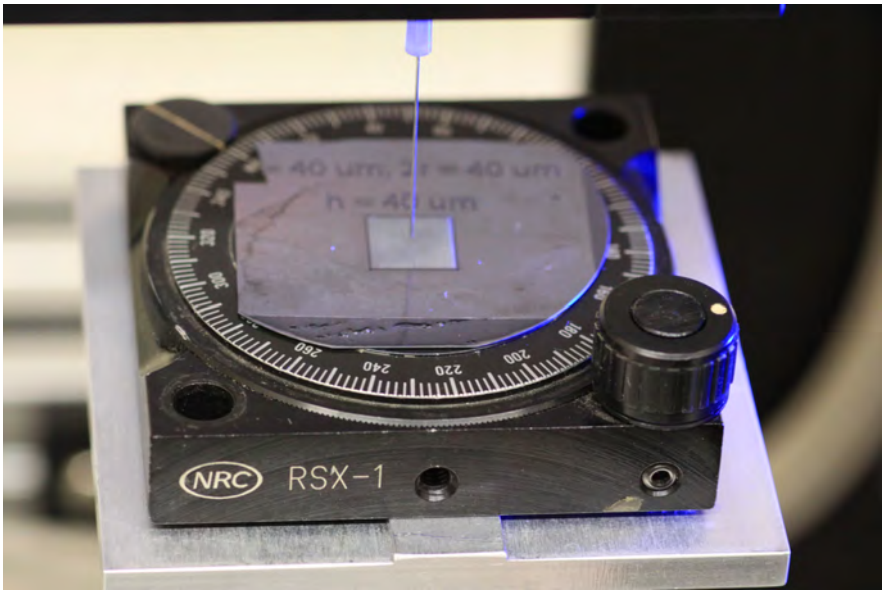

Figure 5.2: RSX-1 used to rotate the angles aligned with the camera in the FTA1000 system.

samples were fixed on adhesive tape before AFM scans were performed. The probe used contained a tetrahedral tip with a height of 14–16 μm and a typical curvature radius of 6 nm. The tip was mounted on a rectangular single crystal silicon (N-type, antimony doped) cantilever with a thickness of 2 μm, a resonant frequency of 140-390 kHz and a force constant of 3.1–37.6 N/m.

5.3 Results and discussion

5.3.1 Wetting properties of self-assembled coatings

Smooth bare glass slides have a contact angle of $30.8 \pm 1.6°$, which indicates a strong hydrophilic property. Simply immersing a smooth glass slide in a hydrolysed oxysilane solution led to a hydrophobic surface. For example, a 107.6° WCA

was obtained on a glass surface after 10 min immersion and a 112.7° WCA was observed on a surface after 1 h immersion (Fig. 5.3). Evidently, the oxysilane coating process has converted the glass slides from hydrophilic to hydrophobic. Different immersion times were trialled on smooth glass slides: 10 min, 30 min, 1 h, 2 h and 4 h. Greatest contact angle was observed on 1 h immersion (Table 5.1). It shows a simple process as short as 10 min could already coat a considerable hydrophobic coating on a surface.

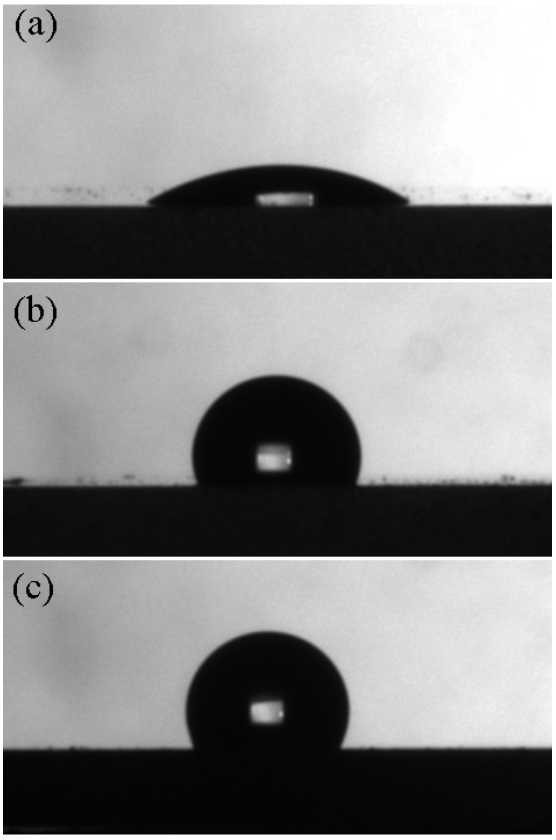

Figure 5.3: Contact angles on: (a) bare glass slide, 31.0°, (b) 10 min immersion in solution, 107.6°, (c) 1 h immersion in solution, 112.7°.

AFM images in Fig. 5.4 reveal the surface morphology of bare glass and coated glass slides at different immersion times. The roughness average values,

for example, root mean square (RMS) and roughness average, were determined over AFM images scanned in 50×50 μm^2 scale and presented in Table 5.1. The smooth bare glass surface had a 6.6 nm RMS and 5.3 nm roughness average. After coating, a 10 min immersion time created a surface with a 0.24 μm RMS and 0.19 μm roughness average. From 10 min to 1 h, the roughness values of coated surfaces increased. From 1 h to 4 h, the roughness values decreased in an unsteady way and so did the WCA. Among the different deposition times, 1 h deposition gives the highest RMS (0.55 μm) and roughness average (0.38 μm), and as well as the greatest contact angle (112.7°).

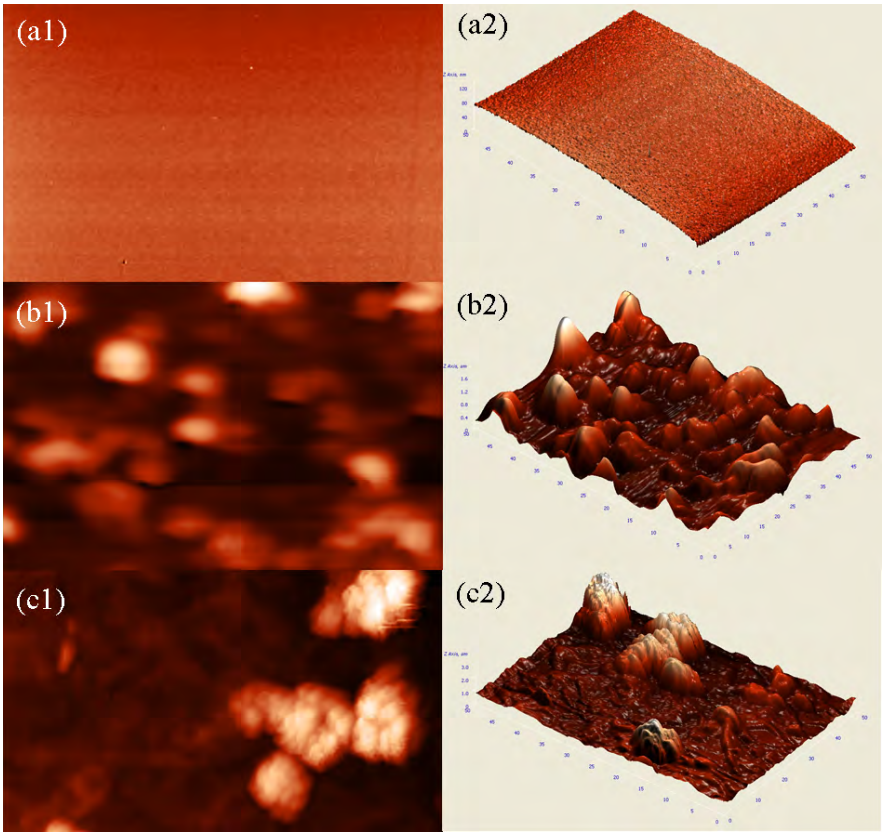

Figure 5.4: Surface morphology at 50×50 μm^2 scan scale of: (a) bare glass, (b) glass slide after 10 min immersion, (c) glass slide after 1 h immersion.

Table 5.1: Measured contact angles and roughness values.

Immersion time	WCA (°)	RMS (μm)	Roughness average (μm)
10 min	107.9 ± 1.6	0.24	0.19
30 min	103.1 ± 1.0	0.26	0.21
1 h	112.7 ± 2.1	0.55	0.38
2 h	105.3 ± 0.7	0.32	0.23
4 h	107.4 ± 1.2	0.41	0.30

The coating mechanism under mild conditions is worthy discussing, as this procedure provides an environmentally friendly and energy-efficient alternative. A self-assembly procedure is proposed here. Firstly, the functional moieties (-OCH_3) of oxysilane react with -OH groups in water and form silanetriols, which carry three reactive -OH groups in one single molecule (Fig. 5.5). The possibility cannot be ruled out that these oxysilane molecules are only partially hydrolysed. These silanetriols subsequently react with each other in the presence of protic acids and form dimers, trimers or polymers in a self-condensation procedure. The long alkyl groups on these polymerized molecules ensure the hydrophobicity of a surface coated with these polymers.

Further more, silanetriols can also form hydrogen bonding with the hydroxyl groups that usually appear on the glass surface. With the catalysis of H^+ ions, they react with the hydroxyl groups and form covalent bonds with two neighbouring hydroxyl groups (Fig. 5.6). By forming water molecules, the third hydroxyl groups on two neighbouring attached silanetriols can further react with each other to form Si–O–Si covalent bonds (not shown). Thus, a single layer of molecules can form on the glass surface with hydrophobic alkyl groups on the surface.

Fig. 5.7 depicts schematically the formation of an ordered amorphous polysilox-

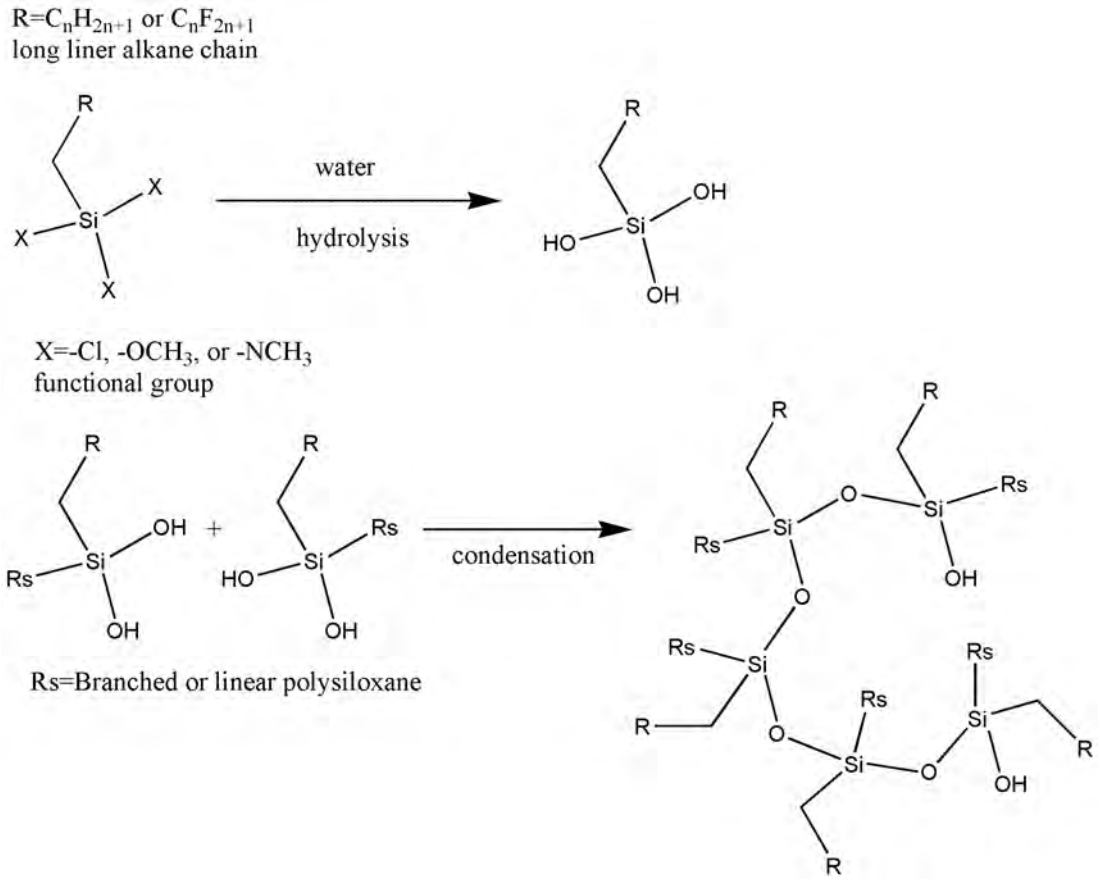

Figure 5.5: Hydrolysis and self-condensation of functionlized silanes [19].

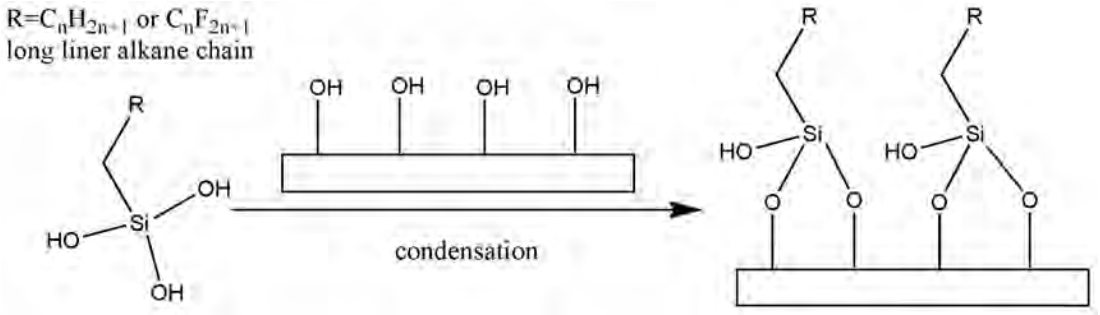

Figure 5.6: Silanetriols react with hydroxyl groups on the surface [20].

ane or homogeneous self-assembled monolayer [20]. Each unit represents a single silanol molecule after oxysilane hydrolysis, with the rounded head denoted as the

hydroxyl groups and the tail as the alkyl group on the other end.

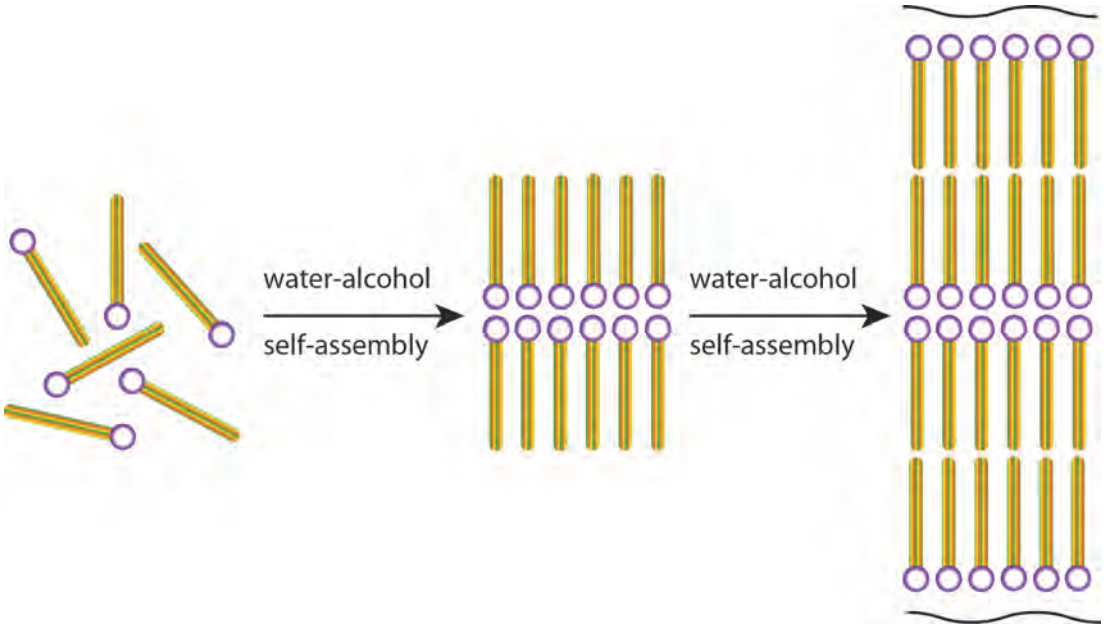

Figure 5.7: Self-assembly mechanism of silanetriols [20].

The existence of a mixed hydrophilic/hydrophilic environment (water and ethanol here) is essential for the self-assembly procedure [20]. Due to Van der Waals force and the hydrophilic/hydrophilic effect, silanol molecules self-organize to form a crystalline structure and this is similar to the common micelle procedure. It is expected that there is a competition between the silanol-silanol self-condensation and silanol self-assembly processes. Usually, the silanol-silanol self-condensation occurs much more slowly than the self-assembly process. In this study, the possibly dominating self-assembly process created bumpy surfaces on glass slides.

Several disadvantages of this procedure, however, were discovered. Within all the coating times including 10 min, translucent films were obtained on transparent glass slides. The ratio of water/ethanol can possibly be manipulated to control

the film thickness to meet certain optical requirements. Water droplets of 5 μL stuck firmly to the surface even when the surface was turned upside down. The roughness might also be controlled to reduce water adhesion by the surface, towards the fabrication of super hydrophobic surfaces. The upper layer of the film can be rubbed off easily, probably due to the weak interaction between layers. Dopamine, a mimic molecule of mussels' adhesive proteins, can be possibly added into the oxysilane solution, given its ability to self-polymerize in mild conditions (pH$\sim$8.5 in room temperature) and to stick to almost any surface [21].

5.3.2 Anisotropic wetting on micro-post surfaces fabricated with photo-lithography

Three groups of surfaces micro-textured with square arrays of microscopic cylindrical posts were designed and fabricated using photo-lithography. However, only data of samples with geometry confirmed by SEM are shown and discussed here. Fig. 5.8 shows the top views and SEM 45° views of two samples with same edge-to-edge distance ($2d$ = 25 μm) and diameter ($2r$ = 50 μm) but different cylindrical heights (h = 60 and 65 μm). Two samples are denoted here as H60 and H65 based on their actual cylindrical heights.

5.3.2.1 Contact angles on micro-post surfaces

Based on the surface geometry shown in Fig. 5.1, there are four axisymmetric axes: two lattice lines and two diagonal lines. Water contact angles (WCA) on lattice and diagonal directions were obtained when aligning these two lines perpendicular to the observation direction. The side views of water droplets on

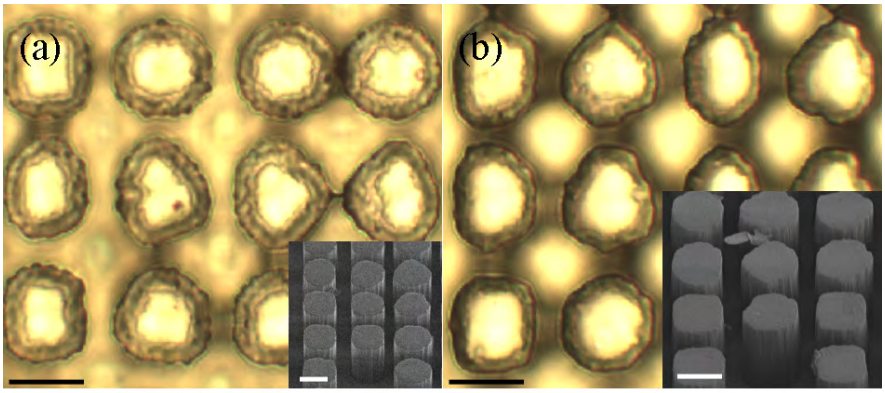

Figure 5.8: Optical top-views and SEM images of micro-posts with same $2r$ and $2d$ but varying heights: (a) $h = 60$ μm and (b) $h = 65$ μm (all scale bars = 50 μm).

samples H60 and H65 when the two directions were aligned up are compared in Fig. 5.9. A distinct difference was also found on the water-surface contact areas, from which WCA values were obtained. In addition, the bright spots in the centre of the droplets, caused by the diffraction of light through the droplet, have rectangle and square shapes respectively. Contact angles measured on the lattice axis and the diagonal line directions are denoted as θ_{la} and θ_{di}, respectively. A distinct difference of approximate 15° between WCA values obtained on two directions for the same sample was present.

Predicted contact angles were calculated using the Wenzel[22] and Cassie[23] equations. The roughness factor for a Wenzel regime has the expression of $r_W = 1+2\pi rh/(2d+2r)^2$, where an increase of h leads to an increase of the $cos\theta_W$ value and thus the Wenzel contact angle θ_W. The fraction of solid contacted by water can be stated as $f = \pi r^2/(2d+2r)^2$ in a Cassie scenario, where h doesn't appear in the equation. The roughness of the flat tops, r_f, was reasonably taken as unity to calculate the Cassie contact angle θ_C. In calculations of theoretical contact

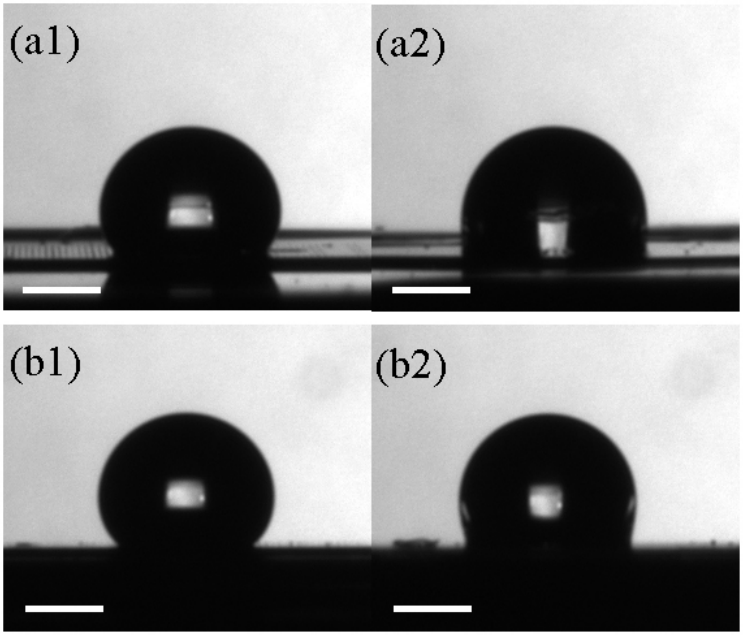

Figure 5.9: Contact angles measured at (1) the lattice direction and (2) the diagonal direction by depositing a 5 μL water droplet on samples (a) H60 and (b) H65. Scale bar = 1.0 mm.

angles, 79° was adopted as the static water contact angle on the photoresist Su-8 smooth surfaces[24].

Roughness ratios "on the line" were also adopted to analyze contact angles at different directions[11]. In these cases, 1D liquid-solid contact is considered instead of 2D contact areas. For a homogeneous wetting, roughness ratios on the lattice axis direction and the diagonal line direction can be stated as $r_{W-la} = 1 + 2h/(2d+2r)$ and $r_{W-di} = 1+2h/[\sqrt{2}(2d+2r)]$, respectively. For a heterogeneous wetting, fractions of solid contacted by water on the lattice axis direction and the diagonal line direction can be stated as $f_{la} = 2r/(2d+2r)$ and $f_{di} = 2r/[\sqrt{2}(2d+2r)]$, respectively. The corresponding predicted contact angles at two wetting regimes and two directions, θ_{W-la}, θ_{W-di}, θ_{C-la} and θ_{C-di} are summarized in

Table 5.2.

Table 5.2: WCA experimental and prediction using Wenzel and Cassie relations.

WCA	H60	H65
θ_{la}	117.3 ± 2.2	119.4 ± 1.4
θ_{di}	102.5 ± 1.6	100.9 ± 1.7
θ_W	59.2	57.4
θ_{W-la}	66.0	64.9
θ_{W-di}	60.2	58.6
θ_C	140	140
θ_{C-la}	116.1	116.1
θ_{C-di}	101.7	101.7

For the two samples, the calculated contact angles has a range of 57–59° when using the Wenzel equation and an identical angle of 140° when using the Cassie relation. Measured contact angles, θ_{la} (117–119°) and θ_{di} (100–102°), fall between predicted ones using two models. It can be deduced that the classic homogeneous and heterogeneous models cannot be used here to directly explain the wetting on these micro-post surfaces. Predicted Cassie WCA, θ_{C-la} (116.1°) and θ_{C-di} (101.7°), however, are close to experimental ones. Therefore, the liquid-solid contact fraction calculation using the current method "on the line" is reasonably applicable here. Another similar method, the contact fraction on the contact triple line, has also been introduced to successfully calculate contact angles on micro-patterned surfaces[12]. This method will be discussed when the contact triple lines are determined in later experiments. It can be deduced that metastable Cassie wetting scenarios must exist on these surfaces, namely water entering the asperities among the micro-posts but not yet touching the bottom.

5.3.2.2 Water droplet and contact area patterns

Optical top views of water droplets of 1 μL in volume on these micro-decorated surfaces show quasi-circular perimeters with similar radii (Fig. 5.10a). Since all measured WCA values are greater than 90°, the contact triple lines were blocked by the droplet contours when viewing from the top. The liquid-surface contact area was obtained after upper liquid was carefully removed with paper towel[11]. Squircle-shaped contact footprints were formed on these surfaces (Fig. 5.10b). There is a minor difference between what was observed here and a systematic study of imbibition on micro-decorated surfaces on square and hexagon lattices[10]. In the four corners of square contact footprints, the contact line rests on two micro-posts across the diagonal direction of one single square lattice. In literature, either a rectangle or a straight line was presented in these corners so that the corresponding square or octagon shape was obtained.

Another observation that has to be pointed out is, the contact triple line tends to stop on the diameter of the micro-posts, as the spinning force on a single micro-post becomes the greatest at this position. This agrees with the reported theoretical reasoning[25] and experiments[12]. The Cassie relation "on the triple line" is more reasonably to be applied here[12]. On the straight lines of the square shape that is also the lattice axis direction while measuring the WCA, fraction of liquid-solid contact can be stated as $f_{la} = 2r/(2d + 2r)$, which remains the same as previously calculated. In the four corners of the square shape that is also the lattice axis direction while measuring the WCA, fraction of liquid-solid contact can be stated as $f_{di} = 2r/[\pi(2d + 2r)/2]$. For these four samples, as the height h doesn't appear on these two expressions, the constant

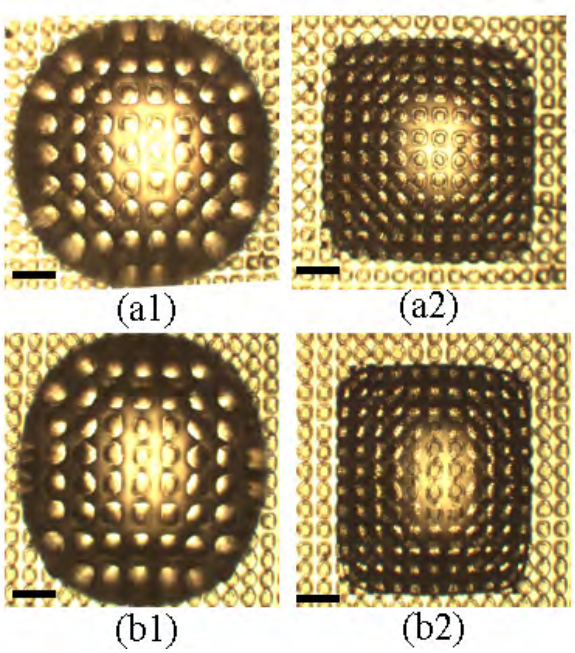

Figure 5.10: Top views (1) of 1 μL water droplets resting on fabricated surfaces (a) H60 and (b) H65 and the contact area footprint (2) after upper water was carefully removed. Scale bar = 200 μm.

Cassie WCA values are obtained as $\theta_{C-la-triple} = 120.0°$ and $\theta_{C-di-triple} = 101.7°$. The calculated $\theta_{C-la-triple}$ value is also close to the observed WCA values on the lattice direction (119.4±1.4° on sample H65).

It can also be observed From Fig. 5.10 that the diagonal line lengths of the squircle-shaped footprints are approximately close to the diameters of the corresponding hypoellipse perimeters. The 3D shape of the droplets on these samples can be constructed from the base as a squircle-shaped contact area with the micro-textured surfaces developing upwards into a quasi-circular contour with the greatest perimeter and continuously concluding as a dome. With close droplet heights measured from the top to the surface, it thus can be deduced easily that the contact angles measured on the diagonal line direction are smaller than these

measured on the lattice direction, since the length of the former is longer than that the latter while the contour on the surface plane is transforming gradually from a squircle into a circle.

The effects of droplet volume on contact patterns were also studied by gently depositing water droplets of varying volumes (1, 3, 5, 7, 9 μL) onto the same specimen (Fig. 5.11). Similar quasi-circular droplet contours and squircle-shaped contact patterns are obtained with different sizes as the droplet volume changes. A curve, instead of a straight line, is explicitly observed on the corners of the contact patterns with bigger droplet volumes.

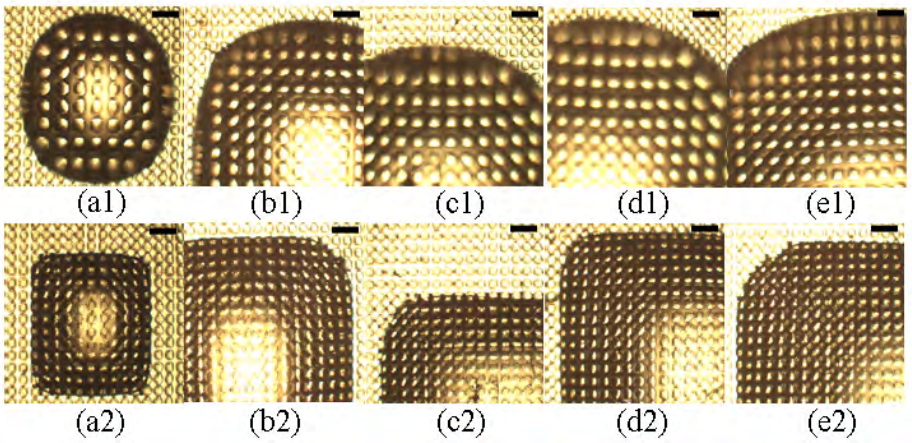

Figure 5.11: Top views of water droplets (1) of varying volumes on sample H65 and the contact area footprints (2): (a) 1 μL, (b) 3 μL, (c) 5 μL, (d) 7 μL, (e) 9 μL. Scale bar = 200 μm.

5.3.2.3 Contact base lengths along the contact line

Comprehensive data for water droplets of varying volumes on all four samples are summarized in Table 5.3. A few observations can be found here: (1) Contact angles are always greater on the lattice direction than on the diagonal direction,

(2) Water contact base lengths are always shorter on the lattice direction than on the diagonal direction, (3) Droplet volume does not affect significantly contact angles measured on the same sample, (4) Only minor difference in contact angle is found on different samples of varying micro-post heights, (5) Water contact base lengths measured on both the lattice and the diagonal direction increase gradually with the droplet volume, but the difference between these two base lengths can be considered constant (0.2–0.3mm) throughout Table 5.3.

Table 5.3: Contact angles and base lengths measured with water droplets of varying volumes on group-1 samples with varying micro-post height h on the lattice direction (denoted as "la") and the diagonal direction (denoted as "di").

Sample		1 μL		3 μL		5 μL		7 μL		9 μL	
		CA (°)	Base (mm)	CA (°)	Base (mm)	CA (°)	Base (mm)	CA (°)	Base (mm)	CA (°)	Base (mm)
H60	la	103	1.2	120	1.6	125	1.8	125	2.0	123	2.3
	di	85	1.5	103	1.9	110	2.1	110	2.3	104	2.6
H65	la	120	1.0	120	1.5	125	1.8	124	2.1	130	2.1
	di	103	1.2	110	1.7	110	2.1	110	2.3	113	2.4

When comparing the contact lengths on the lattice and diagonal directions obtained from side views and contact footprints, the lengths obtained from side views are always longer than the other. Considering the contact footprint are obtained by carefully removing the upper liquid, it can be reasonably postulated that the droplets deposited on these micro-textured surfaces have a contact regime as shown in Fig. 5.12. This is to say, water fills the asperities of the inner contact area and a metastable composite wetting scenario is present in the outer contact area. When the upper liquid of the droplet is removed, the liquid near the outer contact area detaches from the micro-posts and leaves only the contact area that

the pores in the roughness are filled with water.

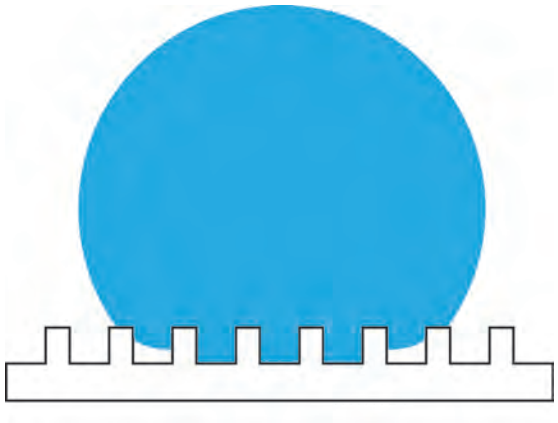

Figure 5.12: Sketch of a droplet on micro-textured surfaces.

5.3.2.4 Tilt stage experiments

Water droplets of 5 μL adhered firmly to the surfaces of H60 and H65 without contact line movement while the surfaces were tilted gradually from horizontal (0°) to vertical (90°) at a speed of 1 deg/sec. The WCA values measured at the front and back of the droplet on sample H60 are shown in Fig. 5.13. When the surface tilt angle increased, the front contact angle increased slowly (from 117 to 122°) and the back contact angle decreased at a relatively large slope (from 117 to 109°).

The front and back contact angles, even though different from advancing and receding angles, respectively, can provide adhesion information between the droplet and the surface during the tilting process. The roll-off angle α of drop can be estimated by the following relation[26]:

$$(\cos\theta_{Rec} - \cos\theta_{Adv})\gamma_{LV} = mg\sin\alpha/r_{drop} \tag{5.1}$$

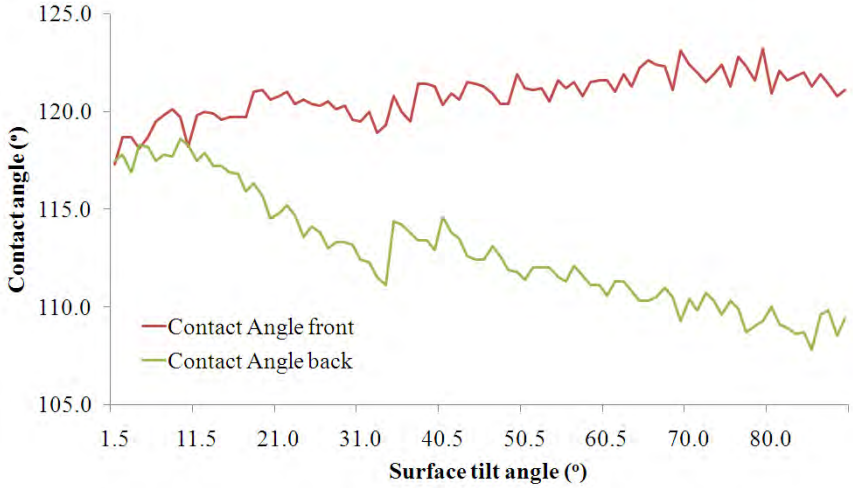

Figure 5.13: Contact angles measured at the front and back of the droplet on sample H60 at different surface tilt angles.

Previous report[27] has demonstrated that no kinetic barrier exists for advancing but it does for receding part of a droplet. The energy barrier to be overcome by the droplet for movement equals the energy that the work of adhesion does along the receding edge of the droplet.

The dynamic values of front and back contact angles can be an analogue to the relation of advancing and receding angles stated in eq 5.1. The $\cos\theta_{back} - \cos\theta_{front}$ value, can reasonably be related to the adhesion force between the droplet and the surface at different surface tilt angles. The change of this value with surface tilt angle is shown in Fig. 5.14. A trendline in black with a 0.91 R-squared value was approximated based on the actual $\cos\theta_{back} - \cos\theta_{front}$ values. As indicated by the trendline, the liquid-surface adhesion increases linearly with the surface tilt angle during the tilt experiment at range 0–90°.

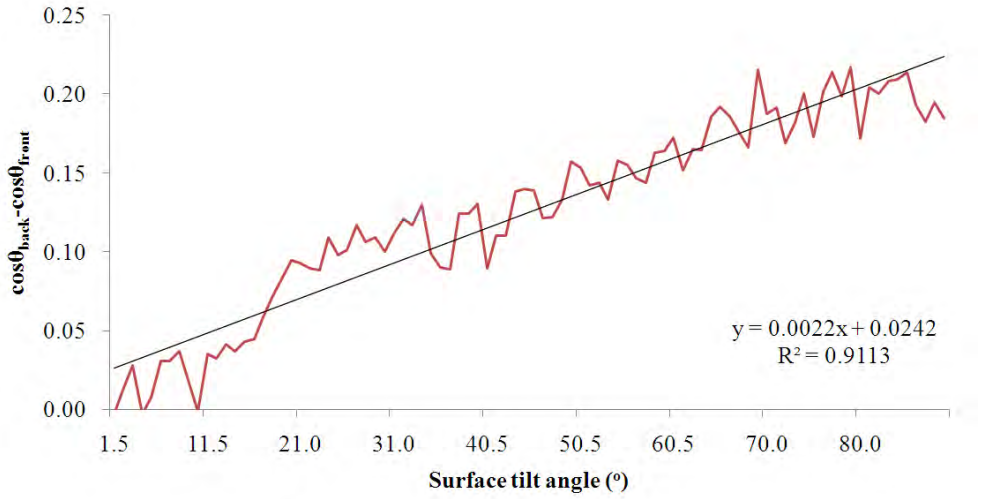

Figure 5.14: The $(\cos\theta_{back} - \cos\theta_{front})$ value versus surface tilt angle on sample H60 with a black trendline.

5.4 Conclusions

Different fabrication methods, for example self-assembly and photo-lithography, were investigated in this chapter to make hydrophobic surfaces. Experiments showed that brief immersion of glass slides in an ethanol solution of hydrolysed oxysilane lead to a hydrophobic surface with micrometer roughness. The self-assembly mechanism of oxysilane at ambient temperatures was also explained using Chemistry and molecular interaction concepts. Hydrophobic surfaces with square arrays of microscopic cylindrical posts were micro-textured on hydrophilic materials using photo-lithography. Anisotropic wetting, namely two distinct contact angles obtained on different directions, was observed on these surfaces. The contact angle values were successfully explained by roughness "on the line" and the Cassie equation. Squircle-shaped contact patterns were observed on droplets resting on these surfaces. A nearly constant difference was revealed between the

base lengths measured on the lattice and the diagonal directions. Finally, the adhesion between the droplet and the surface was found to approximately change linearly with the surface tilt angle.

References

[1] K. K. S. Lau, J. Bico, K. B. K. Teo, M. Chhowalla, G. A. J. Amaratung, W. I. Milne, G. H. McKinley, and K. K. Gleason. Superhydrophobic carbon nanotube forests. *Nano Letters*, 3:1701–1705, 2003. 113

[2] Baitai Qian and Ziqiu Shen. Fabrication of superhydrophobic surfaces by dislocation-selective chemical etching on aluminum, copper, and zinc substrates. *Langmuir*, 21(20):9007–9009, 2005. 113

[3] Kerstin Koch, Bharat Bhushan, Yong Chae Jung, and Wilhelm Barthlott. Fabrication of artificial lotus leaves and significance of hierarchical structure for superhydrophobicity and low adhesion. *Soft Matter*, 5:1386–1393, 2009. 113

[4] Bharat Bhushan, Kerstin Koch, and Yong Chae Jung. Biomimetic hierarchical structure for self-cleaning. *Applied Physics Letters*, 93:093101–093101–3, 2008. 113

[5] Reiner Furstner, Wilhelm Barthlott, Christoph Neinhuis, and Peter Walzel. Wetting and self-cleaning properties of artificial superhydrophobic surfaces. *Langmuir*, 21:956–961, 2005. 113

[6] Gisele Azimi, Rajeev Dhiman, Hyuk-Min Kwon, Adam T. Paxson, and

Kripa K. Varanasi. Hydrophobicity of rare-earth oxide ceramics. *Nature Materials*, 12(4):315–320, 2013. 113

[7] Bharat Bhushan and Eun Kyu Her. Fabrication of superhydrophobic surfaces with high and low adhesion inspired from rose petal. *Langmuir*, 26(11):8207–8217, 2010. 113, 114

[8] Laura Barbieri, Estelle Wagner, and Patrik Hoffmann. Water wetting transition parameters of perfluorinated substrates with periodically distributed flat-top microscale obstacles. *Langmuir*, 23(4):1723–1734, 2007.

[9] Laura Vogelaar, Rob G. H. Lammertink, and Matthias Wessling. Superhydrophobic surfaces having two-fold adjustable roughness prepared in a single step. *Langmuir*, 22(7):3125–3130, 2006. 114

[10] Laurent Courbin, Etienne Denieul, Emilie Dressaire, Marcus Roper, Armand Ajdari, and Howard A. Stone. Imbibition by polygonal spreading on microdecorated surfaces. *Nature Materials*, 6(9):661–664, 2007. 114, 115, 128

[11] Xiying Li, Liqun Mao, and Xuehu Ma. Dynamic behavior of water droplet impact on microtextured surfaces: The effect of geometrical parameters on anisotropic wetting and the maximum spreading diameter. *Langmuir*, 29(4): 1129–1138, 2013. 114, 126, 128

[12] Simon Tylsgaard Larsen and Rafael Taboryski. A cassie-like law using triple phase boundary line fractions for faceted droplets on chemically heterogeneous surfaces. *Langmuir*, 25(3):1282–1284, 2009. 114, 127, 128

[13] Mauro Sbragaglia, Alisia M. Peters, Christophe Pirat, Bram M. Borkent,

Rob G. H. Lammertink, Matthias Wessling, and Detlef Lohse. Spontaneous breakdown of superhydrophobicity. *Phys. Rev. Lett.*, 99:156001, Oct 2007. 114

[14] A.M. Peters, C. Pirat, M. Sbragaglia, B.M. Borkent, M. Wessling, D. Lohse, and R.G.H. Lammertink. Cassie-baxter to wenzel state wetting transition: Scaling of the front velocity. *The European Physical Journal E*, 29(4):391–397, 2009. 114

[15] Jihua Zhang, Zhongjun Cheng, Yongmei Zheng, and Lei Jiang. Ratchet-induced anisotropic behavior of superparamagnetic microdroplet. *Applied Physics Letters*, 94(14):144104, 2009. 115

[16] Susan Daniel, Sanjoy Sircar, Jill Gliem, and Manoj K. Chaudhury. Ratcheting motion of liquid drops on gradient surfaces. *Langmuir*, 20(10):4085–4092, 2004.

[17] Kuang-Han Chu, Rong Xiao, and Evelyn N. Wang. Uni-directional liquid spreading on asymmetric nanostructured surfaces. *Nature Materials*, 9(5): 413–417, 2010.

[18] O. Sandre, L. Gorre-Talini, A. Ajdari, J. Prost, and P. Silberzan. Moving droplets on asymmetrically structured surfaces. *Phys. Rev. E*, 60:2964–2972, Sep 1999. 115

[19] Xiaoyan Song, Jin Zhai, Yilin Wang, and Lei Jiang. Fabrication of superhydrophobic surfaces by self-assembly and their water-adhesion properties. *The Journal of Physical Chemistry B*, 109(9):4048–4052, 2005. 122

[20] Qingping Ke, Guanglu Li, Yue Liu, Tao He, and Xue-Mei Li. Formation of superhydrophobic polymerized n-octadecylsiloxane nanosheets. *Langmuir*, 26(5):3579–3584, 2010. 122, 123

[21] Haeshin Lee, Norbert F. Scherer, and Phillip B. Messersmith. Single-molecule mechanics of mussel adhesion. *Proceedings of the National Academy of Sciences*, 103(35):12999–13003, 2006. 124

[22] Robert N. Wenzel. Resistance of solid surfaces to wetting by water. *Industrial & Engineering Chemistry*, 28(8):988–994, 1936. 125

[23] A. B. D. Cassie and S. Baxter. Wettability of porous surfaces. *Trans. Faraday Soc.*, 40:546–551, 1944. 125

[24] Zhan Gao, David B Henthorn, and Chang-Soo Kim. Enhanced wettability of an su-8 photoresist through a photografting procedure for bioanalytical device applications. *Journal of Micromechanics and Microengineering*, 18 (4):045013, 2008. 126

[25] Gene Whyman, Edward Bormashenko, and Tamir Stein. The rigorous derivation of young, cassie—baxter and wenzel equations and the analysis of the contact angle hysteresis phenomenon. *Chemical Physics Letters*, 450(4–6): 355–359, 2008. 128

[26] Wei Chen, Alexander Y. Fadeev, Meng Che Hsieh, Didem Oner, Jeffrey Youngblood, and Thomas J. McCarthy. Ultrahydrophobic and ultralyophobic surfaces: Some comments and examples. *Langmuir*, 15(10):3395–3399, 1999. 132

[27] Lichao Gao and Thomas J. McCarthy. The "lotus effect" explained:two reasons why two length scales of topography are important. *Langmuir*, 22 (7):2966–2967, 2006. 133

Chapter 6

Wetting and mechanical properties of fluorinated diamond-like carbon coatings

6.1 Introduction

Diamond-like carbon (DLC) is an amorphous form of chemically integrated diamond and graphite carbons, including a substantial proportion of the former. Diamond carbons in the sp^3 electron configuration contribute significant hardness, mechanical durability and chemical inertness [1, 2], while graphite carbons with hybridised sp^2 orbitals provide electron conductivity. Different chemical elements can be incorporated into a DLC coating to modify its surface energy, mechanical hardness and biocompatibility for potential applications [3–5]. Specifically, fluorine can be incorporated by applying a reactive fluorine-containing gas, such as CF_4, C_2F_4, and C_2F_6 together with a hydrocarbon gas such as CH_4 during

the plasma process [6]. The fluorine content can be manipulated by varying the ratio of hydrocarbon gas to fluorine gas in the mixture. Fluorinated diamond-like carbon (F-DLC) coatings substantially lower coefficient of friction, Young's modulus and surface free energy values than fluorine-free counterparts [7–9]. F-DLC coatings also suppress protein adsorption and platelet activation and thus become useful for blood-contacting devices [10]. In general, appropriate F-DLC coatings are potentially useful for hydrophobic-related applications.

Common DLC deposition methods can involve Physical Vapour Deposition (PVD) or Chemical Vapour Deposition (CVD) [2]. Generally, CVD creates much smoother coatings than PVD. F-DLC coatings have been fabricated by an RF or DC Plasma Enchanced Chemical Vapour Deposition (PECVD) method to exploit antithrombogenicity [4], inhibition of protein adsorption [10], antibacterial activity [11], and biofouling reduction [12]. A Closed-Field Unbalanced Magnetron Sputtering (CFUBMS) system with its origins in the basic sputtering technique, gradually developed from the conventional balanced magnetron in the 1970s, to the unbalanced magnetron in the 1980s, and to the multi-source, closed-field system in the 1990s [13]. CFUBMS has now prevailed over PVD methods for preparing functional coatings, whose qualities are comparable to those achieved with other CVD methods. Moreover, its advantages over PECVD, the most popular laboratory method, including versatility, widespread use and scalability, make this technique very promising for commercial purposes.

Unfortunately, there are few reports on wetting and mechanical properties of F-DLC coatings prepared by CFUBMS. In this study, DLC and F-DLC coatings were fabricated by varying the CF_4 gas flow rate during the film deposition stage of the CFUBMS method to optimise the combination of desirable proper-

ties for hydrophobic purposes. Specifically, surface chemistry, wetting property, morphology, mechanical, and finite element analyses were performed on the fabricated samples.

6.2 Experimental details

6.2.1 Preparation of DLC and F-DLC coatings

The DLC coatings were deposited onto stainless steel and Si(100) substrates using a closed-field unbalanced magnetron sputtering system (UDP650/6, Teer Coatings Ltd., UK). Inside the sputtering chamber, six rectangular cathodes were evenly distributed around a 270 mm diameter substrate holder. Two pure Cr targets and four pure graphite targets were coupled with these opposed cathodes. A bias with pulse DC at a frequency of 250 kHz was applied to the substrate. The target-to-substrate distance and rotation speed of the substrate holder were maintained at 190 mm and 10 rpm, respectively. Prior to deposition, the sputtering chamber was evacuated to a background pressure of 4×10^{-4} Pa and substrates were sputter cleaned at a bias of -500 V for 30 min with the presence of Ar gas, in order to remove oxide layers and surface contaminants. The 30 sccm flow rate of 99.995 % pure Ar gas created a working gas pressure of 0.17 Pa.

In the deposition stage, a 0.2 μm adhesive Cr layer was prepared by first applying a -80 V bias voltage for 5 min with a 5.0 A (DC) for Cr(2). Then a composition gradient layer of CrCx ($\sim$0.4 μm) was deposited for load support by varying the Cr(2) current from 5.0 to 0 A and C(4) current from 0 to 3.0 A while concurrently applying a -80 V bias voltage for 20 min. Finally, the DLC

top layer of approximately 0.7 μm in thickness was formed by sputtering the graphite targets with a power of $\sim$2 kW and maintaining the bias voltage at -80 V and the C(4) current at 3.0 A (DC) for 60 min. No additional heating were provided during the deposition procedure. The fluorine element addition into DLC coatings was realized by introducing 99.995 % pure CF_4 gas into the chamber in the final deposition stage at different flow rates (0, 5, 10, 15, 20, 15, 30 sccm).

Each F-DLC film was denoted according to the CF_4 flow rate; for example, F-DLC10 indicates that the F-DLC film was deposited at the 10 sccm CF_4 flow rate.

6.2.2 Contact angle measurements

Contact angle measurements were performed at ambient temperatures using an FTA1000 Drop Shape Analysis instrument (B Frame System, First Ten Angstroms, Virginia, USA) equipped with an automated dispensing syringe and a computer-controlled title stage. Water droplets of 5 μL were dispersed on fabricated samples. The contact angles were obtained by analyzing the sessile drop images using the Drop Shape Analysis software version 2.1 affiliated with the instrument. Five drop tests were performed on each sample and the average angle was adopted for wetting characterization.

6.2.3 Surface characterization

The coating surface was imaged using an atomic force microscope (AFM) (Ntegra Prima, NT-MDT Co., Moscow, Russia) in semi-contact mode. The coating

samples were fixed on adhesive tape before AFM scans were performed. The probe used contained a tetrahedral tip with a height of 14–16 μm and a typical curvature radius of 6 nm. The tip was mounted on a rectangular single crystal silicon (N-type, antimony doped) cantilever with a thickness of 2 μm, a resonant frequency of 140–390 kHz and a force constant of 3.1–37.6 N/m.

6.2.4 Surface chemistry

Surface elemental composition and chemical bond species were acquired using a Kratos Axis ULTRA X-ray Photoelectron Spectrometer (Manchester, UK) incorporating a 165 mm hemispherical electron energy analyser. The incident radiation was Monochromatic Al K X-rays (1486.6 eV) at 225 W (15 kV, 15 mA). Survey (wide) scans were taken at an analyser pass energy of 160 eV and multiplex (narrow) high resolution scans at 20 eV. Survey scans were carried out over 1200–0 eV binding energy range with 1.0 eV steps and a dwell time of 100 ms. Narrow high-resolution scans were run with 0.05 eV steps and 250 ms dwell time. Base pressure in the analysis chamber was 1.0×10^{-9} torr and during sample analysis 1.0×10^{-8} torr. Atomic concentrations were calculated using the CasaXPS software version 2.3.16 and a Shirley baseline with Kratos library Relative Sensitivity Factors (RSFs). The main C1s component attributed to C-C and C-H bonds at 284.6 eV was chosen as a reference for calibrating the energy scale. Peak fitting of the high-resolution spectra was also carried out using CasaXPS software.

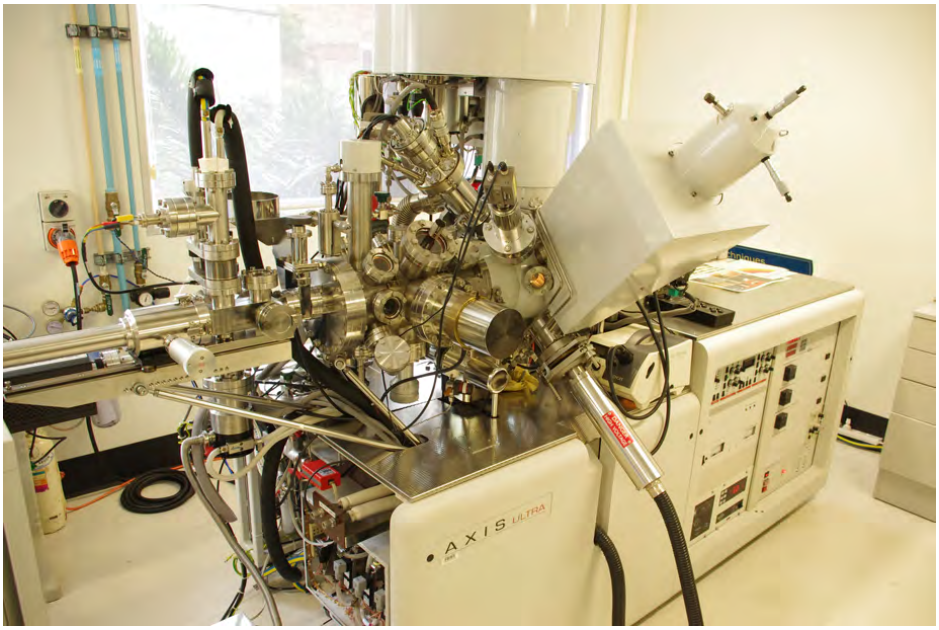

Figure 6.1: A Kratos Axis ULTRA X-ray Photoelectron Spectrometer used for surface chemistry characterization.

6.2.5 Mechanical tests

A nanoindentation workstation (Ultra-Micro Indentation System 2000, CSIRO, Sydney, Australia), equipped with a spherical Berkovich indenter (5 μm radius) [14], was used to measure the mechanical properties of the coatings. Nanoindentation was carried out under load control with a maximum load of 3 mN, under which the maximum penetration depth was found to be less than 10% (0.15 μm) of the film thickness. In this way it was ensured that only the film properties were measured. For each individual measurement, 10 incremental and 10 decremental steps were used, respectively. For each sample, 25 measurements were performed and the corresponding results were collected for determining the mean and standard error.

6.2.6 Finite Element Analysis

Finite element modelling (FEM) was used to analyse the physical response of the coating system to external loading. A two-dimensional (2D) axisymmetric model was constructed with the loading direction along the axial z axis, using COMSOL software version 4.3. Input parameters consisted of both structural and mechanical properties of the coating systems obtained from experiments (see results and discussion section). The model set-up has been described previously [15, 16], and is briefly summarized below. The model assembly was comprised of a coating (1.5 μm thick) on a stainless steel substrate (48.5 μm thick) frequently used for surgical equipments. Accordingly, the simulation block was a rectangle measuring 50×50 μm^2. The surface of the coating was loaded under a spherical tipped indenter with a radius of 5 μm. The coating was assumed to be bonded perfectly to the substrate. Time-dependent deformation behaviours such as creep, as well as surface roughness and contamination, were not considered in our simulations. The contact between the indenter and the sample was assumed to be frictionless. The bottom of the simulation model (z = 50 μm) was fixed in the z direction, while the right edge of the block (x = 50 μm) was fixed in the x direction. The axisymmetric axis coincided with the left edge of the simulation block (x = 0), as such, 3D effects could be evaluated. The tip of the indenter was located at z = 0 μm at the beginning of the simulation. The indentation loading process was simulated as downward movements in successive steps of 0.01 μm each, beginning from 0 up to 0.4 μm.

6.3 Results and discussion

6.3.1 Surface chemical composition

Elements in the surfaces of DLC and F-DLC samples were identified as C, N, O, and F, based on their corresponding 1s peak binding energies at 284.6, 399.3, 532.3, 687.3 eV. In contrast to the fluorine-free DLC sample (Fig. 6.2a), a distinct F 1s peak appears in the XPS survey scans for all F-DLC samples, for example F-DLC20 in Fig. 6.2b.

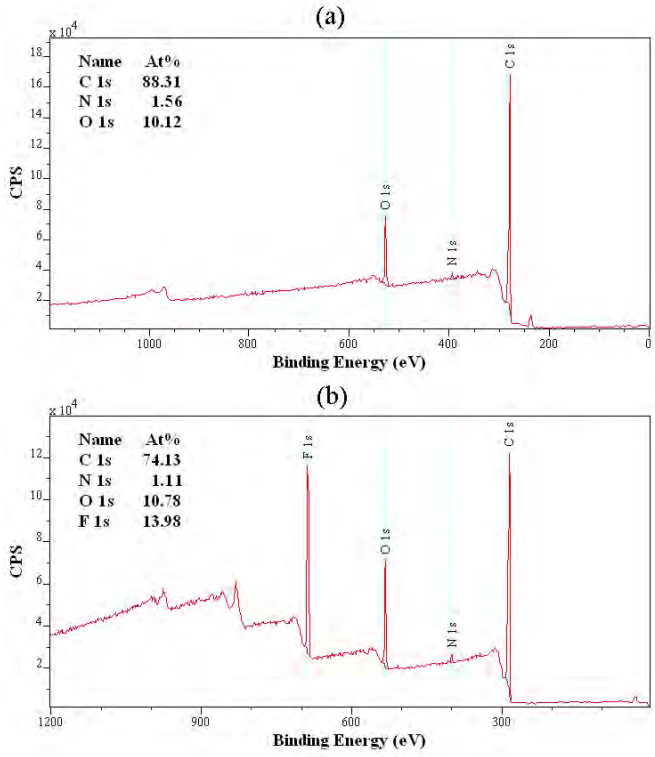

Figure 6.2: XPS survey scans for (a) DLC and (b) F-DLC20.

The atomic percentages for each element were calculated from the normalized peak areas on the XPS survey spectra. Table 6.1 indicates that the carbon content

decreases and the fluorine content increases when the CF_4 flow rate increases from 0 to 20 sccm. Thus F/C atomic ratio also increases from 0 to 0.19 during the same flow rate change (Fig. 6.3). However, when the flow rate was increased to 25 and 30 sccm, both the fluorine content and the F/C ratio remained relatively constant at approximately 10 at.% and 0.14, respectively (Fig. 6.3, blue line). A similar trend was found for the F/C ratio when the sample surfaces were briefly etched by ions prior to XPS scanning (Fig. 6.3, red line).

Table 6.1: Thicknesses, atomic percentages and F/C ratios for DLC and F-DLC samples.

Sample	Thickness (μm)	C1s (at.%)	N1s (at.%)	O1s (at.%)	F1s (at.%)	F/C
DLC	1.2	93.2	0.8	5.9	0.2	0.00
F-DLC5	1.4	88.7	0.4	5.6	5.4	0.06
F-DLC10	1.5	85.6	0.5	5.9	8.0	0.09
F-DLC15	1.5	81.8	0.6	6.1	11.5	0.14
F-DLC20	1.7	80.4	0.8	6.2	12.6	0.16
F-DLC25	1.7	81.7	1.3	7.1	9.9	0.12
F-DLC30	-	82.9	1.4	7.1	8.6	0.10

Both DLC and F-DLC samples contain a negligible amount of nitrogen ($\sim$1 at.%) and a minor amount of oxygen ($\sim$10 at.%) on the surface. The presence of these two elements can be attributed to contamination during fabrication or handling. An approximate percentage of 10 at.% oxygen was also observed on DLC samples prepared by the PEVCD method in the literature[17].

Different carbon bond states and their corresponding percentages were determined by performing deconvolution of the C 1s peaks on high resolution XPS spectra. All samples contain a major C 1s contribution at the 284.6 eV position, which was assigned as the C-C (or C-H) sp2 from vapor oil which can be used

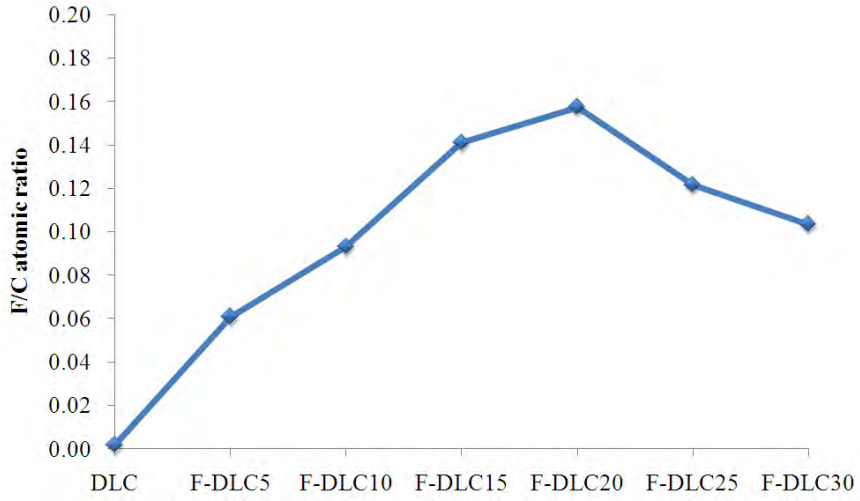

Figure 6.3: F/C atomic ratio changes with the CF_4 gas flow rate.

for energy scale calibration. The peak fitting results for samples DLC, F-DLC10, and F-DLC20 are shown in Fig. 6.4 and major carbon bond percentages for five samples are shown in Table 6.2. The C1s spectrum of the DLC coating can be deconvoluted into six Gaussian peaks corresponding to C-C sp2 (284.6 eV), C-COO (285.1 eV), C-C sp3 (285.5 eV), C-O (286.6 eV), C=O (287.8 eV), and COO (289.0 eV). Similarly, the C1s spectrum of the F-DLC coatings can be deconvoluted into five peaks corresponding to C-C sp2, C-C sp3, C-O, C-CF (287.0 eV), and C-F (289.0 eV). The percentages of $-CF_2$ and $-CF_3$ bonding states were either negligible or non-existent, since nearly no intensities were observed in the C1s spectra for all F-DLC coatings in the corresponding ranges of 290.3-292 eV and 292.6-294 eV, as previously reported [18]. Among these F-DLC samples, the highest fluorine content was obtained at 14.0 at.% on F-DLC20, less than a reported 20.7 at.% or higher where $-CF_2$ bond exists in F-DLC coatings fabricated by RF PECVD [12].

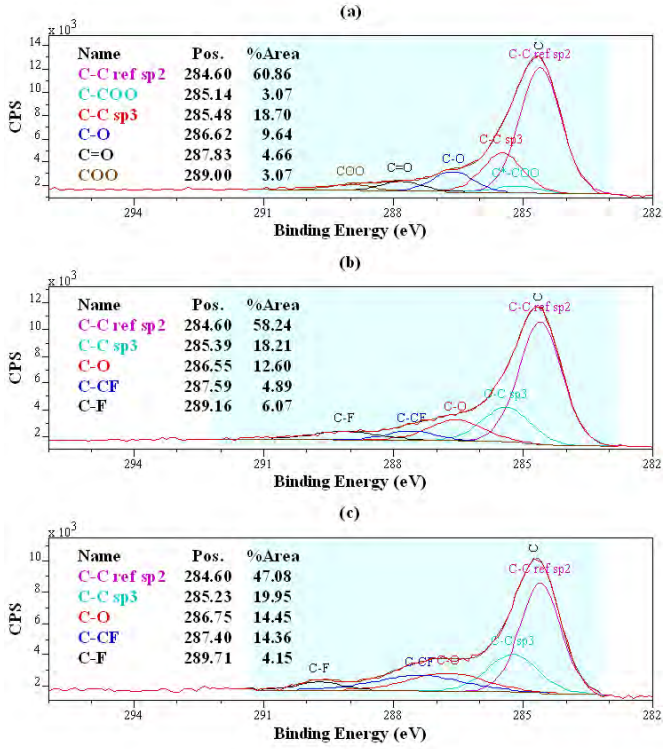

Figure 6.4: Deconvolution of C1s peaks for (a) DLC (b) F-DLC10, and (c) F-DLC20.

Table 6.2: Percentages of major carbon bond states.

Sample	C-C & C=C	C-O	C-CF	C-F
DLC	79.5	9.7	0	0
F-DLC5	80.1	10.2	6.4	3.2
F-DLC10	76.5	12.6	4.9	6.1
F-DLC15	68.8	9.5	14.0	7.8
F-DLC20	70.1	17.5	8.1	4.3
F-DLC25	70.4	9.3	13.5	6.8
F-DLC30	71.5	10.8	12.2	5.6

In the DLC coating, the C-O bond dominated among all the bond species formed between carbon and oxygen atoms. In F-DLC samples, the percentages

of C-CF and C-F bonds generally increased in the CF_4 flow rate range 0–20 sccm. While in the same flow rate range, the combined percentage of C-C sp2 and sp3 dropped approximately from 80% to 70% (Fig. 6.5).

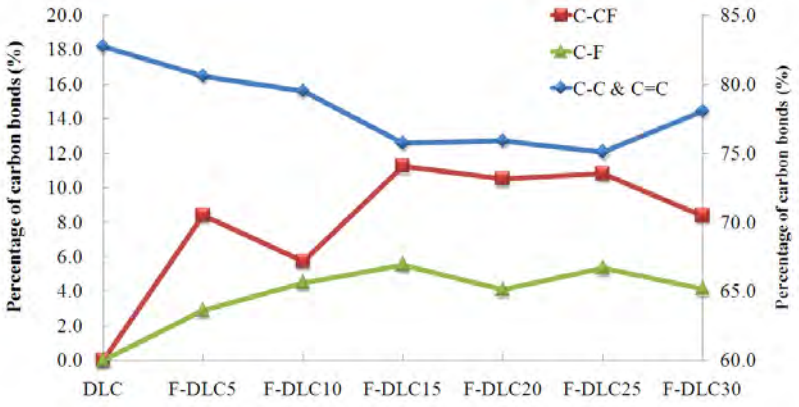

Figure 6.5: Carbon bond species and their percentages with different F/C atomic ratios: right vertical axis for C-CF and C-F bonds, left vertical axis for C-C and C=C.

6.3.2 Water contact angle measurements

Greater water contact angles were obtained on all F-DLC coatings than on the fluorine-free DLC coating (Fig. 6.6). A trend of contact angle versus gas flow rate was found to be similar to that of the fluorine-to-carbon (F/C) atomic ratio (Fig. 6.3): the contact angle increased from 73.8±1.9° to 87.6±0.6° when the CF_4 flow rate changed gradually from 0 to 20 sccm, and then declined steadily to approximately 84° under further increase of gas flow rate to 25 and 30 sccm. The presence and quantity of C-F bonds on the F-DLC surface probably contributed to lowering the surface energy and increasing the water contact angle.

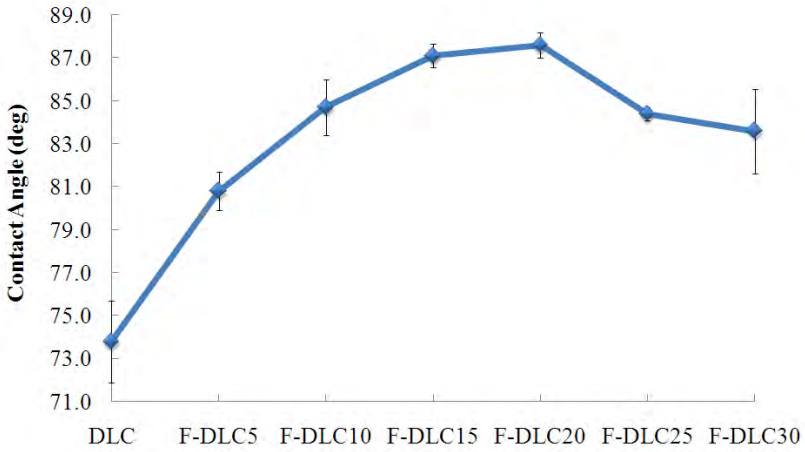

Figure 6.6: Contact angles measured on DLC and F-DLC coatings.

6.3.3 Surface morphology

AFM scanning was performed on DLC and F-DLC samples, to relate the surface morphology to the wetting properties. The representative line scans, 2D and 3D images of DLC and F-DLC10 coatings are shown in Fig. 6.7. In contrast with F-DLC10, the DLC sample had larger irregular particles on the surface, with a typical height range of 72–90 nm. Root mean square (RMS) roughness values were determined over 50×50 μm^2 and 20×20 μm^2 AFM images. The DLC sample also had a much greater RMS (85.0 nm at the 50×50 μm^2 observation scale) than these of F-DLC samples (7–32 nm in Table 6.3). There is no direct relationship between RMS and F/C atomic ratio for F-DLC coatings. RMS roughness of about 30 nm was obtained for F-DLC5 and F-DLC25, 16.2 nm for F-DLC15, and nearly 10 nm for F-DLC10 and F-DLC30. Smallest RMS roughness is observed on F-DLC20 (3.0 nm). Given the relatively flat F-DLC surfaces indicated by measured RMS and roughness average values, the other critical factor for wetting property besides surface roughness, the surface energy, is more likely to follow

closely the trend of contact angles. Even though smaller roughness values were obtained than the 50×50 μm^2 scale, a similar relationship between DLC and F-DLC coatings was observed for RMS values at the 20×20 μm^2 scale.

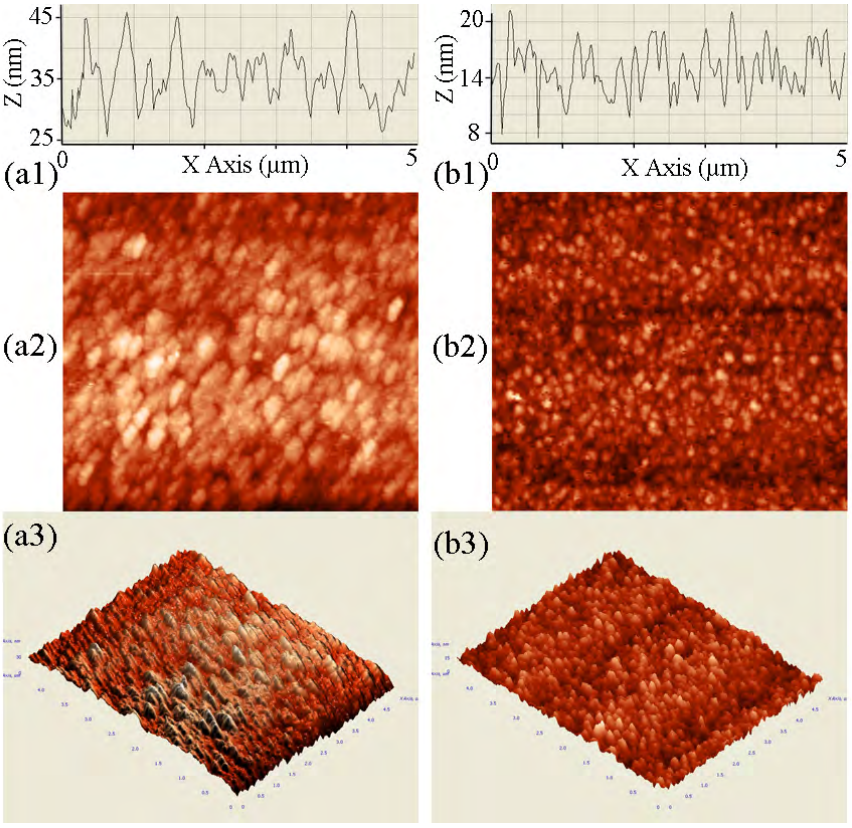

Figure 6.7: Line profiles, 2D and 3D AFM micrographs for (a) DLC and (b) F-DLC10.

6.3.4 Nanoindentation studies

The DLC sample had a hardness of 23.5±1.3 GPa, which was between the reported 80 GPa for tetrahedral amorphous carbon (ta-C) and 10–20 GPa for amorphous carbon (a-C) and hydrogenated alloys (a-C:H) [2]. The DLC sample is likely to have the amorphous structure and this is consistent with other

Table 6.3: Surface roughness analysis of DLC and F-DLC coatings.

Sample	50×50 μm^2		20×20 μm^2		5×5 μm^2	
	RMS (nm)	Roughness average (nm)	RMS (nm)	Roughness average (nm)	RMS (nm)	Roughness average (nm)
DLC	47.5	37.2	28.7	24.4	7.6	5.7
F-DLC5	27.4	23.2	8.1	6.0	3.7	2.7
F-DLC10	33.9	25.4	17.6	13.9	6.2	4.8
F-DLC15	16.2	13.7	8.8	5.3	3.9	2.9
F-DLC20	23.4	19.3	15.2	7.2	3.0	2.4
F-DLC25	30.8	26.1	12.3	10.0	4.2	3.3
F-DLC30	32.0	22.6	6.9	4.9	5.7	4.6

findings in this paper, such as 88.2 at.% for the carbon content, 60.9% and 18.7% for C-C sp^2 and sp^3 bonding species percentages, respectively. With additional fluorine elements incorporated into the coatings, hardness values declined when the CF_4 flow rate was increased from 5 to 30 sccm. However, as seen for several other variables reported in this study, differences between 20, 25 and 30 sccm treatments were relatively small. Even though there is a minor content of oxygen on the surface for all DLC and F-DLC samples (∼10 at.%), the surface hardness as a function of CF_4 flow rate should remain the same trend. The integration of fluorine into an amorphous carbon structure probably disrupted the cross-linked diamond structure and thus the C-C sp^3 bonding, as well as reducing surface hardness [6].

Young's modulus values for the DLC and F-DLC coatings also had an inverse relationship with CF_4 flow rate (or the actual fluorine content) in the range of 0–20 sccm with only small difference in the range 20–30 sccm. From DLC to F-DLC5, the fluorine content increases from 0 to 4.8 at.%, and the Young's modulus drops distinctly from 236±9 to 202±6 GPa. For F-DLC30, the Young's modulus

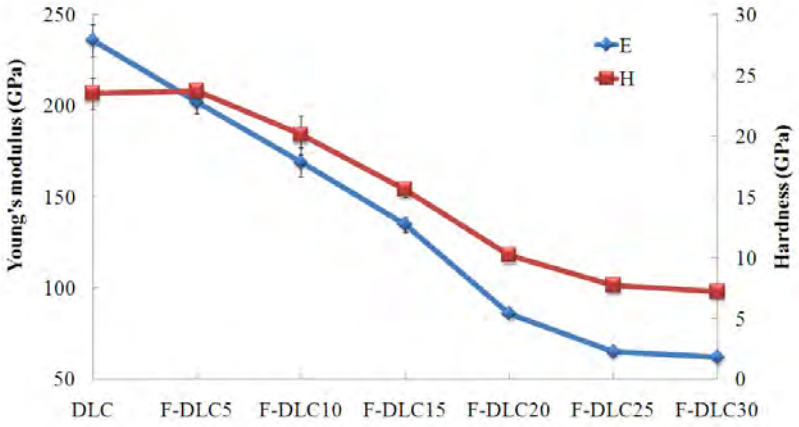

Figure 6.8: Young's modulus and hardness of DLC and F-DLC coatings.

drops significantly to 62±1 GPa. Along with the experimental results, DLC is harder and stiffer than F-DLC coatings fabricated using the CFUBMS method in this research.

6.3.5 Finite Element Analysis

Typical load-displacement curves were obtained by performing nanoindentation experiments on DLC, F-DLC samples, and steel (Fig. 6.9). The experimental values of elastic modulus (E) and hardness (H) of these samples, derived by fitting the data, are presented in Fig. 6.10a. Different elastic modulus and the hardness of the pure DLC coating have been reported, due to variations in deposition and processing method. Results obtained in this research are in general agreement with those depicted in the literature [19, 20].

At the highest CF_4 flow rate (30 sccm), the Youngs modulus and the hardness dropped to only 26% and 30% of those for the DLC sample, respectively. Clearly, addition of CF_4 gas during the fabrication stage resulted in a decrease

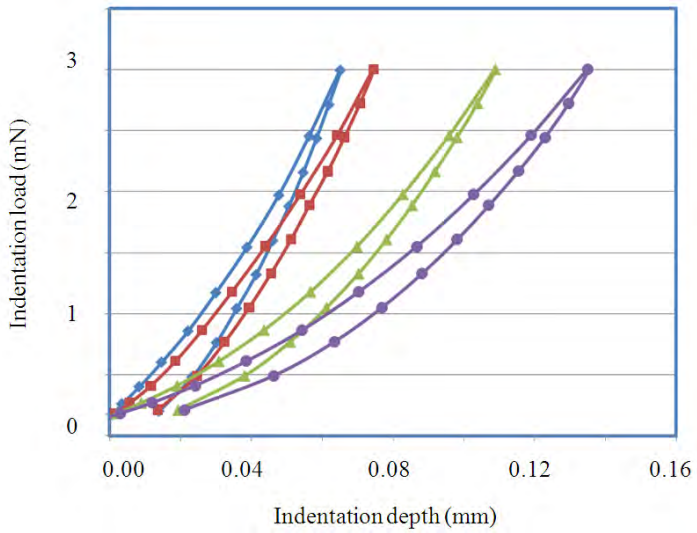

Figure 6.9: Load-displacement curves for DLC and F-DLC samples obtained from nanoindentation experiments.

in both the Youngs modulus and the hardness on the F-DLC coatings, although the relationship is non-linear, with the fastest change occurred at the intermediate range (10–20 sccm). However, for the sample F-DLC10 with a relatively high contact angle (84.7±1.3°), there is only marginal decrease in the hardness (<15%) compared to that of the DLC. Therefore, the sample F-DLC10 gives a combination of considerable hydrophobic property and hardness.

Previous studies show that the hardness to modulus ratio, H/E, is an important parameter for predicting wear resistance [21]. Generally, the higher this ratio, the better the wear resistance of the coating. With the highest H/E ratio value clearly shown in Fig. 6.10b, F-DLC10 is expected to have the best wear resistance among all the study samples. In addition, coatings with a high hardness and a low elastic modulus, and therefore a high plastic resistance ratio H^3/E^2, are more likely to resist plastic deformation under low loadings and hence exhibit

a higher yield strength [22, 23]. As such, the sample F-DLC10 outperforms the DLC coating in this respect (Fig. 6.10c).

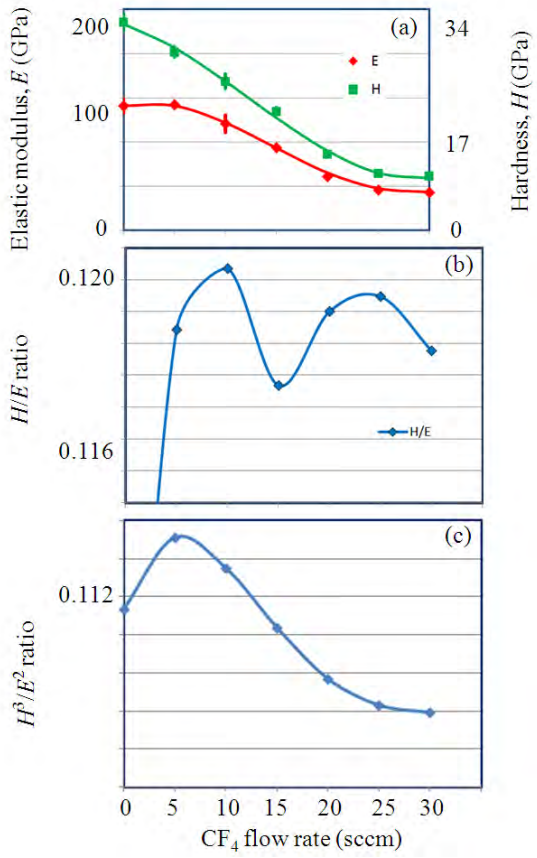

Figure 6.10: Mechanical properties of the coatings derived from the nanoindentation tests, (a) elastic modulus and hardness, (b) H/E, and (c) H^3/E^2.

The mechanical parameters obtained from the nanoindentation results (Table 6.4) were adopted for FEM analysis. The modelling results for the tensile and von Mises stress for DLC and F-DLC10 are presented in Fig. 6.11. The higher stress, as well as the associated plastic zone, was primarily concentrated within the coating layer. Notably, plastic deformation appeared first in the DLC coating and was located within two regions. The first one was at the interface between

the coating and the substrate, at an indentation depth of 0.2 μm, and was caused by excessive radial tensile stress (Fig. 6.11b). The second plastic region appeared immediately below the indenter, and resulted from excessive von Mises stress at a smaller indentation depth of 0.06 μm (Fig. 6.11d). At the same indentation depth, the stress levels in these two regions were lower in F-DLC10, as no plastic deformation was observed (Fig. 6.11a and c).

Table 6.4: Mechanical properties of DLC and F-DLC coatings (obtained from nanoindentation experiments), and steel.

Sample	CF_4 (sccm)	Youngs modulus (GPa)	Hardness (GPa)	H/E	H^3/E^2
DLC	0	236	23.5	0.0996	0.2330
F-DLC5	5	202	23.7	0.1173	0.3262
F-DLC10	10	169	20.1	0.1189	0.2843
F-DLC15	15	135	15.6	0.1156	0.2083
F-DLC20	20	86	10.2	0.1186	0.1435
F-DLC25	25	65	7.7	0.1185	0.1081
F-DLC30	30	62	7.2	0.1161	0.0971
stainless steel	-	180	30	0.1667	0.8333

The two coatings, in terms of the size of the plastic zone is compared for the two coatings in Fig. 6.12, which was obtained through subdomain integration of the FEM results. Even using the conservatively estimated yield strength from $\sigma_y \sim H/3$ [24], which might underestimate the variable for the 10 sccm CF_4 sample (see the discussion relating to Fig. 6.10c), there was still a significant decrease in the volume of plastic zone in this coating. Generally speaking, for the same indentation depth, in the 10 sccm CF_4 sample the plastic zone resulted from the radial tensile stress was reduced by ~35%, and that resulted from the von Mises stress was reduced by ~25%, compared to those in the pure DLC coatings,

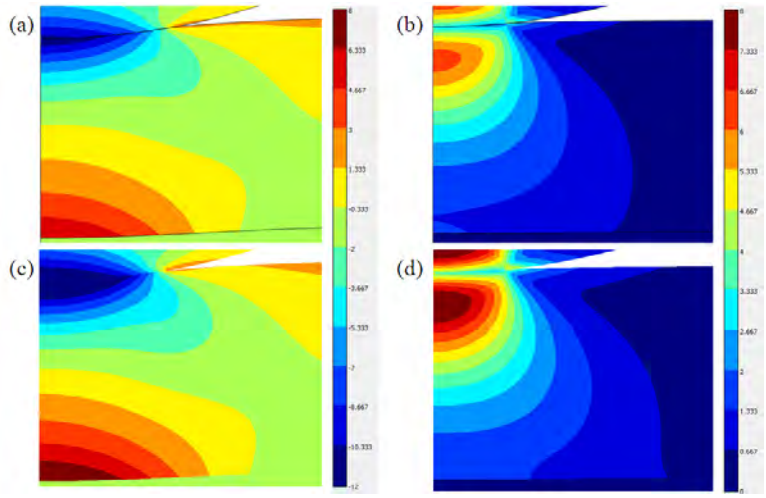

Figure 6.11: Stress distribution within the coatings, obtained from FEM simulations: (a) radial stress σ_r in F-DLC10, indentation depth 0.2 μm, (b) radial stress σ_y in the DLF coating, indentation depth 0.2 μm, (c) von Mises stress σ_{vm} in F-DLC10, indentation depth 0.06 μm, and (d) von Mises stress σ_{vm} in the DLC coating, indentation depth 0.06 μm. Plastic deformation will occur in the DLC coating ((b) and (d)) due to excessive stress level, but not in F-DLC10.

respectively. Subsequently, F-DLC10 shows a better damage tolerance than the DLC coating.

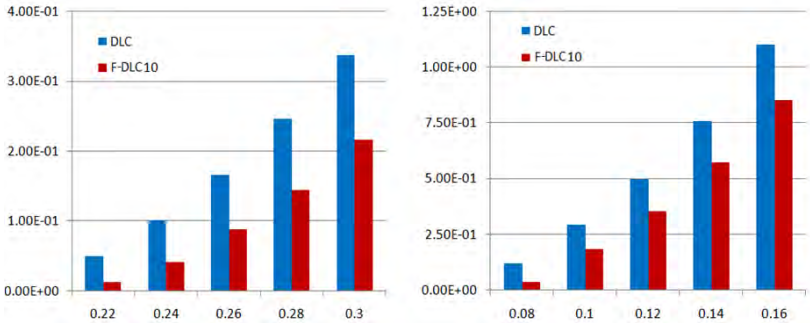

Figure 6.12: The size of the plastic zones in the DCL and F-DLC10 coatings as a function of indentation depth, resulted from (a) radial tensile stress, and (b) von Mises stress.

6.4 Conclusions

DLC and F-DLC coatings with different fluorine contents were successfully fabricated by adjusting the CF_4 flow rate during the CFUBMS deposition procedure. The fluorine content and C-F bond percentages on the coating surface were increased with escalating CF_4 flow rate. Smoother surfaces, revealed by smaller RMS and roughness average values, were obtained on F-DLC coatings than on the DLC sample. Incremental incorporation of fluorine into DLC samples also led to a noticeable increase in water contact angle and a substantial decrease in both Youngs modulus and hardness. The mechanical properties of F-DLC10 sample were studied by nanoindentation and FEM. While there is a slight decrease in the Youngs modulus and hardness compared to the DLC sample, its H/E value, and hence the wear resistance, is the best amongst all samples studied. F-DLC10 also has a better damage tolerance than the DLC sample. As such, the properties of this particular sample, including relatively high contact angle and strong mechanical properties, make it well suited for hydrophobic applications such as in surgical tools.

References

[1] Alfred Grill. Diamond-like carbon: state of the art. *Diamond and Related Materials*, 8(2–5):428–434, 1999. 141

[2] J. Robertson. Diamond-like amorphous carbon. *Materials Science and Engineering: R: Reports*, 37:129–281, 2002. 141, 142, 154

[3] Jung-Gu Kim, Kwang-Ryeol Lee, and Seok-Jo Yang. Wear-corrosion perfor-

mance of Si-DLC coatings on Ti-6Al-4V substrate. *Journal of Biomedical Materials Research Part A*, 86A(1):41–47, 2008. 141

[4] T. Saito, T. Hasebe, S. Yohena, Y. Matsuoka, A. Kamijo, K. Takahashi, and T. Suzuki. Antithrombogenicity of fluorinated diamond-like carbon films. *Diamond and Related Materials*, 14(3):1116–1119, 2005. 142

[5] C.H. Kwok, Jin Wang, and Paul K. Chu. Surface energy, wettability, and blood compatibility phosphorus doped diamond-like carbon films. *Diamond and Related Materials*, 14(1):78–85, 2005. 141

[6] Fatih G. Sen, Yue Qi, and Ahmet T. Alpas. Surface stability and electronic structure of hydrogen- and fluorine-terminated diamond surfaces: A first-principles investigation. *Journal of Materials Research*, 24:2461–2470, 7 2009. 142, 155

[7] C. Donnet, J. Fontaine, A. Grill, V. Patel, C. Jahnes, and M. Belin. Wear-resistant fluorinated diamondlike carbon films. *Surface and Coatings Technology*, 94–95(0):531–536, 1997. 142

[8] M. Hakovirta, X. M. He, and M. Nastasi. Optical properties of fluorinated diamond-like carbon films produced by pulsed glow discharge plasma immersion ion processing. *Journal of Applied Physics*, 88(3):1456–1459, 2000.

[9] C. Donnet. Recent progress on the tribology of doped diamond-like and carbon alloy coatings: a review. *Surface and Coatings Technology*, 100–101 (0):180–186, 1998. 142

[10] Terumitsu Hasebe, Satoshi Yohena, Aki Kamijo, Yuko Okazaki, Atsushi

Hotta, Koki Takahashi, and Tetsuya Suzuki. Fluorine doping into diamond-like carbon coatings inhibits protein adsorption and platelet activation. *Journal of Biomedical Materials Research Part A*, 83A(4):1192–1199, 2007. 142

[11] F.R. Marciano, D.A. Lima-Oliveira, N.S. Da-Silva, E.J. Corat, and V.J. Trava-Airoldi. Antibacterial activity of fluorinated diamond-like carbon films produced by PECVD. *Surface and Coatings Technology*, 204(18–19):2986–2990, 2010. 142

[12] X.J. Su, Qi Zhao, Su Wang, and A. Bendavid. Modification of diamond-like carbon coatings with fluorine to reduce biofouling adhesion. *Surface and Coatings Technology*, 204(15):2454–2458, 2010. 142, 150

[13] P.J Kelly and R.D Arnell. Magnetron sputtering: a review of recent developments and applications. *Vacuum*, 56(3):159–172, 2000. 142

[14] W.C. Oliver and G.M. Pharr. Measurement of hardness and elastic modulus by instrumented indentation: Advances in understanding and refinements to methodology. *Journal of Materials Research*, 19:3–20, 1 2004. 146

[15] Xiaoli Zhao, Zonghan Xie, and Paul Munroe. Nanoindentation of hard multilayer coatings: Finite element modelling. *Materials Science and Engineering: A*, 528(3):1111–1116, 2011. 147

[16] P.C. Wo, X.L. Zhao, P.R. Munroe, Z.F. Zhou, K.Y. Li, D. Habibi, and Z.H. Xie. Extremely hard, damage-tolerant ceramic coatings with functionally graded, periodically varying architecture. *Acta Materialia*, 61(1):193–204, 2013. 147

[17] Antonia Terriza, Rafael Alvarez, Ana Borras, Jose Cotrino, Francisco Yubero, and Agustin R. Gonzalez-Elipe. Roughness assessment and wetting behavior of fluorocarbon surfaces. *Journal of Colloid and Interface Science*, 376(1):274–282, 2012. 149

[18] K. P. Huang, P. Lin, and H. C. Shih. Structures and properties of fluorinated amorphous carbon films. *Journal of Applied Physics*, 96(1):354–360, 2004. 150

[19] Z.-H. Xie, R. Singh, A. Bendavid, P.J. Martin, P.R. Munroe, and M. Hoffman. Contact damage evolution in a diamond-like carbon (DLC) coating on a stainless steel substrate. *Thin Solid Films*, 515(6):3196–3201, 2007. 156

[20] Liang-Yih Chen and Franklin Chau-Nan Hong. Diamond-like carbon nanocomposite films. *Applied Physics Letters*, 82(20):3526–3528, 2003. 156

[21] A Leyland and A Matthews. On the significance of the H/E ratio in wear control: a nanocomposite coating approach to optimised tribological behaviour. *Wear*, 246(1–2):1–11, 2000. 157

[22] J. Musil. Hard and superhard nanocomposite coatings. *Surface and Coatings Technology*, 125(1–3):322–330, 2000. 158

[23] M.E. Roy, L.A. Whiteside, J. Xu, and B.J. Katerberg. Diamond-like carbon coatings enhance the hardness and resilience of bearing surfaces for use in joint arthroplasty. *Acta Biomaterialia*, 6(4):1619–1624, 2010. 158

[24] Brian R. Lawn and Robert F. Cook. Probing material properties with sharp

indenters: a retrospective. *Journal of Materials Science*, 47(1):1–22, 2012. 159

Chapter 7

Wetting and mechanical properties of fluorinated and fluorine-free diamond-like carbon coatings

7.1 Introduction

In the previous chapter, fluorinated diamond-like carbon (F-DLC) coatings were fabricated using the closed-field unbalanced magnetron sputtering (CFUBMS) method with varying CF_4 gas flow rates. In this chapter, two groups of DLC samples were discussed: DLC deposited with the presence of varying C_2H_2 flow rate and DLC-F fabricated with the presence of both varying CF_4 gas flow rates and a fixed C_2H_2 flow rate. The surface chemistry, morphology and mechanical properties are compared here.

7. WETTING AND MECHANICAL PROPERTIES OF FLUORINATED AND FLUORINE-FREE DIAMOND-LIKE CARBON COATINGS

In regard to the tribological properties of a protective coating, the optimum hardness (H) and elastic modulus (E) values are always the objective to achieve. While hardness is widely held as an important factor, other parameters, such as the hardness-to-modulus ratio (H/E), plasticity index and the expression H^3/E^2, also play a critical role in the material's toughness [1]. H/E is an indicator for the gap between energy dissipation by elastic and plastic deformation in the indentation contact [2]. Higher H/E values can help the coating sustain high critical loads for the elastic/plastic transition. In addition, a higher H/E value leads to in a lower plasticity index and a more elastic contact [1]. For hard elastic coatings, immediate recovery occurs in indentation and the plasticity is minimised. The plasticity index is the ratio of plastic work done to total work done [3].

Overcoat films are generally assumed to be resistant to plastic strain during contact and coating cracking is observed to be directly involved with plastic deformation [4]. The load required for the initiation of plastic deformation, P_y, can be related to the radius r of a rigid sphere that is in contact with an elastic/plastic half-space by the following equation [5]

$$P_y = 0.78 r^2 \frac{H^3}{E^2} \tag{7.1}$$

A high contact load will be needed for plastic deformation on a film with a high value of H^3/E^2. Therefore, this value can be used to quantify the resistance of a coating to plastic deformation.

The H/E and H^3/E^2 values for these DLC and DLC-F samples are also compared to find a hard elastic coating that is suitable for the purpose of mechanical

protection.

Statistical roughness measurements, i.e. root mean square roughness (R_{rms})and roughness average (R_a), are obtained from AFM scans and generally used to characterize surface roughness. R_{rms} is defined as the square root of the summation of squared vertical deviations divided by the number of data points minus 1.

$$R_{rms} = \sqrt{\frac{\sum_{i=1}^{n}(Z_i - \bar{Z})^2}{n-1}} \tag{7.2}$$

where Z_i is the vertical height of each sampled data point, and $\bar{Z}$ is the average vertical height of the sampled surface. Therefore, R_{rms} really represents the standard deviation of the surface height from its height average. R_a is the arithmetic average of vertical deviations and can be expressed as

$$R_a = \frac{\sum_{i=1}^{n}|Z_i - \bar{Z}|}{n} \tag{7.3}$$

7.2 Experimental details

Fabrication of DLC coatings, contact angle measurements, surface characterization, mechanical tests and other experimental details can refer to the previous chapter.

The DLC samples deposited with the presence of varying C_2H_2 flow rate were denoted based on the flow rate. This series includes five samples: DLC5, DLC10, DLC20, DLC25 and DLC30.

The DLC-F fabricated with the presence of both varying CF_4 gas flow rates

and a fixed C_2H_2 flow rate of 10 sccm were donted in a similar way (based on the CF_4 flow rate). This series includes five samples as well: DLC-F5, DLC-F10, DLC-F15, DLC-F20 and DLC-F25.

7.3 Results and discussion

7.3.1 Surface chemical composition

Elements presented in the surfaces of DLC and DLC-F samples were identified as C, N, O, and F, based on their corresponding 1s peak binding energies at 284.6, 399.3, 532.3, 687.3 eV.

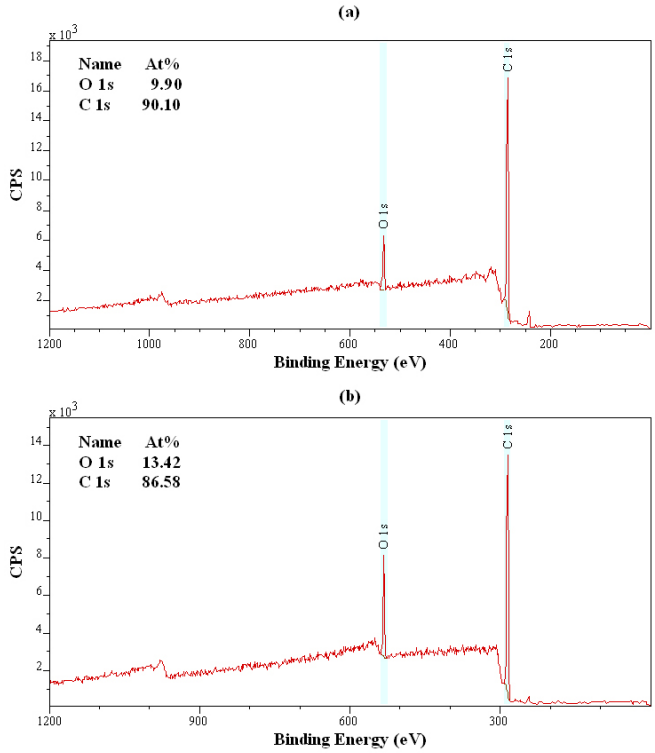

Figure 7.1: XPS survey scans for two DLC samples: (a) DLC5 and (b) DLC20.

Carbon and oxygen were found as the major elements on five DLC samples from their XPS spectra, with approximately 90% and 10% atomic percentages, respectively (Table 7.1). There is, therefore, no clear relationship between atomic percentage and C_2H_2 flow rate. The incorporation of oxygen into the DLC samples can be attributed to contamination during fabrication or contact with air.

Table 7.1: Atomic percentages and bond species for DLC samples fabricated at different C_2H_2 flow rates.

Sample	C1s (at.%)	O1s (at.%)	C=C (%)	C-C (%)	C-O (%)	C=O (%)
DLC5	90.1	9.9	57.2	34.2	3.9	4.7
DLC10	92.1	7.9	65.6	22.9	7.5	4.0
DLC20	86.6	13.4	81.3	10.9	6.5	1.4
DLC25	90.2	9.8	82.9	9.5	3.7	3.9
DLC30	90.8	9.2	72.6	13.1	10.4	3.9

Four carbon bond species were found on these five DLC samples by resolving their XPS C1s spectra, namely C=C sp2 at 284.60 eV calibrated as the binding energy reference, C-C sp3 at around 285.3 eV, C-O bond at about 286.4 eV, and C=O bond at approximately 287.8 eV (Fig. 7.2). The C=C sp2 bond percentage increases with the C_2H_2 flow rate from 57.2% to 82.9% when the rate reaches 25 sccm, and then drops to 72.6% at 30 sccm C_2H_2 flow rate. The C-C sp3 bond percentage has a reverse trend to the C=C sp2 bond percentage (Fig. 7.3). The data indicate that the sample DLC25 is possibly a turning point, in regard to the C=C sp2 and C-C sp3 bond percentages, for this series of samples fabricated with varying C_2H_2 flow rates, even though no further data have been acquired for C_2H_2 flow rates greater than 30 sccm. Similar to the atomic percentages presented in Table 7.1, there were no clear trends for C-O and C=O bond percentages.

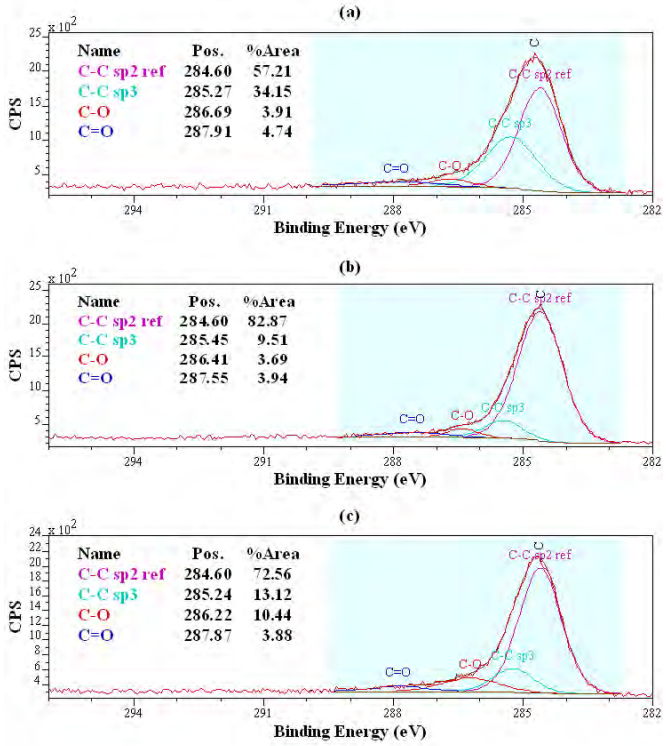

Figure 7.2: Carbon bond species for three DLC samples: (a) DLC5, (b) DLC25 and (c) DLC30.

As for DLC-F samples, carbon, oxygen and fluorine elements appear distinctly on each XPS spectrum (Fig. 7.4). In the meanwhile, with a CF_4 flow rate increasing from 5 to 25 sccm and a C_2H_2 flow rate fixed at 10 sccm during deposition, carbon atomic percentage declines from 86.9 at.% to 80.4 at.% and fluorine atomic percentage increases from 2.1 at.% to 9.4 at.% (Table 7.2). Oxygen atomic percentage remained nearly the same, at about 11.0 at.%. The F/C atomic ratio increased steadily from 0.02 for DLC-F5 to 0.12 for DLC-F25 (Fig. 7.5).

Compared to DLC5-30 samples, DLC-F5-25 samples contain the same C=C sp2, C-C sp3, and C-O bonds, but not the C=O bond. In addition, C-F and

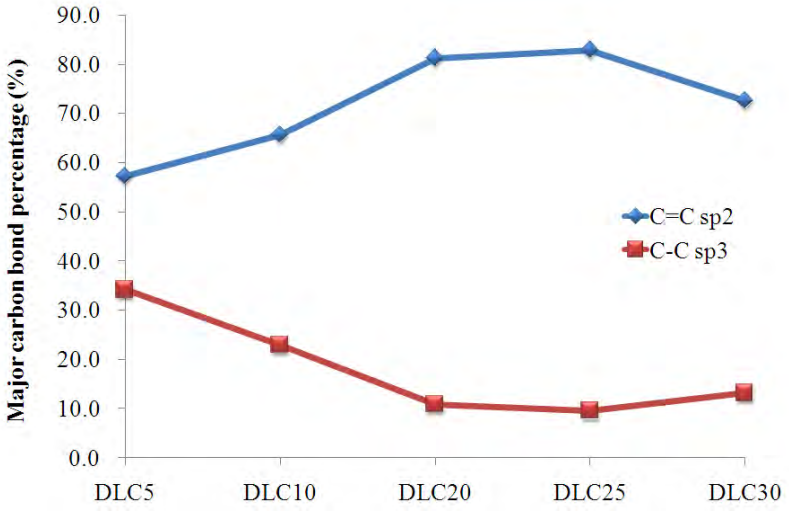

Figure 7.3: Carbon bond percentages for C=C sp2 and C-C sp3 in five DLC samples.

Table 7.2: Atomic percentages and F/C ratios for DLC-F samples.

Sample	C1s (at.%)	O1s (at.%)	F1s (at.%)	F/C
DLC-F5	86.9	11.0	2.1	0.02
DLC-F10	86.3	11.0	2.8	0.03
DLC-F15	83.8	12.0	4.2	0.05
DLC-F20	82.3	12.2	5.5	0.07
DLC-F25	80.4	10.3	9.4	0.12

C-CF bonds appeared on the XPS C1s spectra (Fig. 7.6).

The percentages of carbon bond components, as shown in Table 7.3, all have turning points versus the increasing CF_4 flow rate from 5 to 25 sccm. The percentage of C=C sp2 and C-C sp3 bonds combined, declined from 84.5% to 73.0% on DLC-F20, and then rose to 77.2% on DLC-F25. The percentages for C-O and C-CF bonds have an opposite trend. They both increased steadily to the peak results on DLC-F20, and then dropped on DLC-F25. A trend is also found on the

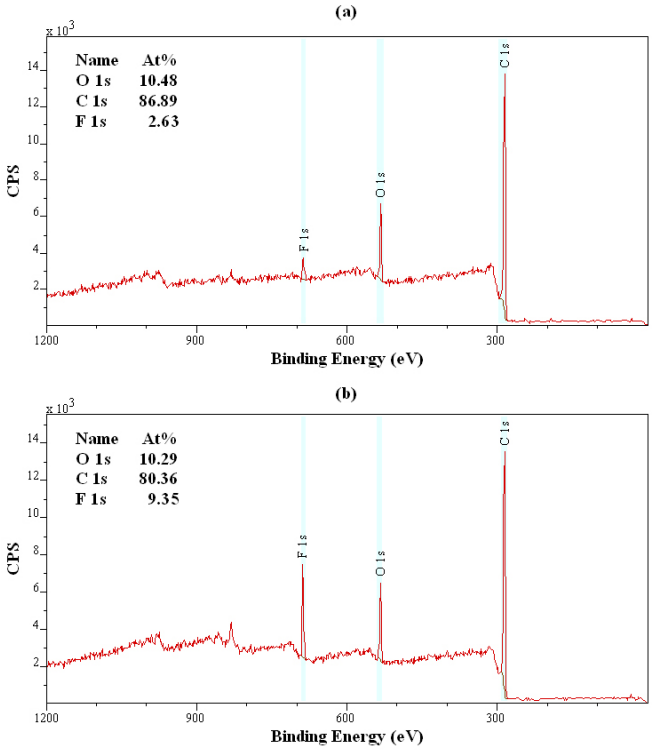

Figure 7.4: XPS survey scans for two DLC-F samples: (a) DLC-F10 and (b) DLC-F25.

Table 7.3: Percentages of major carbon bond states.

Sample	C=C & C-C (%)	C-O (%)	C-CF (%)	C-F (%)
DLC-F5	84.5	6.1	4.5	4.8
DLC-F10	83.2	6.8	5.5	4.4
DLC-F15	75.0	11.1	7.2	6.8
DLC-F20	73.0	14.2	7.3	5.5
DLC-F25	77.2	11.9	6.7	4.1

percentage of C-F bond, similar to that of C-O and C-CF bonds, even though a slightly higher result (4.8%) was found on DLC-F5 than on DLC-F10 (4.4%), and the peak result (6.8%) was found on the sample DLC-F15 instead on DLC-F20.

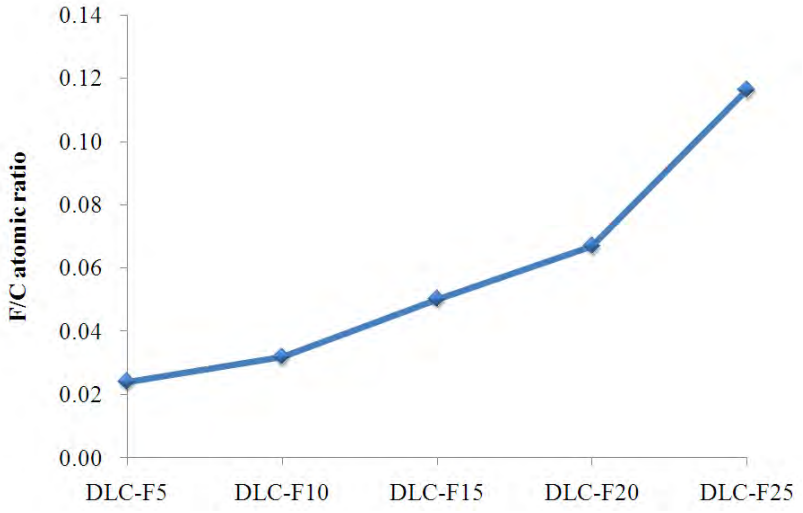

Figure 7.5: F/C atomic ratio changes with the CF_4 gas flow rate.

7.3.2 Water contact angle measurements

Water contact angles declined steadily with the C_2H_2 flow rate increasing from 5 to 30 sccm during DLC coating fabrication (Fig. 7.8). Highest WCA was obtained on DLC5 as 85.6±0.3°. From DLC5 to DLC30, the WCA dropped about 5.5°.

As for DLC-F samples, highest WCA was obtained on DLC-F5 as 85.7±0.3°. From DLC-F10 to DLC-F25, the WCA increased slowly from 82.1±1.2° to 83.1±0.5°. Compared to the F/C atomic ratio change (Fig. 7.5), there is only a slight increase on the WCA value for these DLC-F coatings.

7.3.3 Surface morphology

Fig. 7.10 reveals two different surface topographies on DLC samples: pebble-like and granule-like. The pebble-like topography was only observed on DLC10, and the granule-like topography was found on other four DLC samples. There is no explicit explanation, however, to describe the formation mechanisms for these

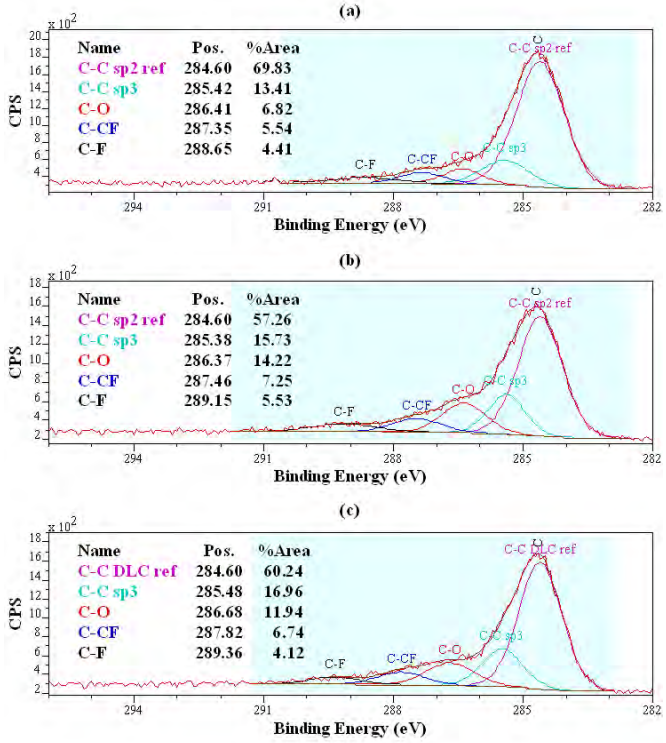

Figure 7.6: Carbon bond species for three DLC-F samples: (a) DLC-F10 (b) DLC-F20 and (c) DLC-F25.

two topographies, with current data acquired.

Root mean square (RMS) and roughness average values were determined over AFM images scanned in 50×50 μm^2, 20×20 μm^2 and 5×5 μm^2 observation scales and presented in Table 7.4. Evident difference was observed on different scales, especially between 50×50 μm^2 and either of the other two scales: higher roughness values were obtained on 50×50 μm^2 than smaller scales. It is spontaneous that different values are acquired in varying scales, and therefore roughness is influenced by scanning scale. However, most roughness values obtained on 20×20 μm^2 and 5×5 μm^2 scan scales are similar. It indicates that in a reasonably scale size ($\sim$ 20×20 μm^2), roughness values reach a saturation and therefore relatively

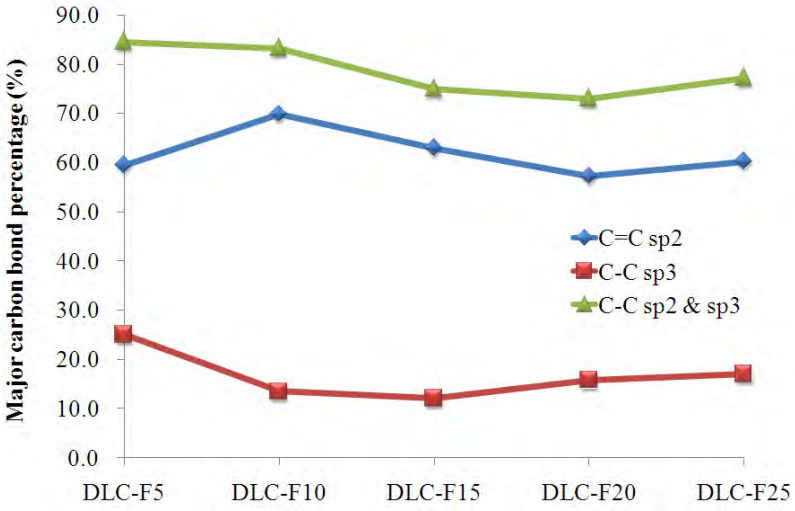

Figure 7.7: Carbon bond percentages for C=C sp2 and C-C sp3 in five DLC-F samples.

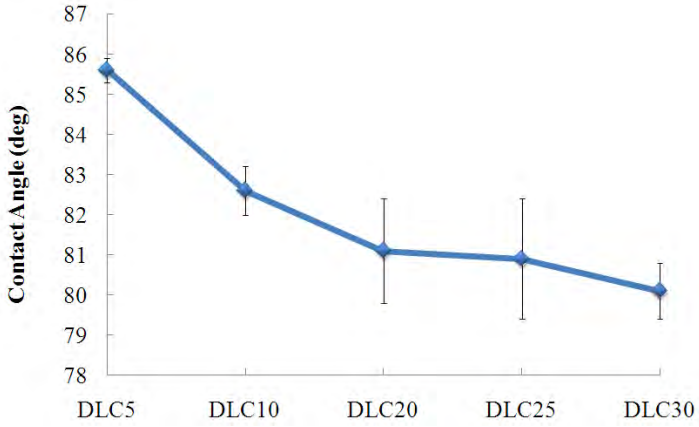

Figure 7.8: Contact angles measured on five DLC coatings.

reliable for roughness characterization.

In this series, lowest RMS and roughness average values were observed on DLC25 as 4.2 nm and 3.4 nm, respectively. Highest roughness values were obtained on DLC30 to be 5.7 nm and 4.6 nm. The roughness values of other DLC samples spread between these two narrow ranges (4.2–5.7 nm and 3.4–4.6 nm).

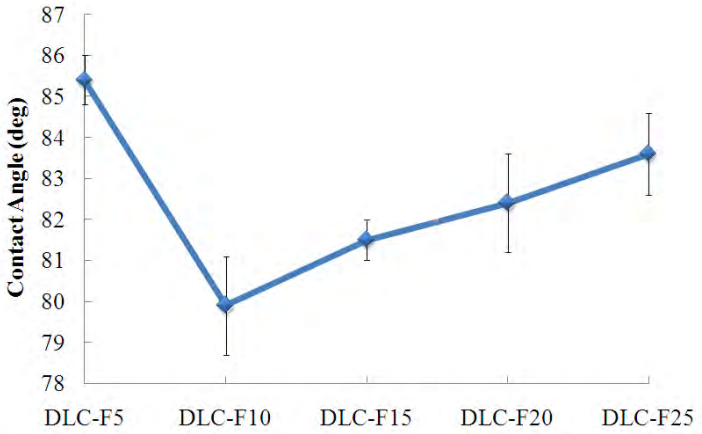

Figure 7.9: Contact angles measured on five DLC-F coatings.

Table 7.4: Surface roughness analysis of DLC5-30 coatings.

Sample	50×50 μm^2		20×20 μm^2		5×5 μm^2	
	RMS (nm)	Roughness average (nm)	RMS (nm)	Roughness average (nm)	RMS (nm)	Roughness average (nm)
DLC5	7.4	6.0	4.4	3.7	4.1	3.1
DLC10	9.8	7.9	5.6	3.9	3.9	3.1
DLC20	17.1	13.9	5.2	4.1	5.9	4.7
DLC25	9.2	7.6	4.2	3.4	2.7	2.2
DLC30	11.4	9.2	5.7	4.6	6.6	5.2

Higher C_2H_2 flow rates during coating deposition are likely to increase the surface roughness of DLC coatings.

The roughness values for DLC-F samples obtained in three scan scales are shown in Table 7.5. Based on previous discussion in regard to AFM observation scales and due to the same reason, the roughness values obtained in the 20×20 μm^2 scale were adopted for surface characterization. Highest roughness values were obtained on DLC25 to be 7.6 nm and 5.4 nm. Other four DLC-F samples have similar RMS (5.2–6.0 nm) and roughness average (4.2–4.7 nm). With a

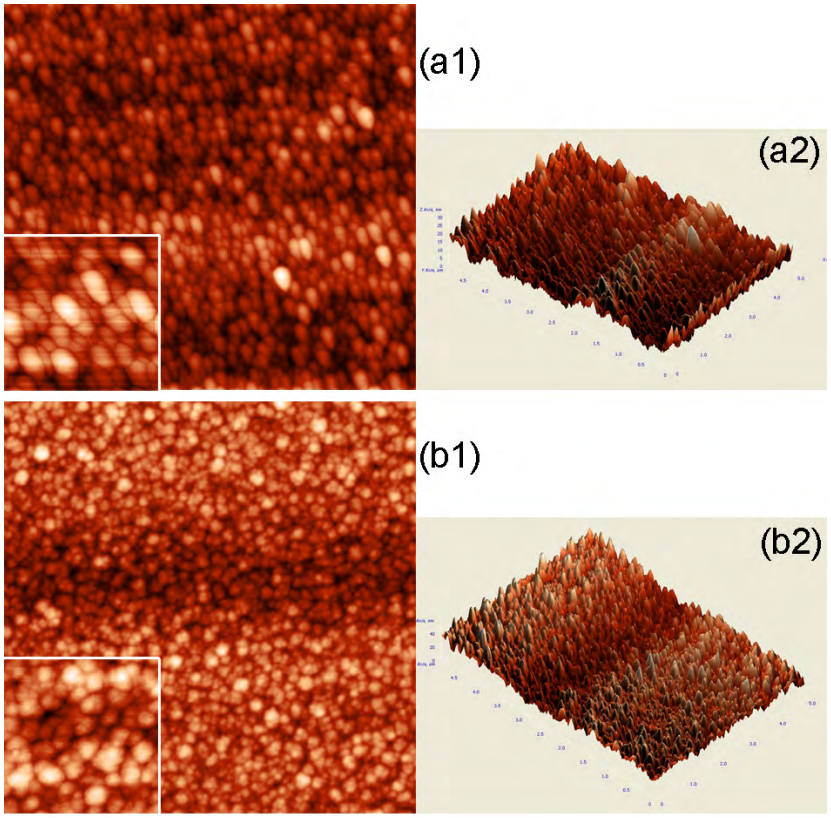

Figure 7.10: 2D (1) and 3D (2) micrographs for two DLC coatings at 5×5 μm^2 scan scales : (a) DLC10 and (b) DLC30. Insets: 2D micrographs at 1×1 μm^2 scan scales.

Table 7.5: Surface roughness analysis of DLC-F5-25 coatings.

Sample	50×50 μm^2		20×20 μm^2		5×5 μm^2	
	RMS (nm)	Roughness average (nm)	RMS (nm)	Roughness average (nm)	RMS (nm)	Roughness average (nm)
DLC-F5	11.1	9.0	5.8	4.7	5.5	4.5
DLC-F10	11.0	9.3	6.0	4.2	5.8	4.4
DLC-F15	11.2	8.9	5.2	4.3	4.3	3.4
DLC-F20	8.1	6.2	5.2	4.5	3.9	3.3
DLC-F25	11.3	9.3	7.6	5.4	4.4	3.5

10 C_2H_2 flow rate during surface fabrication, the CF_4 flow rate change from 5 to 25 sccm has slight influence on the coating roughness. Compared to DLC samples, apparently higher RMS and roughness average values were observed on corresponding DLC-F samples. The incorporation of fluorine into DLC samples contributes to higher roughness of the coating surface.

The AFM micrographs of three DLC-F coatings are shown in Fig. 7.11. Similar to DLC coatings, both the pebble-like and the granule-like morphologies were presented on this series of DLC-F coatings. The pebble-like was only observed on DLC-F20 and the granule-like was found on other four DLC-F samples.

7.3.4 Nanoindentation studies

Both the Young's modulus (E) and hardness (H) of the DLC samples decline steadly with the increasing C_2H_2 flow rate (Fig. 7.12). The narrow range of hardness for DLC samples, 16.8–26 GPa, is close to 10–20 GPa for amorphous carbon (a-C) and hydrogenated alloys (a-C:H) and much lower than 80 GPa for tetrahedral amorphous carbon (ta-C). Combined with the C=C sp2 and C-C sp3 percentages presented in Fig. 7.3, the decrease in hardness can be explained by the increasing C=C sp2 percentage and decreasing C-C sp3 percentage in the DLC series except for DLC30, in which the tendency of both percentages reverse. The substantial percentage of C-O bond in DLC30 (Table 7.1) is probably attributed to the continuing decrease of hardness.

The H/E value of DLC samples increases steadily with the C_2H_2 flow rate (Fig. 7.13). The H^3/E^2 value first drops slightly at DLC10, then increases slowly to the peak at 0.3495, and continuously drops to the valley at 0.3009 for

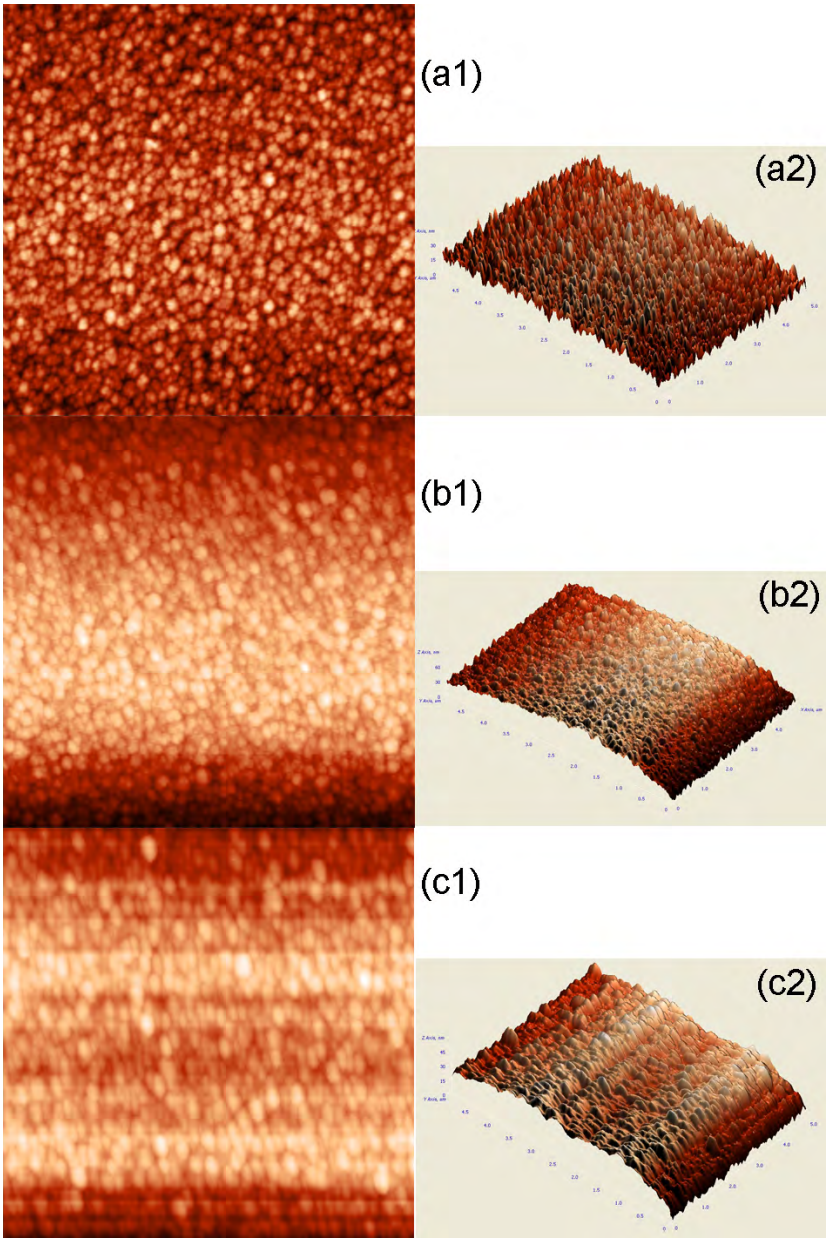

Figure 7.11: 2D (1) and 3D (2) micrographs for three DLC-F coatings at 5×5 μm^2 scan scales: (a) DLC-F5, (b) DLC-F10 and (b) DLC-F20.

the sample DLC30.

Both the Young's modulus and hardness values measured on DLC-F coatings

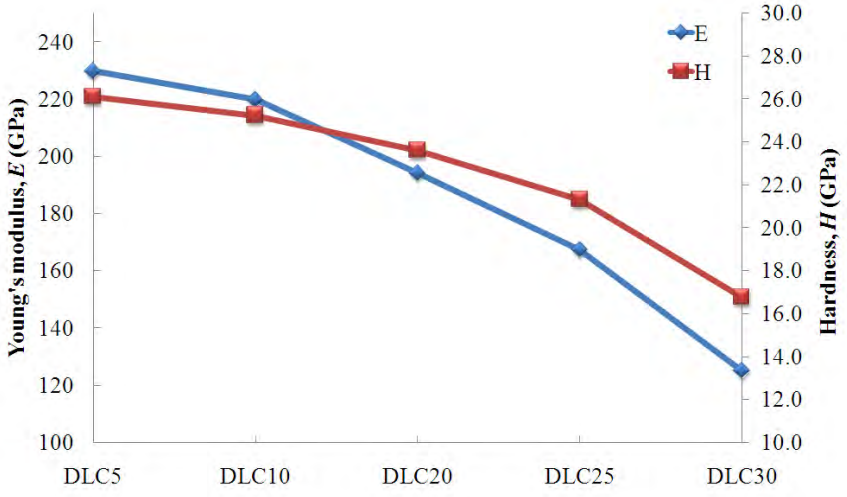

Figure 7.12: Young's modulus and hardness of DLC coatings.

Table 7.6: Mechanical properties of DLC coatings (obtained from nanoindentation experiments), and steel.

Sample	C_2H_2 (sccm)	Youngs modulus (GPa)	Hardness (GPa)	H/E (GPa)	H^3/E^2
DLC5	5	230	26.1	0.1137	0.3372
DLC10	10	220	25.2	0.1148	0.3325
DLC20	20	194	23.6	0.1217	0.3495
DLC25	25	167	21.3	0.1273	0.3454
DLC30	30	125	16.8	0.1340	0.3009

show a similar trend versus the CF_4 flow rate in Fig. 7.14: both values decrease from DLC-F5 to the valley on DLC-F10, then increase to the peak on DLC-F20, and finally decrease again on DLC-F25. The valley and peak values for Young's modulus are 126 and 166 GPa, and for hardness are 15.5 and 19.1 GPa, respectively. Therefore, in this F-DLC series, DLC-F10 is the softest and most pliable, while DLC-F20 is the hardest and stiffest.

The trend of hardness can be postulated to be affected by C=C sp2 and C-C

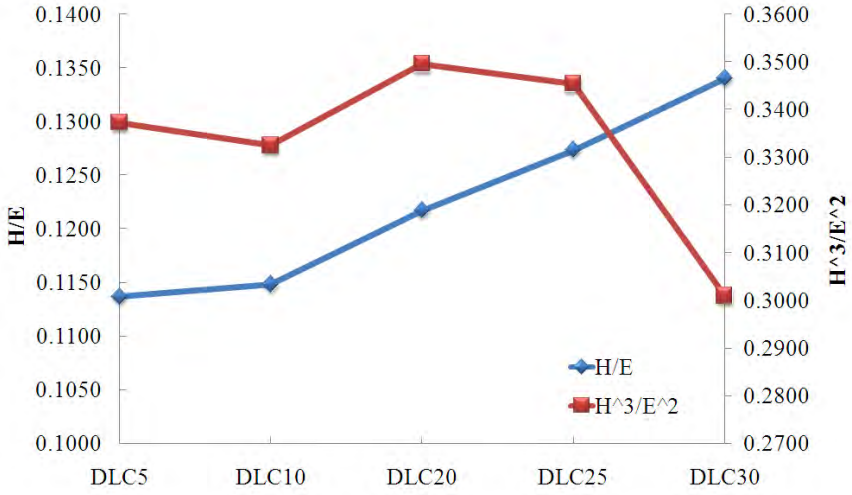

Figure 7.13: H/E and H^3/E^2 values for DLC coatings.

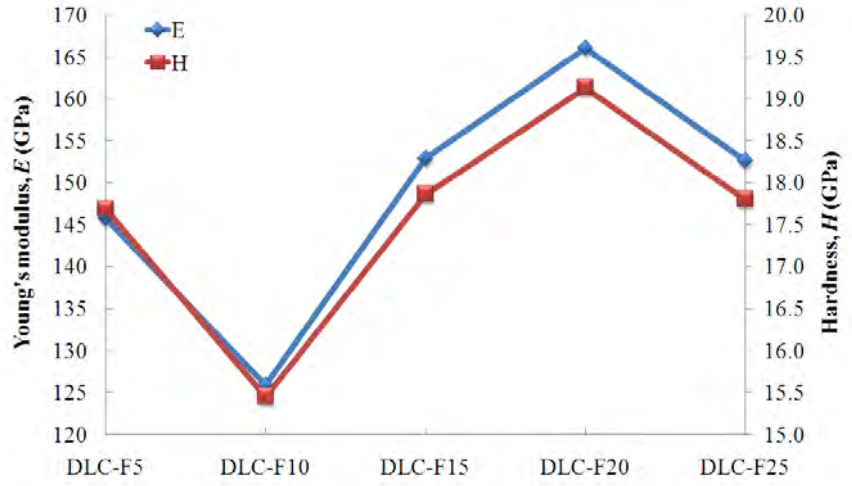

Figure 7.14: Young's modulus and hardness values of DLC-F coatings.

sp3 bond percentages indicated in Fig. 7.7. On sample DLC-F10, the highest C=C sp2 bond percentage and the second lowest C-C sp3 bond percentage were obtained. On sample DLC-F20, the second lowest C=C sp2 bond percentage and the third highest C-C sp3 bond percentage were observed. However, the hardness

trend is not strictly in accordance with the ratio of C-C sp3 to C=C sp2 bond percentages.

Table 7.7: Mechanical properties of F-DLC coatings (obtained from nanoindentation experiments), and steel.

Sample	CF_4 (sccm)	Youngs modulus (GPa)	Hardness (GPa)	H/E (GPa)	H^3/E^2
DLC-F5	5	146	17.7	0.1214	0.2605
DLC-F10	10	126	15.5	0.1228	0.2330
DLC-F15	15	153	17.9	0.1168	0.2438
DLC-F20	20	166	19.1	0.1152	0.2541
DLC-F25	25	153	17.8	0.1166	0.2422

The H^3/E^2 value has a trend similar to that of the Young's modulus and hardness trends (first decrease, then increase and decrease again, in Fig. 7.15). The H/E value has a reverse trend.

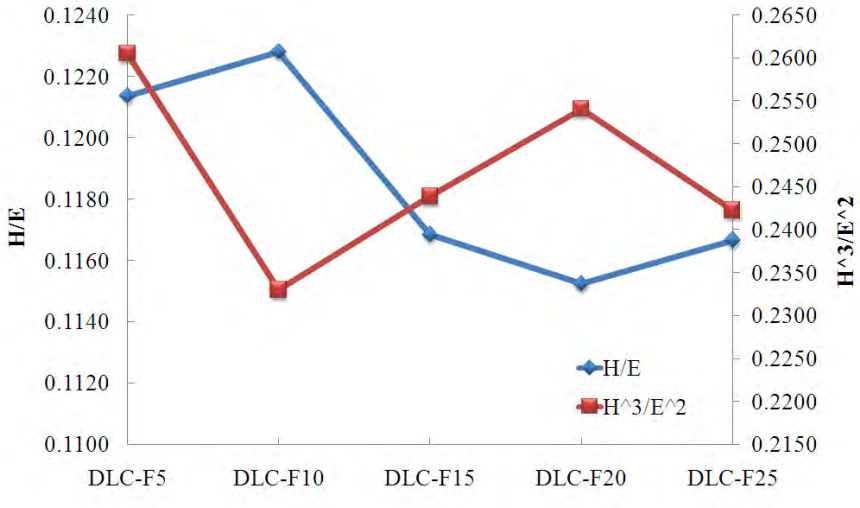

Figure 7.15: H/E and H^3/E^2 values for DLC-F coatings.

7.4 Conclusions

DLC and F-DLC coatings with different fluorine contents were successfully fabricated by adjusting the CF_4 flow rate during the CFUBMS deposition procedure. The fluorine content and C-F bond percentages on the coating surface were increased with escalating CF_4 flow rate. Smoother surfaces, revealed by smaller RMS and roughness average values, were obtained on F-DLC coatings than on the DLC sample. Incremental incorporation of fluorine into DLC samples also led to a noticeable increase in water contact angle and a substantial decrease in both Youngs modulus and hardness.

References

[1] B D Beake, V M Vishnyakov, and J S Colligon. Nano-impact testing of TiFeN and TiFeMoN films for dynamic toughness evaluation. *Journal of Physics D: Applied Physics*, 44(8):085301, 2011. 168

[2] A Leyland and A Matthews. On the significance of the H/E ratio in wear control: a nanocomposite coating approach to optimised tribological behaviour. *Wear*, 246(1–2):1–11, 2000. 168

[3] B.D. Beake, G.S. Fox-Rabinovich, S.C. Veldhuis, and S.R. Goodes. Coating optimisation for high speed machining with advanced nanomechanical test methods. *Surface and Coatings Technology*, 203(13):1919–1925, 2009. 168

[4] T. Y. Tsui, G. M. Pharr, W. C. Oliver, C. S. Bhatia, R. L. White, S. Anders,

REFERENCES

A. Anders, and I. G. Brown. Nanoindentation and nanoscratching of hard carbon coatings for magnetic disks. *MRS Proceedings*, 383, 1995. 168

[5] K. L. Johnson. *Contact Mechanics*. Cambridge University Press, Cambridge, UK, 1985. 168

Chapter 8

Conclusions and future work

This study aimed to learn from nature and to engage relevant knowledge in engineering designs. Since what is bio-inspired and designed will be applied back in a resembling environment, this methodology brings in natural considerations of many practical factors. Subsequently, various methods were adopted in the research to fabricate rough surfaces that mimicked certain plant leaves, followed by an investigation of their surface characteristics and wettability.

Native Australian leaves were firstly selected based on their hydrophobicity. Four categories, namely hairy, palm-tree-like, micro-ridge and micro-bump, were summarized based on their distinct surface morphologies. Different water-repelling mechanisms leaves were postulated for these categories. For *Eucalyptus* particularity, physical models were constructed and surface energy analysis was carried out on the models. In contrast with *Eucalyptus*, greater cylindrical length below the microscopic hemisphere in the lotus model increased the energy barrier for the wetting transition, which is beneficial for hydrophobic stability. The strong water adhesion on *Eucalyptus* leaves was also explained by a relatively

larger liquid-solid contact area than for lotus.

Two common methods, self-assembly and photo-lithography, were examined for fabricating hydrophobic surfaces. Brief immersion of glass slides in an ethanol solution of hydrolysed oxysilane lead to a hydrophobic surface with micrometer roughness. The self-assembly mechanism was explained using chemical reactions and molecular interactions. Surfaces with periodic micro-posts were fabricated by photo-lithography. Anisotropic wetting characterized with distinct contact angles obtained on different directions, was observed on these surfaces. The contact angle values were mathematically explained by roughness "on the line" and the Cassie equation. Squircle-shaped contact footprints were observed on droplets resting on these surfaces. A nearly constant difference was revealed between the base lengths measured on the lattice and the diagonal directions. Adhesion between the droplet and the surface could be approximated to change linearly with the surface tilt angle.

DLC and F-DLC coatings with different fluorine contents were fabricated by adjusting the CF_4 flow rate during the CFUBMS deposition procedure. The fluorine content and C-F bond percentages on the coating surface increased with escalating CF_4 flow rate. Smoother surfaces, revealed by smaller RMS and roughness average values, were obtained on F-DLC coatings than on the DLC sample. Incremental incorporation of fluorine into DLC samples also led to a noticeable increase in water contact angle and a substantial decrease in both Youngs modulus and hardness. The mechanical properties of F-DLC10 sample were studied by nanoindentation and FEM. While there is a slight decrease in the Youngs modulus and hardness compared to the DLC sample, its H/E value, and hence the wear resistance, is the best amongst all samples studied.

Further work following this research may greatly enhance the applicability and scope of the approaches and methods discussed here. Specific geometries observed on Australian native leaves, for example, palm-tree-like and micro-ridge, can be explored more about mechanical and directional wetting properties, as well as other functions. Materials that self-polymerize at ambient conditions, such as dopamine, can be incorporated into oxysilane solution to make controllable and durable hydrophobic coatings. Finally, deposition of thin F-DLC films on micro-structures can make chemically inert and mechanically tough hydrophobic surfaces.

Appendix A

Operation of Atomic Force Microscopy (AFM)

AFM (Ntegra Prima, NT-MDT Co., Moscow, Russia) was used in a semi-contact mode to obtain roughness parameters and 3D surface profiles in this study. The whole system is composed of a scanning unit, a controller and a data acquisition system (Fig. A.1). Controllers are usually chosen and integrated into the system based on different modes and purposes, such as Atomic Force Acoustic Microscopy, Electrochemical Measurements, Liquid Measurements, Magnetic Field Measurements, and NanoIndentation and sclerometry.

Other supplementary apparatuses are also included to assure convenient and precise measurement. The optical microscope assists viewing the sample surface and the probe, from which a relatively smooth area is chosen for scanning. The anti-vibration lab table, on which the scanning unit sits, reduces the effects that mechanical vibration causes during scanning. Below is a general description of AFM scanning procedure.

A. OPERATION OF ATOMIC FORCE MICROSCOPY (AFM)

Before AFM scanning, samples are fixed on a plastic sample holder using adhesive tape and mounted on the stage thereafter. The probe (type NSG10) used here contains a tetrahedral tip with a height of 14–16 μm and a typical curvature radius of 6 nm. The tip is mounted on a rectangular single crystal silicon (N-type, antimony doped) cantilever with a thickness of 2 μm, a resonant frequency of 140–390 kHz and a force constant of 3.1–37.6 N/m. Other properties of the probe include: chip size: 3.4×1.6×0.3 mm, relfective side: Au, tip curvature radius: 10 nm, aspect ratio: 3:1–5:1, cantilever length: 95±5 μm, cantilever width: 30±5 μm, cantilever thickness: 1.5–2.5 μm.

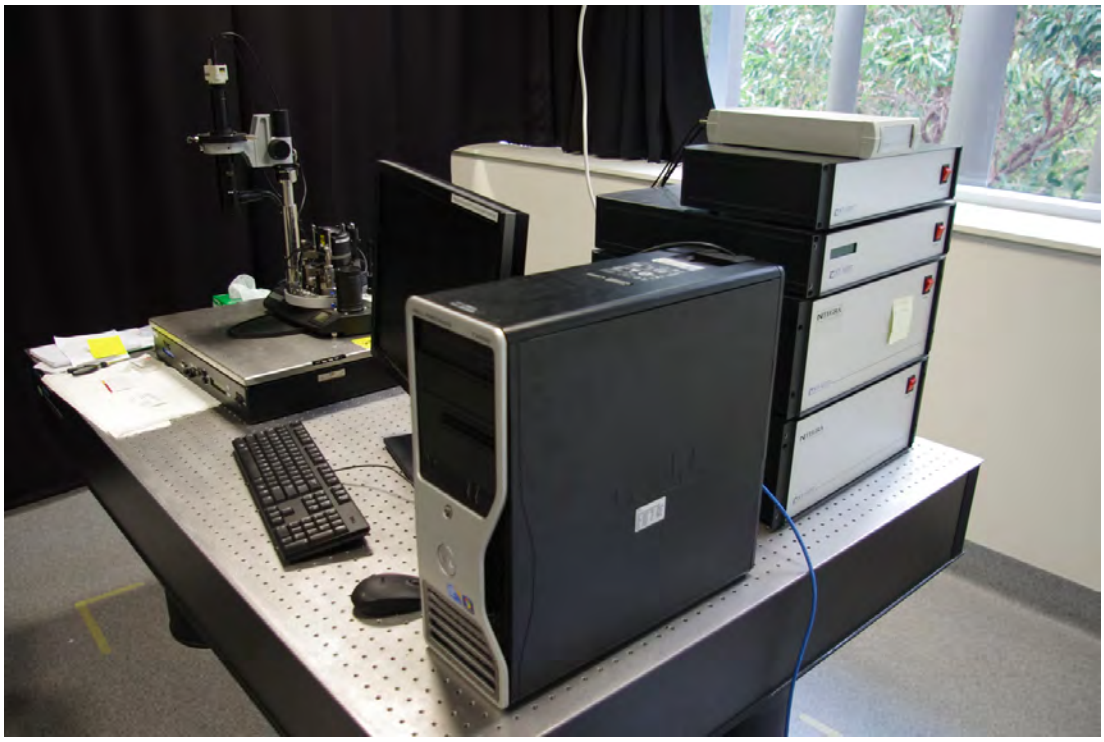

Figure A.1: Configuration of a complete AFM system.

A.1 Aiming of laser beam

After the sample and probe are mounted, the laser beam is aligned on the cantilever of the probe by adjusting the two screws on the scanning head (Fig. A.2).

The Aiming tab is opened when clicking the corresponding button on the Main Operations Panel (Fig. A.3). The DFL value, the difference signal between top and bottom halves of the photodiode, and the LF value, the difference signal between left and right halves of the photodiode, are adjusted to zero by rotating other two screws on the scanning head. The laser beam thus hits the photodiode center and illuminates equally the four sectors.

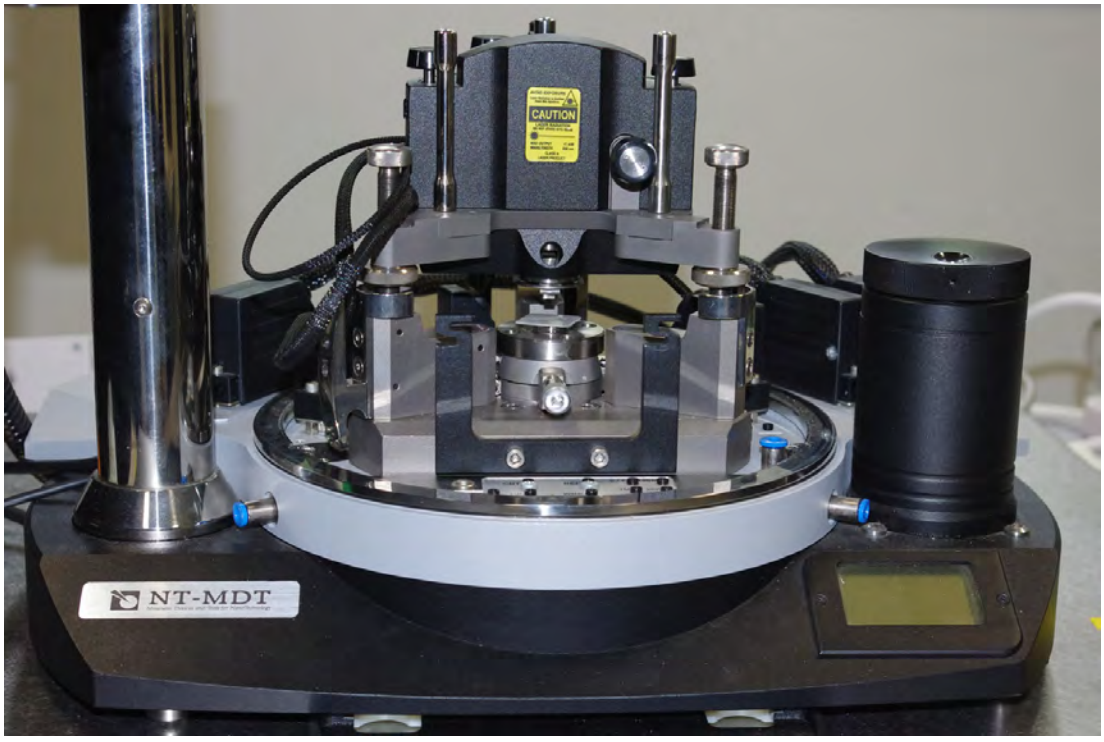

Figure A.2: AFM scanning unit.

The Laser value on the Aiming tab indicates the sum of signal coming from

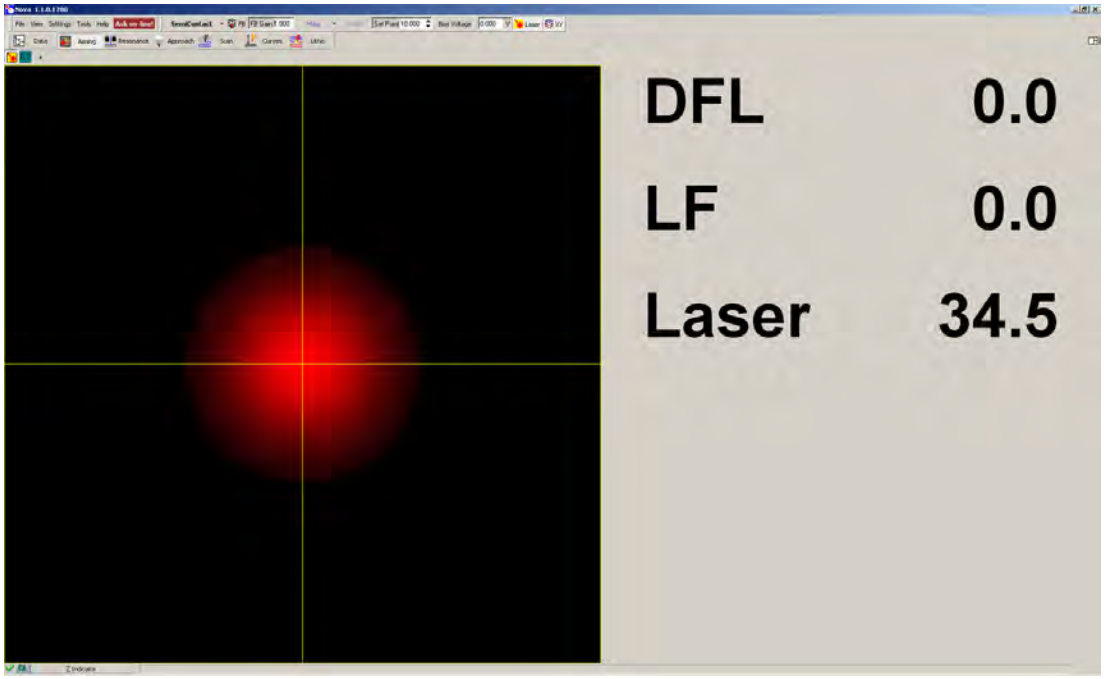

Figure A.3: AFM aiming.

all four segments of the photodiode and is proportional to the intensity of the laser radiation reflected from the cantilever. In Fig. A.3, the Laser value is 34.5.

A.2 Setting resonance frequency

In the Resonance tab, click the Run button to detect the resonance frequency of the cantilever and to preset it in the program. The biggest symmetrical peak is auto-picked by the detecting system. The Mag signal is usually set up to the range of 10-35 nA by adjusting Amplitude (generator output) or Gain (gain of the lock-in detector). In Fig. A.4, the Laser value is approximately 25. The Generator Amplitude and Lock-In Gain have to be changed as necessary when a distinct frequency cannot be found.

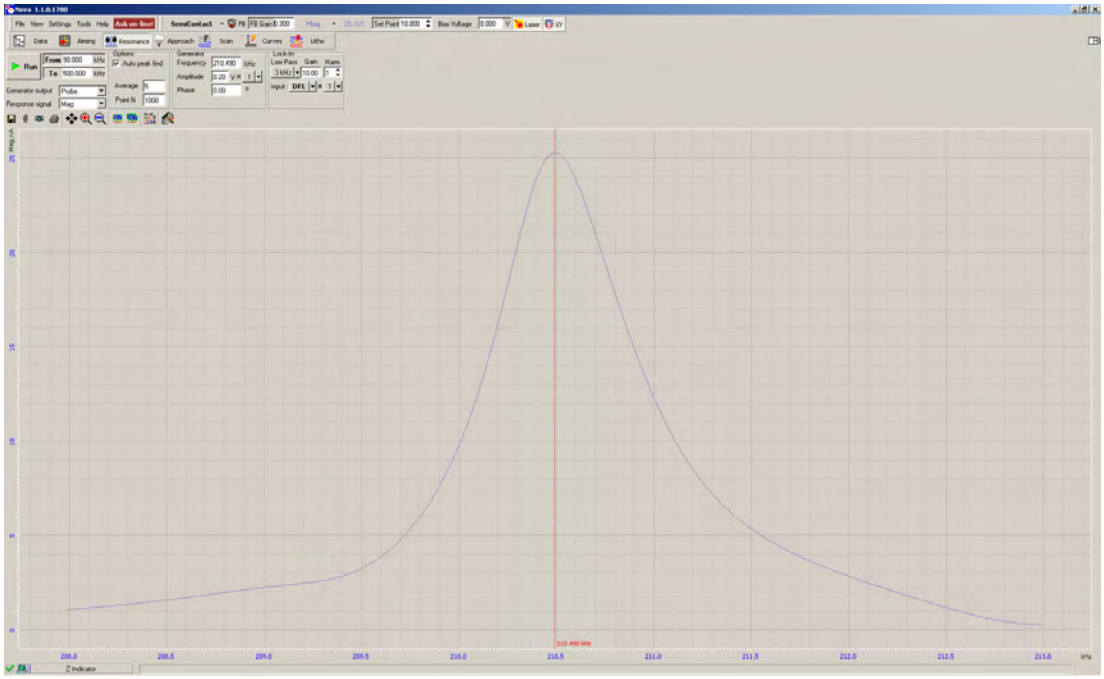

Figure A.4: AFM resonance frequency detected by the system.

A.3 Approaching the surface

The sample is first manually brought close to the probe at a distance of 0.5-1 mm by rotating the approach knob counterclockwise. With the "Auto Setpoint"button pushed down, an automatic approaching procedure begins after the "Landing"button on the "Approach"tab is pushed. A message appears in the information box on upper-left corner of the window when the procedure is finished. Under this "Auto Setpoint"setting, the "Set Point"value is automatically set equal to half of the current Mag signal. Manual setting of the parameter "Set Point"is available by typing a designated value into the text box behind the label.

Fig. A.5 shows the Mag signal after approach is completed. Nearly no noise or oscillation on the Mag signal is observed in this case. Nevertheless, the pa-

rameter "FB Gain" usually needs to be adjusted to reduce the noise generated in the feedback loop. The magnitude of the scanner extension is characterized by the length of the colored bar in the lower-left corner of the window. After approaching, the Z-scanner stays at a position approximately half of the scanner extension range. Subsequently, the system is ready for scanning.

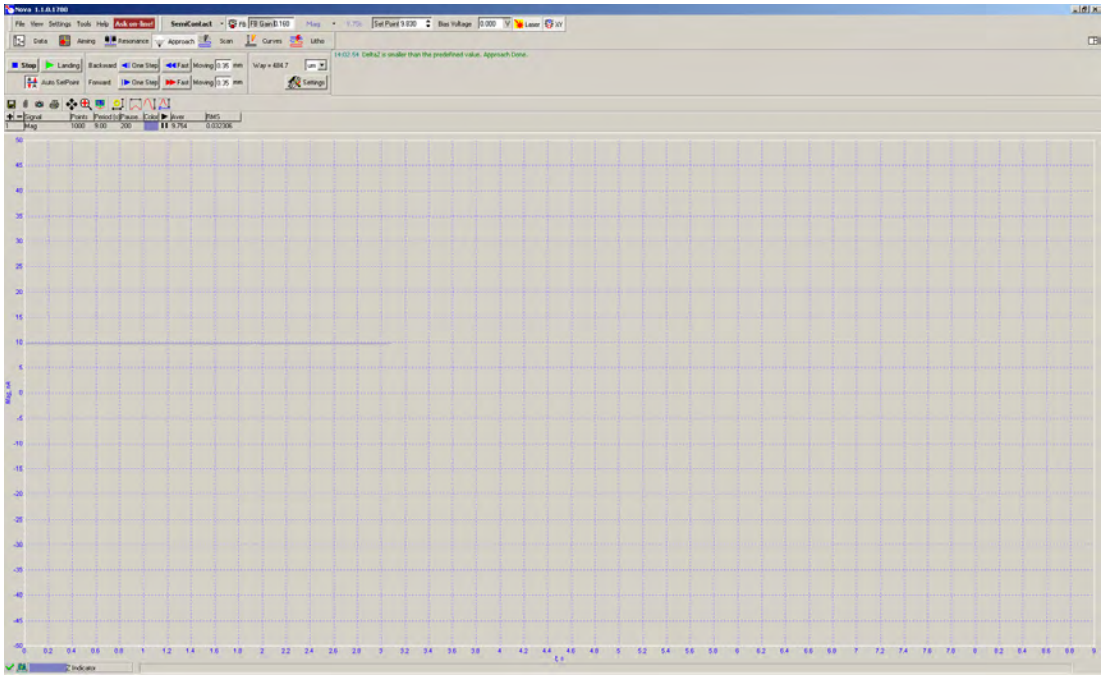

Figure A.5: AFM approach.

A.4 Scanning the surface

A scan can started by pushing the "Run" button, after setting up mode, scanning frequency and direction. The two-dimensional line profiles are collected line by line from the bottom to the top (Fig. A.6). A three-dimensional topography is thus acquired by combing the line profiles.

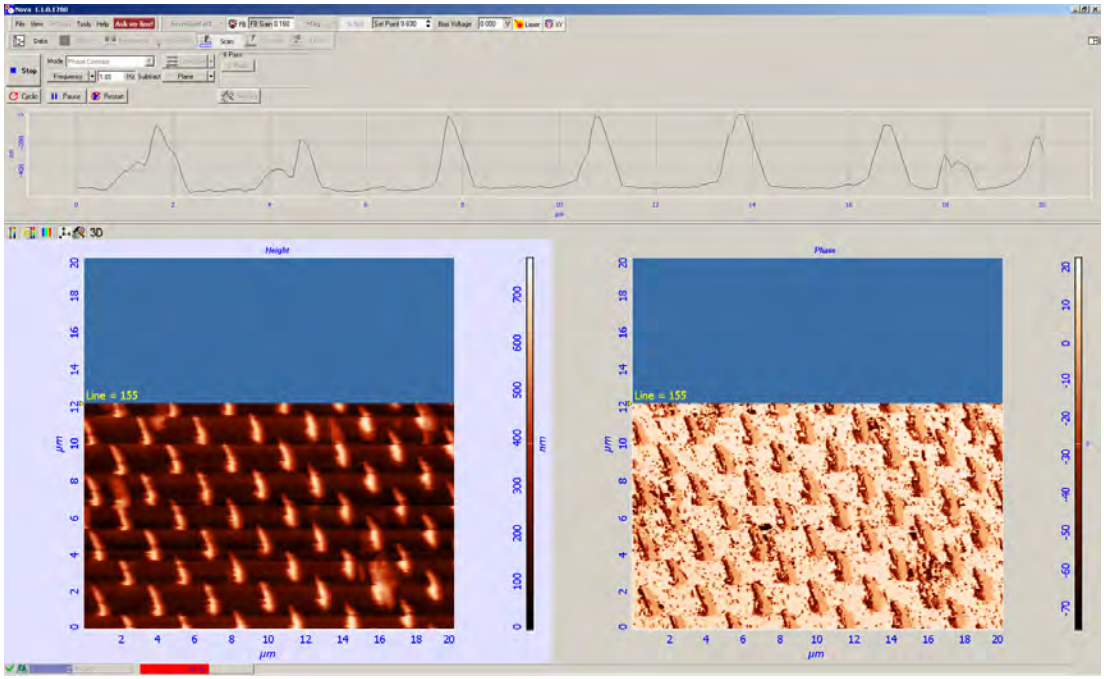

Figure A.6: AFM scanning in process.

A.5 Image analysis and data processing

Raw AFM data can be processed with the Image Analysis P9 program (Build 3.5.0.2072) for surface images and topography profiles. After tilt surface subtraction, 2D and 3D surface images are obtained in the display window (Fig. A.7). Statistic parameters, such as root mean square (RMS) and roughness average, are retrieved by clicking the corresponding menu on the right side of the window (Fig. A.8).

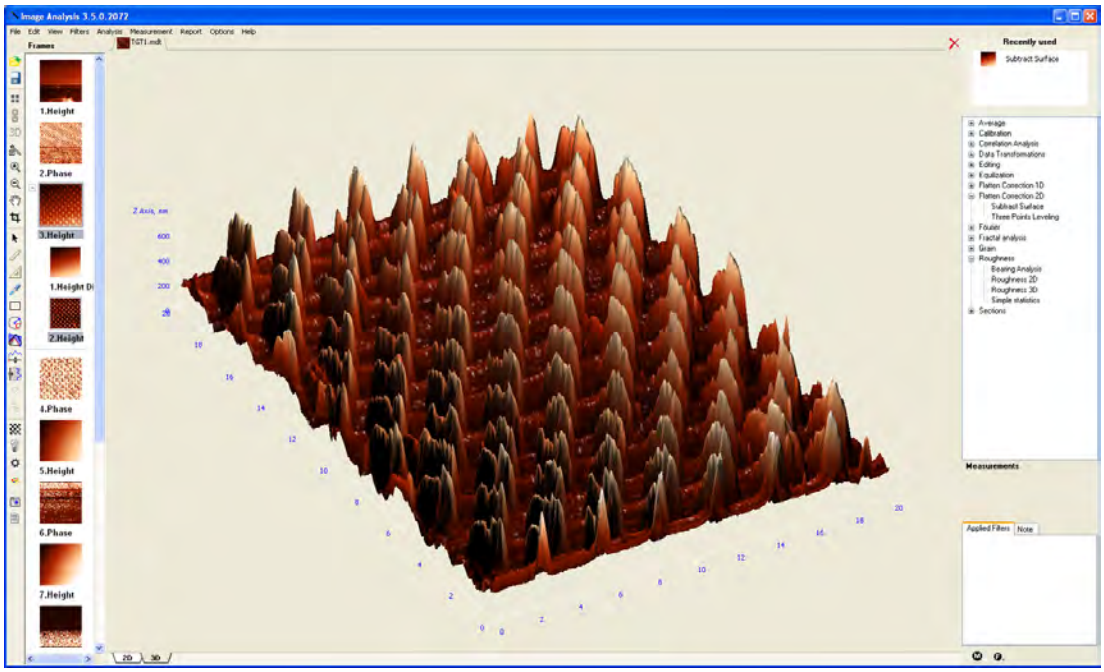

Figure A.7: Date and image processing: 2D and 3D images.

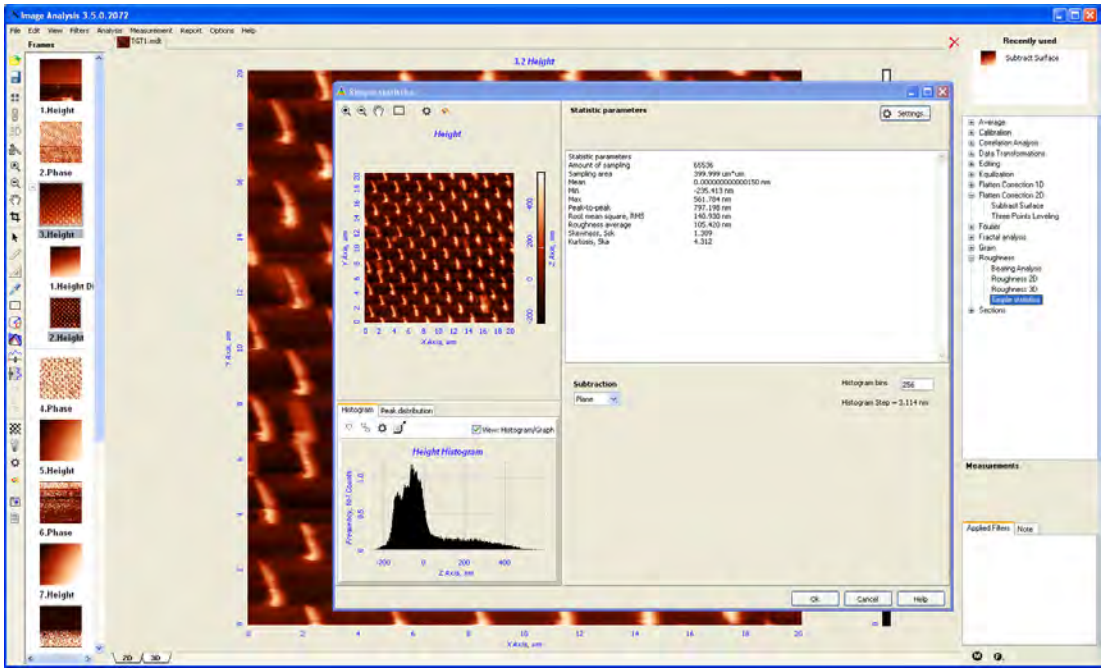

Figure A.8: Date and image processing: statistic parameters.